Design Studies for a Tracking Upgrade of the Crystal Barrel Experiment at ELSA

and

Installation of a Tracking Test Bench

Dissertation
zur
Erlangung des Doktorgrades (Dr. rer. nat)
der
Mathematisch-Naturwissenschaftlichen Fakultät
der
Rheinischen Friedrich-Wilhelms-Universität Bonn

vorgelegt von

Dipl. Phys. Alexander Winnebeck
aus Bonn

Bonn, im Oktober 2009

Angefertigt mit Genehmigung
der
Mathematisch-Naturwissenschaftlichen Fakultät
der
Rheinischen Friedrich-Wilhelms-Universität Bonn

Erscheinungsjahr: 2010

Diese Dissertation ist auf dem Hochschulschriftenserver der ULB Bonn unter
http://hss.ulb.uni-bonn.de/diss_online
elektronisch publiziert.

1. Gutachter: Prof. Dr. R. Beck
2. Gutachter: Prof. Dr. H. Ströher

Tag der Promotion: 17.12.2009

Abstract

Ever since mankind was interested in the understanding of the universe and especially the matter in it. The fundamental building blocks of matter seem to be quarks and gluons, whose interactions are investigated in hadron physics. To study this strong interaction different experimental approaches can be used. One way is to do spectroscopy similar to atomic physics.
The Crystal Barrel experiment at ELSA performs spectroscopy of nucleons to learn more about the strong interaction. A major improvement of this experimental setup will be the introducing of charged particle tracking as it will be shown in this thesis.
Different detector concepts will be discussed concerning feasibility, material budget and especially momentum resolution. It will turn out that a Time Projection Chamber (TPC) is the optimal solution.
Then it will be shown how a prototype TPC is tested using a newly installed tracking test bench with an electron beam and obtained results will be presented.
The design of the final TPC and its integration into the Crystal Barrel experiment will be discussed as well as methods to calibrate the detector.

Contents

Nemo nascitur sapiens, sed [fortasse] fit.
Seneca

1 Introduction

The principle of all physical investigations is to understand the behavior of nature by finding the basic symmetries and regularities.
All the matter surrounding us, consists of atoms[1], and since E. Rutherford's scattering experiments of α particles on a gold foil[2], one knows that atoms are not solid, but themselves consist of a nucleus encircled by electrons.
After the discovery of the neutron by J. Chadwick in 1932, nuclei could be constructed out of protons and neutrons - the nucleons. However, the mass difference between nuclei and the sum of their constituents was an impressive proof of A. Einstein's energy mass relation[3].
In 1930 the neutrino was postulated by W. Pauli to fullfill the conservation laws in the β decay and in 1956 it was experimentally discovered [3].
The stability of nuclei can not be explained with the electromagnetic force, as same charges repulse each other. Therefore H. Yukawa postulated in 1935 that the nucleons are bound together through particle (pion) exchange. This strong force is much stronger than the electromagnetic one, but with a much shorter range due to its massive exchange bosons.
In the late 1960s deep inelastic electron proton scattering revealed, that protons are no fundamental particles, but are composed of pointlike sub particles called quarks [4].
Today there is no evidence for a substructure of quarks. Therefore leptons[4], quarks, and the gauge bosons as mediators of the forces are assumed to be fundamental particles.

1.1 Hadron Physics

Particles which are composed out of quarks are called hadrons. Quarks do have an additional quantum number labeled color charge with values red, anti-red, green, anti-green, blue, and anti-blue which becomes necessary to construct totally antisymmetric wave functions for quark systems, since quarks are fermions. The interaction between quarks is based on this color charge, where gluons are the exchange gauge bosons. In contrast to photons, the gauge boson of the electromagnetic interaction, gluons carry a color and an anti-color, thus interactions between gluons occur, which is not the case for photons.
Only colorless hadrons were observed in nature, and the simplest ways to ob-

[1] atomos *classical greek*: indivisible. Democritus (460 - 371 B. C.) conjectured that atoms are the smallest fraction of material, which still have the same behavior than the whole, and can not be divided anymore.

[2] Actually Geiger-Marsden experiment (1909) [1], but the interpretation was done by Rutherford (1911) [2].1

[3] $E = mc^2$. The binding energy, which corresponds to the mass difference, was measured in nuclei decays.

[4] $e^{\pm}$, $\mu^{\pm}$, $\tau^{\pm}$, ν.

tain this are either quark-antiquark pairs $(q\bar{q})$[5], called mesons, or a triple of quarks (qqq) with colors r+g+b = colorless, labeled baryons. Proton and neutron are the most prominent baryons.
There are 6 flavors of quarks (up, down, charm, strange, top, bottom) organized in three families[6]

$$\begin{pmatrix} u \\ d \end{pmatrix}, \begin{pmatrix} c \\ s \end{pmatrix}, \begin{pmatrix} t \\ b \end{pmatrix},$$

where the upper quarks have a charge of $+2/3\,\mathrm{e}$ and the lower $-1/3\,\mathrm{e}$.
The proton for instance is build out of 2 up quarks and one down quark (uud), though the mass of the proton ($938.3\,\mathrm{MeV/c^2}$) is much greater that the sum of the quark masses ($\approx 10\,\mathrm{MeV/c^2}$). So approximately 99% of the hadrons' masses is coming from their binding energies. This is just the other way around as for nuclei where the binding energy is on the sub percent level of the mass. The strength of the strong interaction expressed in terms of the coupling

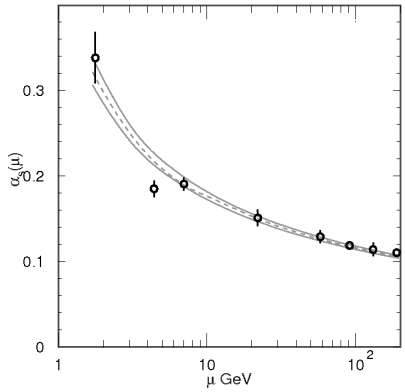

Figure 1: Strong "running" coupling constant α_s plotted versus the energy scale μ.[5]

constant α_s is plotted in figure 1. It's not really a constant since it depends on the energy scale μ. For high energies ($\mu \gtrsim 10\,\mathrm{GeV}$) α_s is getting small, the quarks are less coupled so that perturbation theory[7] can be applied. For infinite μ the coupling strength vanishes, which is called asymptotic freedom[8]. At lower energy scales, i. e. larger distances, the strength of the coupling increases. The quarks are *confined* inside the hadron. Whenever one tries to separate a quark, the potential energy increases until it is large enough to produce another quark-antiquark pair, which splits into a hadron and a new meson. For this reason no free quarks can be observed.
The corresponding theory for this strong interaction based on the color charge is the Quantum Chromo Dynamics (QCD). Since α_s is in the order of 1 at low energies[9], where the nature happens, the methods of perturbation theory can

[5] Color + anti-color = colorless.
[6] Similar to leptons $\binom{e}{\nu_e}, \binom{\mu}{\nu_\mu}, \binom{\tau}{\nu_\tau}$.
[7] Expansion of wave function in powers of the coupling constant α. Higher orders can be neglected if $\alpha \ll 1$.
[8] Nobel prize in physics 2004
[9] Energies in the range of 1 GeV.

not be applied, because the series in the coupling constant does not converge. Therefore other approaches are necessary to solve QCD in this energy regime:

- Lattice QCD uses enormous computing power to determine the behavior of a strong interacting system of quarks and gluons discretized in space and time with a typical scale a. The gimmick is now to calculated the observables for different a and then perform an extrapolation for $a \to 0$ to extract physical values for observables.
- A second approach is the chiral perturbation theory (χPT), an effective field theory, which does not use quarks and gluons, but light mesons (π, η, K) as degrees of freedom. Therefore methods of perturbation theory can be applied to calculate observables with the costs of some low energy constants, which need to be extracted from experiments or Lattice QCD simulations.

At some points models can be consulted to get predictions for observables like masses of states. One class of models are the constituent quark models, which the Bonn model[6] is one example of.

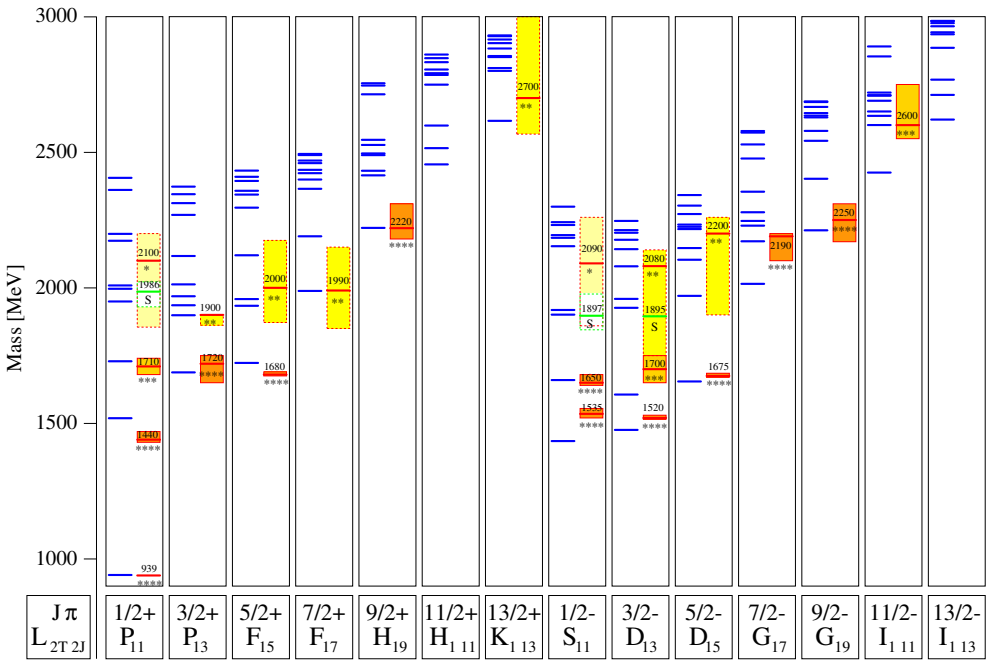

Figure 2: Predicted masses of nucleon resonances of the Bonn Model [6] separated for spin and parity (blue lines) compared to measurements (red lines).

The Bonn model predicts the masses of resonances e. g. of nucleons, as plotted in figure 2. The blue lines correspond to predicted resonances and in red real measurements with uncertainties and widths are shown. The model is fixed at the proton mass and most of the experimentally observed resonances fit to the prediction, but some (e. g. $S_{11}(1535)$, $P_{11}(1440)$) are quite off. In addition, the model delivers many resonances with masses $\gtrsim 2\,\mathrm{GeV/c^2}$ without any experimentally evidences. These *missing resonances* are not special to the Bonn model, but show up in other models as well. There are many conjectures about

these missing resonances. One explanation could be that the quarks inside a nucleon are not free, but obey a substructure e. g. a quark-diquark structure, which reduces the degrees of freedom and in parallel the number of excited states[10]. Another explanation could be that the missing resonances are not (or only very rarely) produced in pion scattering experiments, where most of the data in figure 2 is coming from.
For that reason photoproduction experiments (γ N $\rightarrow$ N* + X) are performed. One approach to understand more of the interaction between quarks is identical to the one in atomic physics, namely performing spectroscopy. But unfortunately the job is much more complex, since the resonances are not narrow lines, but broad and overlapping due to the much shorter life time[11].
To learn more about the strong interaction it is very important to extract all contributing resonances and not only the superposition of many, thus methods for separation are needed. By preparation of the initial and/or final state, contributing resonances can be suppressed and smaller amplitudes can be revealed. The preparation is performed by polarizing the initial particles and/or measuring the polarization of final state particles.
In this context the concept of *polarization observables* (POs) was introduced, which in principal parameterizes the cross section in terms of target, beam, and recoil polarization. In case of the Crystal Barrel experiment, where a longitudinal polarized target and linearly or circularly polarized beam is available, the cross section can be expressed similar to [11] by

$$\frac{d\sigma}{d\Omega}(\theta,\phi) = \frac{d\sigma_0}{d\Omega}(\theta)\left(1 - p_\gamma^{lin}\Sigma\cos(2\phi) - p_\gamma^{lin}p_z G\sin(2\phi) + p_\gamma^{circ}p_z E\right).$$

Beside the unpolarized differential cross section $\frac{d\sigma_0}{d\Omega}(\theta)$ there are three more observables - Σ, G, and E - contained in the parameterization of the cross section shown above. In total there are 16 observables for single pseudoscaler meson photoproduction, but only a subset of 8 well chosen[12] is needed to have a *complete experiment*[13], meaning the decomposition of the cross section into the partial waves is uniquely.
The extraction of the polarization observables of the cross section is done by preparing the initial polarization (target and beam) and by fitting the strength of the measured ϕ modulation except for a phase.

1.2 Crystal Barrel experiment

The Crystal Barrel experiment at ELSA is a fixed target photoproduction experiment to perform baryon spectroscopy. The name is given by the central calorimeter, which was already used at LEAR[13] to investigate $p\bar{p}$ annihilations[14].
In the following subsections the aim of the experiment, the experimental setup, and planned upgrades are discussed.

[10] For details see [7], [8], [9], [10].
[11] $\Gamma\tau \geq \hbar/2$, i. e. short lifetime $\rightarrow$ great widths.
[12] E. g. σ_0, Σ, T, P, E, G, O_x, C_x.
[13] **L**ow **E**nergy **A**ntiproton **R**ing at CERN

1.2.1 Aim of the experiment

The goal of the Crystal Barrel experiment is to measure the excitation spectrum of baryons and the properties of these excited states. These informations will lead to a deeper understanding of QCD at low energies and can be used to test model predictions and to improve them.
As explained above a preparation of the initial state spins is used to obtain polarization observables, which are instrumented by the partial wave analysis to resolve ambiguities and extract the properties of excited states. Therefore the target and the photon beam are polarized in the experiment.

1.2.2 Experimental setup

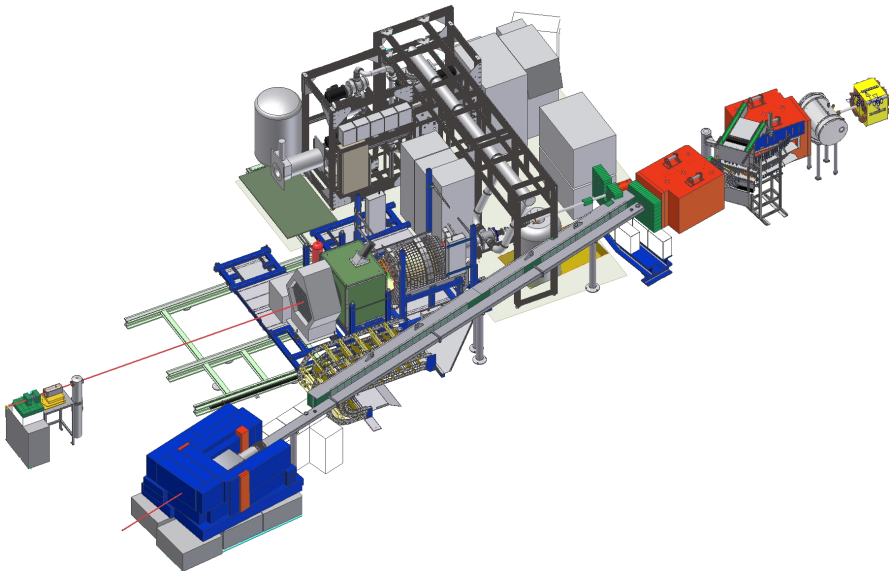

Figure 3: Artificial overview drawing of the Crystal Barrel experimental setup. The electrons from ELSA entering from the right hand side (last quadrupole in yellow), hit the radiator target (grey cylinder), are deflected by two dipole magnets (red blocks), and finally stopped in the beam dump (blue boxes on the bottom left hand side). The generated photon beam goes straight through the deflecting units, through the target, which is surrounded by the detector system. At the end of the line the photons are absorbed in the Gamma Intensity Monitor.

Production of high energy photon beams

A high energy photon beam is needed, and since photons with energies up to some GeV can not be generated directly, an electron beam is used to produce these.
The **El**ectron **S**trecher **A**ccelerator ELSA [15], located in the basement of the Physikalisches Institut in Bonn, delivers a quasi continuously extracted electron beam of longitudinally polarized or unpolarized electrons with energies up to 3.5 GeV at a current of $\lesssim 1$ nA.

With it three types of photon beams become available:

- An **unpolarized** photon beam is created when unpolarized electrons impinge on an amorphous radiator target, which produce photons via bremsstrahlung.
- One also can generate a **linearly polarized** photon beam by performing coherent bremsstrahlung. Thereby a diamond crystal is used as radiator target, which emits the bremsstrahlung photons only along reciprocal lattice vectors. The emission is called coherent, because of the symmetry of the lattice and the superposition of photons with parallel polarization planes.
- The third type of photon beam, **circularly polarized**, is achieved by impinging longitudinally polarized electrons on an amorphous radiator.

A comprehensive discusion of the generation of polarized photon beams at ELSA is given in [16].

The emitted photons are not monoenergetic but appear with a probability p(E) $\sim$ 1/E. It is essential to know the energy of the generated photon to determine the event kinematic. Therefore an energy tagging detector called tagger (see figure 4) is installed. Since the deflection of a charged particle in a magnetic field is depending on its energy E', and the energy before the bremsstrahlung process E_0 is fixed, the energy of the generated photon E_γ can be calculated via $E_\gamma = E_0 - E'$.

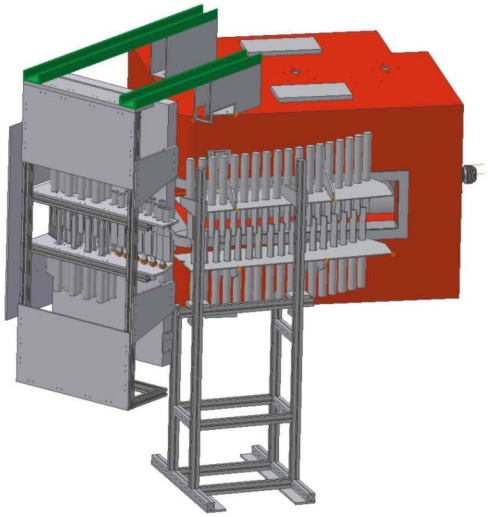

Figure 4: Artificial view of the photon energy tagging system. The deflecting dipole magnet is sketched in red. Electrons enter from the right hand side. The scintillating bars (grey rods) are placed staggered in front of the return yoke's gap. On the left hand side, where higher electron energies are detected, the additional 480 scintillating fibers (covered by an aluminum box) are mounted.

The deflecting of the electrons in a dipole magnet is measured by 96 scintillating bars and 480 scintillating fibers read out by photomultiplier tubes (PMTs).

Targets

During the recent data taking runs 3 different types of target were used:

- Solid state target (Carbon)
- LH_2/LD_2 target
- Longitudinally polarized butanol target

The first one is a cylinder of CH_2 ($\varnothing$ 30 mm, length 30 mm) fixed by a Rohacell clamp at the target point inside the inner detector. It was used especially for measurements of ω in-medium mass modifications.
The liquid hydrogen target[17] serves many applications. Besides measuring the beam asymmetry Σ, it is very important for the energy calibration of the tagger and the calorimeters as well as for the photon flux determination. The target cell (3 cm diameter and 5.1 cm length) is supplied by a horizontal cryostat pointing from the upstream side on the beam axis into the detector system. To provide a neutron target, the hydrogen is replaced by deuterium.
The Bonn frozen Spin Target (BoFroST)[18] is the main production target. It uses also a horizontal cryostat to cool down the doped butanol target cell (2 cm diameter and length) to $\approx$ 20 mK. This extreme low temperature and a magnetic holding field are necessary to prolongate the relaxation time of the externally polarized proton spins. During production beam times every 2 - 3 days the whole detector system is pushed back on a rail system to slide a 1.5 T solenoid over the target cell for repolarization.
A transversally polarized version of this cryostat is also available, which is needed to measure the target asymmetry T.

Detector System

The central and name giving sub detector is the Crystal Barrel electromagnetic calorimeter (see figure 5). Its 1290 CsI(Tl) crystals with lengths of 30 cm (16 X_0) are arranged in a barrel shape[14] around the target point such a way, that all are pointing towards it. The scintillation light is collected at the end surface with wave length shifter, where a PIN[15] photo diode is placed on its side to convert the light into an electrical signal. The analog signal is fed into a charge sensitive preamplifier and a differential driver transmits the signal over 60 m twisted pair cable to a shaper[16]. One output of the shaper is connected to a Fastbus QDC[17], and the second one is going to a discriminator, a latch

[14] Crystals cover a θ and ϕ angle of 6° each. The rings closest to the beam axis have 12° ϕ coverage.

[15] Between the pn junction of the diode is put a layer of insulator, to increase the depletion zone / sensitive detector area.

[16] Analog signals filter to change pulse shape and optimize the signal to noise ratio by cutting the signal in the frequency domain

[17] A charge (**Q**) to **d**igital **c**onverter digitizes the integrated charge during a time gate.

and finally to the **Fa**st **C**luster **E**ncoder (FACE) [19] to provide the trigger with the number of clusters in the calorimeter within less than 10 μs.
The 3 downstream most rings - called *forward plug* - do have the same crystals but a different readout. Here photo multiplier tubes (PMT) and no photo diodes are used. The big advantage of that is the much shorter response time, which provides a fast trigger capability [20]. Since a big fraction of the generated particles are boosted in forward direction, the triggering in this region improves the event selection a lot. The reason that the other crystals are read out by photo diodes is that the calorimeter originally was installed in a magnetic field, where PMTs can not be used.
For the separation of charged and uncharged particles the *inner detector* [21], a scintillating fiber detector surrounding the target, and scintillating tiles [22] in front of the forward plug crystals are installed. The employed organic scintillating material is sensitive to charged particles only.
The opening of the calorimeter in downstream direction is covered by a sec-

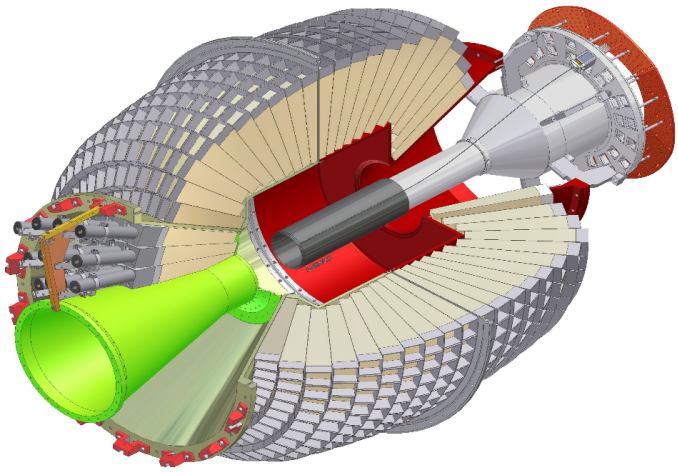

Figure 5: Artificial view of the Crystal Barrel calorimeter with its crystals, the forward plug (left side, around the green cone), and the inner detector (dark grey is the active area) surrounding the target in the middle of the setup.

ond electromagnetic calorimeter, the MiniTAPS detector. It consist of 216 hexagonal BaF_2 crystals read out by PMTs with charged particle veto detectors[18] in front of the crystals.
Between the main calorimeter and the MiniTAPS detector a gas Cerenkov detector is installed. It is a threshold Cerenkov detector, which is sensitive on electrons only. All other types of particles in the momentum region available in the Crystal Barrel experiment do not generate a signal [23]. Thus this detector is used to suppress electromagnetic background on the trigger level.
At the end of the photon beam line the **G**amma **I**ntensity **M**onitor (GIM), a PbF_2 Cerenkov counter, is installed to register all incoming photons. The

[18] Organic scintillators read out via optical fibers and multi channel PMTs.

main purpose is the photon flux determination, but due to its segmentation it also serves as beam position monitor, because the count rate ratios between the detector segments (16 crystals) vary with a moving beam.

Trigger & DAQ

The Crystal Barrel experiment has a triggered and gated **D**ata **Acq**uisition system (DAQ), i. e. the trigger electronics recognizes an interesting event and starts the data acquisition. During the readout and the reset of electronics the trigger is locked, so that no further events are generated. Afterwards the trigger is armed again for the next event.
The trigger logic is separated into two levels. The 1^{st} level collects the information of the fast[19] sub detectors (forward plug, inner detector, MiniTAPS, tagger, GIM, and Cerenkov detector) and searches for selected topologies. If that's the case, the 2^{nd} level is triggered, which determines the number of clusters in the Crystal Barrel calorimeter (FACE) within $10\,\mu s$ and generates either an event signal to start the readout, or a fast_reset signal to clear the electronics. For more details refer to [24].
VME[20] FPGA[21] based modules (see also appendix B) provide the synchronization between the eight CPUs used for the DAQ. This system propagates the current event number and ensures that all systems are ready for data taking before re-arming the trigger. The data packets of every CPU are sent via TCP/IP to a server, which combines the packets to full events, checks data integrity and sends the output file to storage. A detailed description of the recently used DAQ system can be found in [25].

1.2.3 Upgrades of the experimental setup

Citius, altius, fortius...

There are three main upgrades planned for the Crystal Barrel experiment at ELSA in the next time:

- **Trigger capability of the whole calorimeter**
  There is no way to trigger on neutral particles in the main calorimeter (beyond the forward plug) in the first trigger level at the moment. For photoproduction off the proton, the recoil proton is used to generate a trigger signal. But for $\gamma n \rightarrow n\pi^0$ no charged particle is available for triggering. As the current photo diode with its extremely slow charge sensitive preamplifier can not be used to generate a trigger signal, two new readout concepts were investigated:
  - **S**ilicon **P**hoto**M**ultiplier (SiPM): Here a SiPM is added to the wave length shifter of the present readout to generate a trigger signal only, while the energy readout remains the same (photo diode). [26][27]

[19] Not later than 280 ns after the event occurred.
[20] **V**ersa **M**odule **E**urocard bus. Parallel 32 bit bus to control and read out modules via at least one master (CPU).
[21] **F**ield **P**rogrammable **G**ate **A**rray

  - **A**valanche **P**hoto **D**iode (APD): In this scenario the old light readout is completely replaced by an APD with a modern charge sensitive preamplifier to generate a fast trigger signal as well as an energy signal. [28][30]

  The digitization is also going to be changed from simple QDCs to Sampling ADCs, to extracted not only the energy, but also a timing signal, and to detected pile up and base line drifts.

- **Intensity upgrade**
  Since the cross sections of the reactions under investigation are very small and very high statistics are necessary to get profound answers, the required measuring time is also large[22]. The planned intensity upgrade of ELSA will deliver a factor of ten higher luminosity[23] to the experiment. This will decrease the measuring time by the same factor, while the cost will not be affected the same way.
  At least the photon tagging system and the readout of the main calorimeter need to be upgraded from the experimental side to cope with the higher rates. All new detector systems have to be designed to face this intensity upgrade.

- **Inner tracking upgrade**
  The detection of charged particles and their tracks, called *tracking*, has many advantages for the Crystal Barrel experiment:

  - Improve statistics of recently investigated reactions by taking also the decay channels with charged particles into account.
  - Observe new reactions with charged and semi-charged final states.
  - Tagging of strangeness production via detection of secondary vertices.
  - Measurement of particles charge sign and transversal momentum when applying a magnetic field.

According to the physics road map of the Crystal Barrel experiment, the implementation of the first level trigger capabilty of the calorimeter has the highest priority and is therefore going to be realized at first. To dismantel the calorimeter, modify all 1290 crystals, install the new electronics, and reassembly of the whole detector will take between 6 and 12 months. The intensity upgrades of ELSA can go in parallel, because man power of both projects are independent and the downtime of the data taking is decreased.
Implementing the tracking of charged particles in the experimental setup needs more preparation time and it is unlikely to have both upgrades at the same time. It might be possible to install the tracking detector in a first step during the calorimeter upgrade without external magnetic field. In a second step the solenoid could be installed, which corresponds to major installation work in the experimental area, since almost all detectors need to be removed, the support structures need to be modified, and the beam line needs to be changed.

[22] Many hundreds of hours data taking.
[23] Tagged photon rate will increase from $\approx 10\,\mathrm{MHz}$ to roughly $100\,\mathrm{MHz}$.

Before going in further inplementation details, the next chapter explains in detail the advantages of introducing tracking of charged particles in the Crystal Barrel experiment. Different detector concepts are presented and discussed concerning capability and feasibility.

Ignoranti quem portum petat nullus suus ventus est.
Seneca

2 Tracking

2.1 Motivation

There are three main reasons for including tracking of charged particles in the Crystal Barrel experiment, namely:

- Measurement of new quantities of particles (p_t, q, trajectory).
- Increase of detectable decay channels.
- Observation of new reactions.

In the following sections these topics are discussed.

2.1.1 Measurable quantities

The current setup of the Crystal Barrel experiment measures only a single space point of charged particles' trajectories with the inner detector. Assuming the particle to originate from the center of the target, one can reconstruct straight lines and compare it to hits in the calorimeter, which results in an angular resolution of approximately $\sigma_\theta = 1.5°$ and $\sigma_\phi = 0.5°$ [31].
Having now not only a single point, but many space points along the charged particle's track, the angular resolution will improve. Furthermore the assumption that tracks originate from the center of the macroscopic target is not needed anymore.
By reconstructing the tracks of charged particles the primary vertex can be determined in a multi charged tracks event directly with a tracking detector, or if only one charged particle and some photons occur, one can reconstruct the vertex in the offline analysis taking the tracking detector and the calorimeter into account.
Especially in hyperon[24] decays, where the typical reach $c\tau$ is in the order of some dozens of millimeters, secondary vertices appear inside the tracking detector and are clear signatures for strangeness. In table 1 the detection ef-

Detection efficiency η	90%	95%	98%	99%	99.5%
Resolution σ_z [mm]	7.69	3.74	1.48	0.734	0.37

Table 1: Needed longitudinal resolution σ_z to achieve the desired detection efficiency η for Λ decays originating from the Σ^0 decay in the reaction $\gamma p \to K^+\Sigma^0$.

ficiency for observing the Λ decay in the reaction $\gamma p \to K^+\Sigma^0$, where the Σ^0 decays into $\gamma\Lambda$, is shown with the required resolution along the z axis (beam axis) σ_z to obtain the secondary vertex. The data is coming from a GEANT4[25]

[24] Hadron containing at least one s-quark like $K, \Sigma, \Lambda, \Xi, \ldots$
[25] Simulation framework, see for details *www.chern.ch/geant4*.

simulation of photons with a bremsstrahl spectrum between 1.5 and 3.5 GeV hitting on a liquid hydrogen target.
Applying a magnetic field in addition, which deflects charged particles, enables the determination of transversal momenta p_t from the bending radius and the sign of the particle's charge out of the spiralization direction.

2.1.2 Increasing of the detectable decay channels

Recent experiments with the Crystal Barrel setup are photoproduction of neutral mesons like $\pi^0, \eta, \omega, \eta'$. Only decays of these mesons in neutral final states, i. e. photons, are investigated up to now. When taking also decay modes with charged particles in the final state into account, the statistics can be improved as listed in table 2. For example the number of detected ω mesons can be increased almost by a factor of 11 by using the charged decay modes as well. The overall efficiency of the setup will improve by measuring the neutral and

Reaction	BR(neutral)	BR(charged)	Gain
$\gamma p \rightarrow p\omega$	9.3%	90.7%	≈ 11
$\gamma p \rightarrow p\eta'$	22.8%	77.2%	≈ 4
$\gamma p \rightarrow p\eta$	71.2%	28.8%	≈ 1.3

Table 2: Branching ratios of recently investigated reactions for neutral and charged final states. In addition the gain is noted when taking decay channels with charged particles as well into account.

charged final states in parallel. This means more information is contained in the data of a beam time and the ratio beam time (costs) / analysis is becoming smaller, i. e. for same costs and shifts more students can be provided with data for an analysis.

2.1.3 Newly observable reactions

Beside the improvement in statistics for reactions already under investigation, detecting charged particles' tracks also opens the field of new reactions, which can not be observed with the current setup of the Crystal Barrel experiment. Especially the observation of Λ and Σ hyperons are of great interest, because of their self-analysing power. The azimuthal angle ϕ distribution between photon polarization plane and the hyperon decay plane can be used to extract the recoil polarization observables P, $O_{x'}$, $C_{x'}$, and T according to [11] and [12]. Taking the unpolarized cross section σ_0, the beam asymmetry Σ, and the G observable, which all can be measured already with the current setup, and adding the H observable from measurements with a transversally polarized target[26], a complete experiment [13] for hyperons can be performed. This could be the first complete experiment ever done.
Precise data of η' decays are needed to resolve the different ρ meson contributions and to extract the light quark mass difference m_d - m_u. Therefore the

[26] A transversally polarized target will be available in 2010 for the Crystal Barrel experiment.

decay widths of the η' decays into $\pi^0\pi^+\pi^-$ and $\eta\pi^+\pi^-$ need to be measured very accurately [29]. These measurements require a very good detection efficiency for neutral and charged particles, which will be available in the Crystal Barrel experiment including the tracking upgrade.

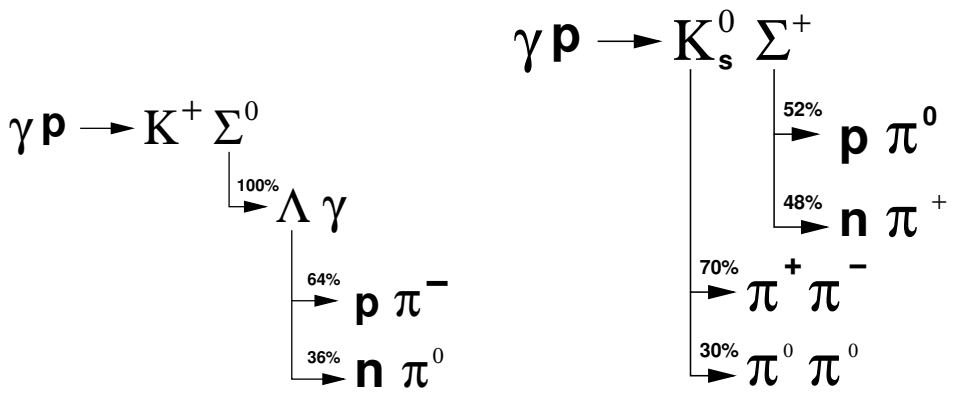

(a) (b)

Figure 6: Decay scheme for $\gamma p \to K^+\Sigma^0$ (a) and $\gamma p \to K_s^0\Sigma^+$ (b) with branching ratios for different decay modes, if particles decay within the detector.

Two further interesting reactions, which need the detection of charged and neutral particles at the same time, with their decay modes are shown in figures 6(a) and 6(b). In the reaction $\gamma p \to K^+\Sigma^0$ the K^+ can be considered as stable for our purpose, since $c\tau > 3.7\,\mathrm{m}$. Finally one ends up with $K^+p\pi^-\gamma$ or $K^+n3\gamma$, which shows, that the detection of charged and neutral particles is necessary.
For the second reaction ($\gamma p \to K_s^0\Sigma^+$) the 2 secondary vertices are clear indicators, because both produced hyperons have a $c\tau \approx 2.5\,\mathrm{cm}$. The dominant channel into $p\pi^+\pi^-\pi^0$ is identical to the most prominent decay of the ω meson, but the detection of the secondary vertices enables a good separation. The same is true for the final state $p3\pi^0$, which also occurs in the η production ($\gamma p \to p\eta \to p3\pi^0$).

Summing up there are many reasons for including tracking of charged particles into the Crystal Barrel experiment:

- Precise measurement of tracks including angles and primary vertex.
- Increasing the observable fraction of decay channels.
- Investigation of new reactions with pure or semi charged final states.
- Capability of tagging strangeness via detection of secondary vertices.
- Measuring recoil polarizations of hyperons and having that way a complete experiment.

2.2 Phase space simulations

To fix the specifications of a detector in general and especially for tracking detectors, it is essential to know the angular distribution and the energy / momentum of the particles to be observed.
The following two reactions are used to perform phase space (kinematics) simulations:

1. $\gamma p \rightarrow p\omega \rightarrow p\pi^+\pi^-\pi^0$
2. $\gamma p \rightarrow K^+\Lambda \rightarrow K^+p\pi^-$

The simulations are performed by using the *TGenPhaseSpace* package of the root[27] framework. The incident photons impinging on a proton target have an approximated bremsstrahl spectrum, i. e. 1/E distribution between production threshold and 3.5 GeV (see figure 7(a)).

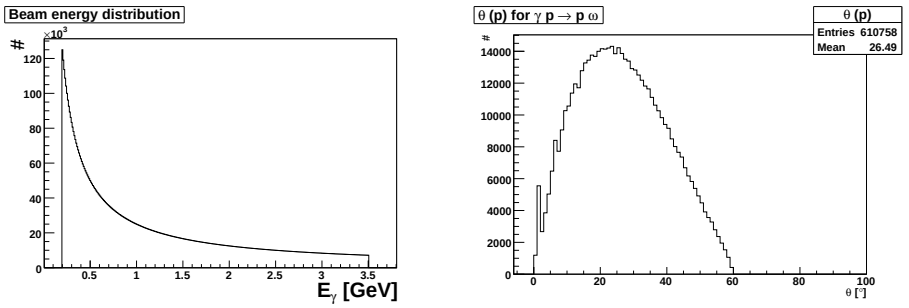

(a) E_γ distribution (b) θ of proton in $\gamma p \rightarrow p\omega$

Figure 7: a)1/E photon beam energy distribution used for the simulation. b) Polar angle distribution of the proton in $\gamma p \rightarrow p\omega$.

In table 3 the maxima and mean values of the angular distribution of all charged particles for the simulated reactions are listed.

$\gamma p \rightarrow p\omega \rightarrow p\pi^+\pi^-\pi^0$					
θ_{max}(p)	θ_{mean}(p)	$\theta_{max}(\pi^+)$	$\theta_{mean}(\pi^+)$	$\theta_{max}(\pi^-)$	$\theta_{mean}(\pi^-)$
60°	50.27°	180°	48.53°	180°	48.53°
$\gamma p \rightarrow K^+\Lambda \rightarrow K^+p\pi^-$					
θ_{max}(p)	θ_{mean}(p)	$\theta_{max}(K^+)$	$\theta_{mean}(K^+)$	$\theta_{max}(\pi^-)$	$\theta_{mean}(\pi^-)$
60°	28.1°	180°	45.1°	180°	35.8°

Table 3: The maxima and mean values of the polar angle distribution of charged particles for given reactions.

→ The proton stays always in the forward direction ($\theta < 68°$).

→ Lighter particles like pions and kaons occurr also in backward direction.

[27] Widely used C++ analysis framework for particle and high energy physics. See *http://root.cern.ch*

A realistic tracking detector cannot cover the full polar angle range, but has a minimal θ_m, where particles only with $\theta > \theta_m$ are detected. The detection efficiencies for various θ_m and reactions are registered in table 4.

reaction	$\theta_m = 0°$	$\theta_m = 5°$	$\theta_m = 10°$	$\theta_m = 15°$	$\theta_m = 20°$	$\theta_m = 25°$
$p\omega$(p)	1	0.771	0.708	0.621	0.519	0.412
$p\omega(\pi^{\pm})$	1	0.785	0.761	0.717	0.663	0.602
$K^+\Lambda$(p)	1	0.98	0.922	0.834	0.723	0.597
$K^+\Lambda(K^+)$	1	0.987	0.948	0.889	0.816	0.735
$K^+\Lambda(\pi^-)$	1	0.977	0.913	0.823	0.721	0.616

Table 4: Detection efficiency of charged particles from different reactions after applying minimal polar angle cuts. Particles in brackets are the investigated ones.

In case of the $p\omega$ reaction for example a cut on the polar angle of 10° causes a reduction of the detection acceptance by 30%.

→ Detection efficiency is very sensitive on θ_m, i. e. polar angular coverage of the detector.

⇒ θ_m has to be as small as possible to have a good acceptance. From mechanical and geometrical point of view polar angles of less than 15° seem not to be feasible. The coverage in backward direction is not that crucial, but to match with the calorimeter a maximal polar angle of 160° would be desirable.

Besides the polar angle also the transversal momentum p_t distributions are simulated. To measure p_t and the sign of the charge of a electrical non neutral particle, a magnetic field is used. The curvature of the trajectory determines the momentum, while the bending direction reveals the sign of the particle's charge.
For that purpose a solenoid will be installed around the calorimeter to cover the whole central detector setup, deflecting charged particles in the tracking detector. The former CB@LEAR return yoke will be reused, but replacing the normal conducting solenoid by a super conducting one, with a higer magnetic field strength (up to 3 T) and a much lower electrical power consumption (from MW to some kW).

In figure 2.2 the p_t distribution for the proton in the simulated reaction $\gamma p \rightarrow p\omega$ with a 1/e Bremsstrahlung spectrum up to 3.5 GeV photon energy is plotted. Figure 2.2 shows the correlation between the polar angle and the transversal momentum.
The mean and maximum values of the transversal momentum distributions are listed in table 5.

→ Maximal transversal momentum $p_t^{max} \leq 1.2\,\mathrm{GeV/c}$.

⇒ Fixing the magnetic field strength if the detector point resolution is known according to the desired momentum resolution.

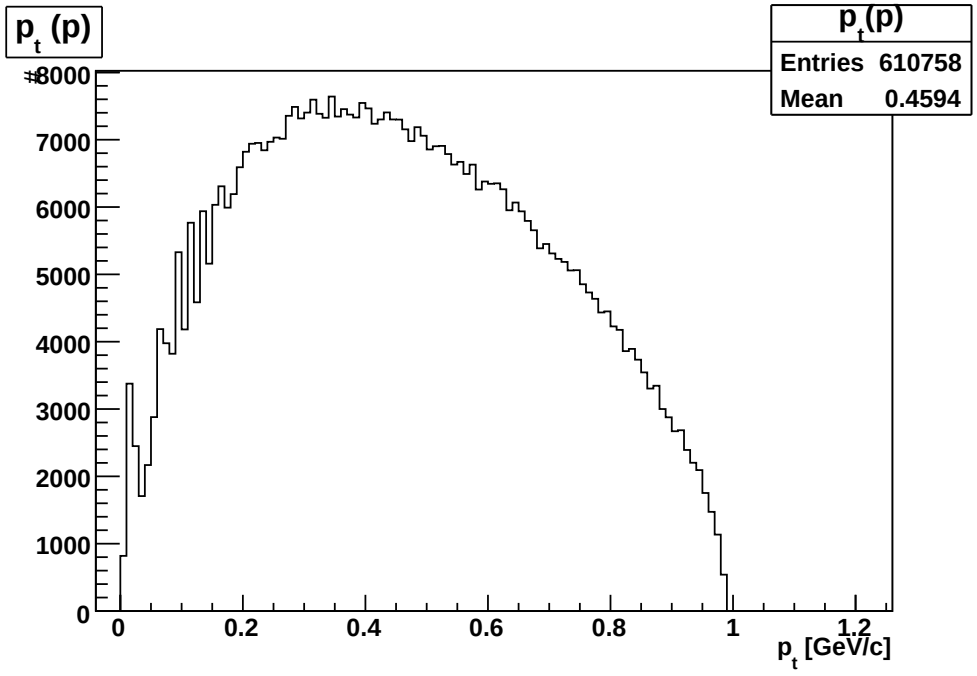

Figure 8: Simulated transversal momentum distribution of the proton from ω production for a Bremsstrahlung spectrum up to 3.5 GeV.

$\gamma p \to p\omega \to p\pi^+\pi^-\pi^0$					
$p_t^{max}(p)$	$p_t^{mean}(p)$	$p_t^{max}(\pi^+)$	$p_t^{mean}(\pi^+)$	$p_t^{max}(\pi^-)$	$p_t^{mean}(\pi^-)$
990 MeV/c	459 MeV/c	950 MeV/c	232 MeV/c	950 MeV/c	232 MeV/c

$\gamma p \to K^+\Lambda \to K^+p\pi^-$					
$p_t^{max}(p)$	$p_t^{mean}(p)$	$p_t^{max}(\pi^-)$	$p_t^{mean}(\pi^-)$	$p_t^{max}(K^+)$	$p_t^{mean}(K^+)$
1 GeV/c	533 MeV/c	300 MeV/c	120 MeV/c	1 GeV/c	626 MeV/c

Table 5: Transversal momentum distribution of charged particles for the different reactions.

An overall relative momentum resolution of 10% seems to be feasible in comparison to similar experiments like WASA [34]. Details concerning these simulations and further plots can be found in appendix A.

2.2.1 Resulting specifications

The results from above phase space simulations are employed to fix the specifications of the tracking detector.

1. $\theta_m \leq 15°$
2. $\theta_{max} \geq 160°$
3. Longitudinal space resolution $\sigma_z \leq 1\,\text{mm}$
4. Transversal momentum resolution $\sigma_{p_t}/p_t \approx 10\%$

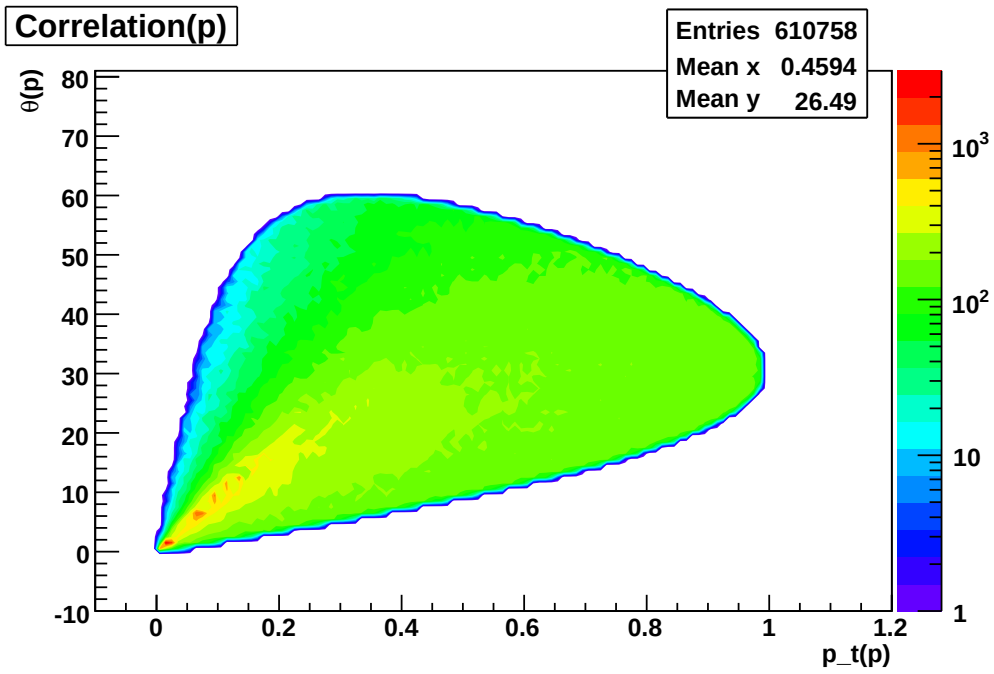

Figure 9: Simulated correlation between transversal momentum and polar angle of the proton in $\gamma p \rightarrow p\omega$. The highest p_t appear at angles with maximal track length in the available active volume, which improves the resolution.

The first point is very important for the detector. As shown in table 4, the detection efficiency is very sensitive to the minimal polar angle which can be observed (θ_m). Since there are no ideal detectors ($\theta_m = 0°$) a trade-off has to be done. At 15° the overall detection efficiency is 79.8%. Even in the worst case of the proton in $\gamma p \rightarrow p\omega$ the efficiency is 62.1%, which is still acceptable, but larger θ_m should be avoided.
With a polar angle coverage up to 160° all particles hitting the calorimeter also have to go through the tracking detector. As shown most charged particles go in forward direction, only light particles like pions and kaons occur with $\theta > 160°$, but the efficiency losses are negligible.
A longitudinal space resolution σ_z of 1 mm corresponds to a 98.5% probability to detect Λ decays via secondary vertex.

2.3 Constraints for tracking

First of all one has to consider that the tracking detector has to fit inside the existing Crystal Barrel calorimeter and the space for the production targets has to be kept free - see figure 10. This results in the following geometrical constraints:

- Inner bore for the targets: $\varnothing_i \geq 105\,\text{mm}$.
- Outer diameter $\varnothing_o \leq 310\,\text{mm}$ if the detector sticks out of inner volume.

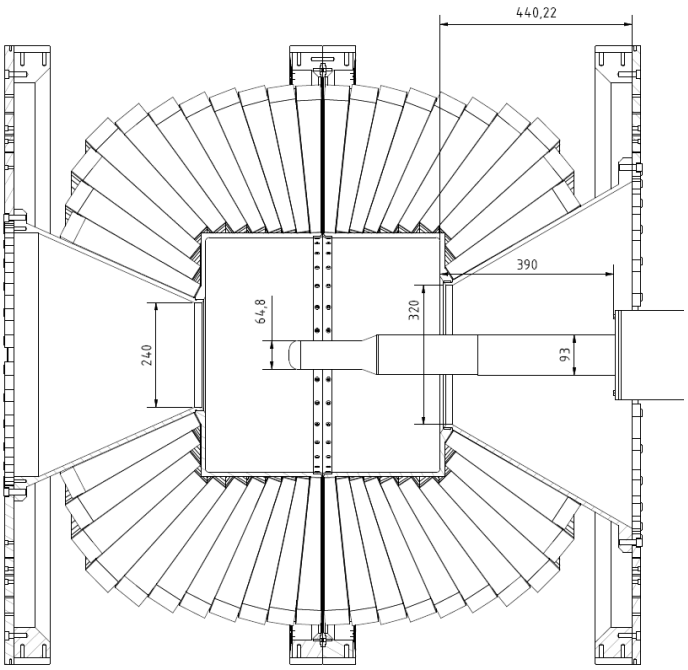

Figure 10: Cross section of the Crystal Barrel calorimeter with the target cryostat entering from the right hand side. The tracking detector can cover almost the whole volume between target and calorimeter.

Beside the geometrical constraints there are more things to take into account:

- Since the whole detector setup is ϕ symmetric[28], the tracking detector should also provide rotational symmetry.
- The detector has to have a minimal material budget ($\lesssim 1\%$ X_0) to minimize the conversion probability of photons and the scattering of particles.
- Due to very small breakouts in the magnet's return yoke the amount of cables and supply lines is limited.
- The tracking detector should be operated at room temperature, because condensation water would destroy the hygroscopic CsI(Tl) crystals of the calorimeter.

2.4 Tracking detectors

When the abstract properties are fixed, the next step is to look for real implementation options.
In high energy physics the tracking detector subsystem is composed of different tracking detectors, which are specialized to certain tasks. Closest to the interaction point a fine granular layered detector is located to deliver high resolution points for primary and secondary vertices detection. For a good

[28] Azimuthal angle symmetry, i. e. invariant for rotations along beam axis.

momentum resolution many reconstructed space points are needed. Typically gas detectors fullfill this task.
Due to limited space for tracking inside the Crystal Barrel calorimeter, both competing jobs should be combined within a single tracking detector.

In the following subsections three detector concepts for a tracking detector are shown and their feasability is discussed.

2.4.1 Silicon strip detector

An inner tracking detector built out of some layers of silicon strip detectors arranged in concentrical cylinders is common in high energy physics experiments like ALICE [35], ATLAS [36], and CMS[37] but will also be implemented in hadron physic experiments like $\bar{P}ANDA$[29].
The basic idea of semiconductor detectors is to have a reversed biased diode, i. e. maximal extended depletion zone, where no free charge carriers are present. An incident charged particle ionizes atoms in the depletion zone and the charges propagate to cathode or anode. This generated charge is amplified in a charge sensitive preamplifier to a voltage signal for further processing. To obtain a position information these detectors are segmented in the mm to μm range.
To detect spiraling particles at least 4 layers of silicon strip detectors should be used. Corresponding to the constraints from section 2.3 one can design such a detector with cylinder diameters $\varnothing = \{105\,\text{mm}, 150\,\text{mm}, 200\,\text{mm}, 250\,\text{mm}\}$ with length $l_z = \{400\,\text{mm}, 570\,\text{mm}, 756\,\text{mm}, 945\,\text{mm}\}$ to achieve $\theta_m = 15°$. An adequate strip size would be $200\,\mu m$ x 20 mm. With this one can estimate the number of strips per cylinder / barrel to $n_i = \{47.7\text{k}, 96.7\text{k}, 171\text{k}, 267\text{k}\}$ with the assumption that 20% more strips than the cylinder surface requires are used, due to overlapping and staggering tilt chips along the radius. But these strips would deliver only a resolution in ϕ (azimuthal angle) and hardly no information in z or θ. Therefore one needs stereo strips typically perpendicular to the first ones. This means the amount of strips has to be doubled, so one ends up with approximately 1.2 million strips.

Ordinary silicon detectors have a thickness of at least $300\,\mu m$, so with four layers one has 1.2 mm silicon. This corresponds to 13% X_0, where the radiation length in silicon is $X_0 = 9.36\,\text{mm}$. In addition there needs to be a support structure (carbon fiber compound), cooling pipes, front end electronics as well as cables for power supply, bias voltage, and signals. Experience shows that the overall material budget for supply and support structures is between 5 and 10% X_0, which is much bigger than the design goal of 1% X_0. This would lead to a higher conversion rate of photons and more multiple scattering for particles.
Four space points are sufficient to fit a track, but to determine particle's transversal momentum, i. e. fitting the bending radius, is hardly feasible.

[29] Anti Proton Annihilation Darmstadt, $\bar{p}p$ experiment in progress located at GSI in Darmstadt

Pros	Cons
Very high granularity	Huge amount of channels
High rate / occupancy capable	High material budget
Very good point resolution	Poor p_t resolution

2.4.2 Spiral Projection Chamber

A **S**piral **P**rojection **C**hamber (SPC) is a radial drift chamber. Figure 11 shows a sketch of a cross section of SPC, where the electric field is pointing from the inner drift cathode to the outer wall. The field wires (blue dots) focus the drifting electrons onto the signal wires, where the gas gain occurs, before signal detection. Due to a longitudinally applied magnetic field the drifting electrons from ionization processes along charged particles' tracks move along bended trajectories (spirals).
One can determine the azimuthal angle by fitting the center of gravity of the signal wires. The z-resolution is coming from the charge division method, where the signal wire is read out on both ends (q_1, q_2). The actual position is then given by $z = L\frac{q_1}{q_1+q_2}$, with L beeing the total wire length. The time between the signal occurs on the signal wire and external start is used to determine the drift length and therefore the radius, where the primary ionization had taken place.
SPCs were successfully used in experiments like ASTERIX[38] and OBELIX[39]

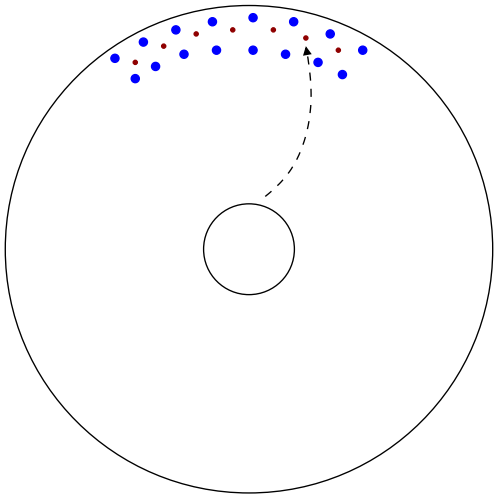

Figure 11: Sketch of a SPC with drift cathode (inner cylinder), outer wall, signal wires (red dots), field wires (blue circles), and drift electron's path (dash arrow).

at CERN. Here the detectors are called **X**-ray **D**rift **C**hamber (XDC), because they did another job in parallel, namely the detection and energy determination of X-rays, which were emitted by $p\bar{p}$ pairs to decay into ground state before annihilation. For that special purpose the inner cathode was manufactured from a $6\,\mu m$ thick aluminized capton foil, to prevent the X-rays to be absorbed before entering the active gas volume.
The ASTERIX SPC achieves with its 90 wires and 30 MHz Sampling ADC

readout a transversal resolution of $\sigma = 400\,\mu m$ [32]. The successor XDC of OBELIX was equipped with 100 MHz Flash-ADCs and a segmented cathode. This setup achieves $\sigma_z = 1\,\text{mm}$, $\sigma_{r\phi} = 500\,\mu m$, and an energy resolution of 18% FWHM at 5.5 keV for ^{54}Mn X-ray spectrum [40].
SPCs got out of focus nowadays, because of their limited rate capability. Due to the low number of the readout channels, the occupancy is high, which limits the detector efficiency. However, for the Crystal Barrel experiment this would not be an issue, since the maximum rate of charged particles entering the active volume including background like compton scattering and e^+e^- pair production is not higher than 2 kHz [33].

Pros	**Cons**
Extreme low material budget	Readout on up- and downstream face
Simple and flexible mechanics	Can not stand very high rates
Few (≈ 100) readout channels only	
Good dE/dx resolution	

2.4.3 Time Projection Chamber

A **T**ime **P**rojection **C**hamber (TPC) is a longitudinal drift chamber with parallel electric and magnetic fields ($\vec{E} \parallel \vec{B}$) [41]. A sketch of a TPC is shown in figure 12.
Charged particles traversing the TPC drift volume ionize the drift gas along their tracks. These primary electron clusters drift to the readout anode, are amplified in the amplification stage, and are finally detected with 2 dimensional position sensitive detectors. The drift time of the clusters is used to determine the longitudinal coordinate (z-axis). Together with the xy-coordinates from the position sensitive detectors one gets 3 dimensional cluster origins, which are then used to reconstruct the particles' tracks.

In case of a TPC a magnetic field does not only serve to bend the charged particles trajectories, but also reduces the transversal diffusion of the electron clusters, because of their cyclotron oscillations around the drift vector. With this technique drift lengths of several meters are possible and already implemented for example in the ALICE TPC [42].
The energy deposition dE/dx in the chamber is depending on the particle type and in combination with the measured momentum particle identification (PID) can be performed up to $p_t \approx 1\,\text{GeV/c}$.
Former TPCs used wires to generate the amplification similar to multi wire proportional chambers (MWPC) and a gating wire grid in front to minimize the ion back drift into the drift volume, since during the amplification process not only electrons are set free, but also the same amount of ions. This gating grid introduces a deadtime, because drifting charges do not overcome this barrier.
One way to overcome this is to use an amplification stage with internal ion supression. Gaseous Electron Multipliers (GEMs) for instance are such devices. In principle it is a copperized Mylar foil ($50\,\mu m$ thickness) with a fine grid of etched holes (pitch $\approx 125\,\mu m$). Applying a voltage difference between

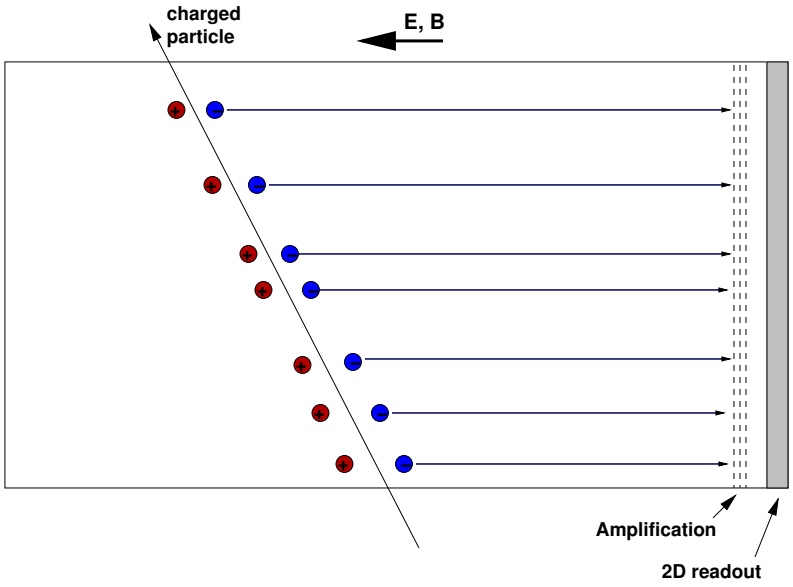

Figure 12: Schematic drawing of a TPC, with a charged particle crossing the active volume.

both sides produces a high electrical field in the holes, so that the process of gas amplification takes place. Since most of the electric flux lines end at the GEM foil surface, the ions from gas amplification are guided to the foil surface, where they recombine and become neutralized. GEMs as amplification stage make gating dispensable, so a continous operation of the TPC becomes possible.

Due to long drift times of dozens of μs event mixing occurs already at moderate rates (some kHz), which means, that at the readout plane clusters appear in coincidence, while the corresponding tracks arise from different events. This means a simple time cut to separate an event is not feasible.
The classical way to operate a TPC is to get an external trigger, record all pads for at least one full drift periode, and extract the correct tracks.
Another way would be a continous readout without external trigger, but a higher level data processing, which recognizes tracks and stores their features(time, helix fit, dE/dx) as proposed for the $\bar{P}ANDA$ experiment[30], needs to be implemented to reduce the amount of data.

Pros	**Cons**
Very low material budget	Long drift time (event mixing)
Only single side readout necessary	Needs very good $\vec{E}$ and $\vec{B}$ fields
High rate capability	Very sensitive on v_{drift} variations
Low dead time possible	

[30] See *www-panda.gsi.de.*

2.5 Comparison of tracking detector options

The transversal momentum resolution σ_{p_t} is one of the central parameters to compare tracking detectors. Therefore a model to determine σ_{p_t} is shown and its application on the previous discussed tracking detectors is presented.
R. L. Glückstern developed in his paper [43] a parametrization of the track curvature error Δc, which is given by

$$\Delta c = \frac{\sigma_x}{L^2}\sqrt{\frac{720}{N+5}}, \tag{1}$$

where σ_x is the point resolution perpendicular to the track projection (xy-plane), L is the projected track length onto the plane perpendicular to the magnetic field (xy-plane), and N is the number of space points used to determine the curvature. Actually the formular works only for large N. But there is also a small N approximation.
The transversal momentum of particle with charge q = ± e is given by

$$p_t = 0.3 \cdot BR, \tag{2}$$

with R being the bending radius of the trajectory in a magnetic field with field strength B. The curvature c is the inverse radius (c = 1/R), so $p_t = \frac{0.3 \cdot B}{c}$. Assuming a constant homogenous magnetic field, the error on B (ΔB) vanishes and with gaussian error calculation on equations 1 and 2 one gets for the error on the transversal momentum:

$$\Delta p_t = \frac{0.3 \cdot B}{c^2}\frac{\sigma_x}{L^2}\sqrt{\frac{720}{N+5}}.$$

The relative error can then be written as:

$$\frac{\Delta p_t}{p_t} = \frac{\sigma_x}{L^2}\frac{p_t}{0.3 \cdot B}\sqrt{\frac{720}{N+5}}. \tag{3}$$

As one can see in equation 3, the most important parameter is the projected track length L, because it enters in the resolution quadratically. The position resolution σ_x and the magnetic field strength B contribute linear to the relative resolution. Even if N contributes only like $1/\sqrt{N}$, it is important to have many track points for the curvature fit.

Fitting a helix on three space points only is not a bijective operation, since a helix in general has at least 5 parameters.
The track reconstruction without any further information does not work for the four silicon strip layer detector concept, therefore and in combination with the hugh amount of channels this detector concept is not an option for the Crystal Barrel tracking detector.

2.5.1 Projected track length parametrization

Since the orientation of the magnetic field is the same for SPC and TPC and both do have a cylindrical shape, the calculation of the projected track length

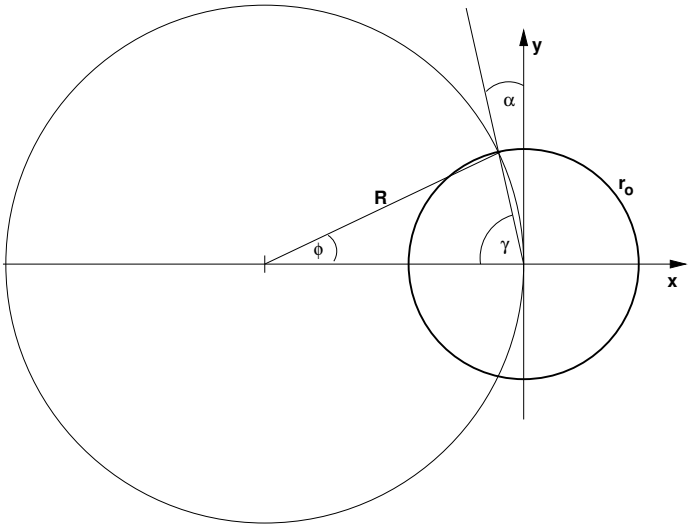

Figure 13: Sketch of detector xy-projection (thick line circle) and a particles trajectory (thin line circle).

L is the same for both. The following calculations neglect diffusion, multiple scattering, and field inhomogeneities.

In figure 13 the xy-projection of the detector is sketched. The outer radius of the detector r_o (thick line), and the trajectory of a bend particle (thin circle) with radius R are shown.

L is now the length of the circle segment of a particle's circle between origin and the crossing of both circles. Using angle ϕ the track length can be written as $L = \phi \cdot R$. The angle ϕ can be expressed by both radii: $\phi = 2 \cdot \arcsin(r_o/2R)$. There are two corrections one has to take into account. First of all the detectors are not full cylinders, but have an inner bore with radius r_i to fit around the target. L has to be reduced by the track length, which is not contained in the active volume, i. e. for $r < r_i$. Now L can be written as:

$$L = (\phi - \phi_i) \cdot R,$$

with $\phi_i = 2 \cdot \arctan(r_i/2R)$.

The second correction needed to be integrated is the finite length of the detector. Thus particles leave the active volume not through the outer cylinder surface, but the face surface. This means the r_o depends on the polar angle θ, $r'_o = min\{r_o; l/2 \cdot \tan\theta\}$ with $l/2$ being the distance between target point and downstream end of the detector. So finally one gets

$$L = \big(\arcsin(r'_o/2R) - \arcsin(r_i/2R)\big) \cdot 2R.$$

The parameters to determine L are p_t, θ, B, r_i, r_o, $l/2$. All other quantities can be derived from these.

The determination for the number of track samples N is different for both detectors, because the SPC measures z and ϕ and the TPC x and y.

2.5.2 Parametrization of a SPC

Each of the n_w signal wires in a SPC covers an azimuthal angle $\delta\phi = 2\pi/n_w$. Thus naively N can be determined just by division of the deflection angle α and $\delta\phi$.

$$N = \frac{\alpha}{\delta\phi}. \tag{4}$$

Actually many clusters are generated by the charged particle in the drift gas, which induce individual signals on the signal wires. Due to drift velocities in the order of μs/cm and sampling rates of appoximately 100 MHz, the distance between drifted charge and sense wire can be determined better than the sense wire pitch, what leads to an improved ϕ resolution compaired to $\delta\phi$. Therefore N is under estimated in formular 4, but it will be used for further calculations.

2.5.3 Parametrization of a TPC

Assuming to have hexagonal pads with diameter d, the number of samples along L can easily be calculated by

$$N = L/d.$$

This formular is only true if at least one cluster hits each pad on the projected track. If the pad size is too small, then it will happen that some pads are not seeing a cluster and don't contribute to N. But on the other hand, due to diffusion and broadening during amplification, a single cluster induce signals not only on a signal pad.
For simplicity the simple formular for N is used for the following studies.

2.5.4 Model cross check with simulations

To make sure the model is working properly and the generated predictions correspond to reality it is necessary to test the model for a known scenario. Comparison with measurements would be the first choice, but also simulation results can be used.
In [44] S. Neubert presents simulation results for the $\bar{P}ANDA$ TPC, which are compared to the corresponding model predictions. The following parameters are used for the calculations:

r_i	0.15 m
r_o	0.4 m
d	0.002 m
l/2	1.1 m
B	2 T
σ_x	$1.5{\cdot}10^{-4}$ m

The model predictions are listed in table 6 and the results are reasonable. They are of the same order of magnitude and the general behavior matches.

$\theta[^\circ] \setminus p_t$[GeV/c]	0.2	0.4	0.6	0.8	1	1.2
10	0.123	0.2619	0.3974	0.532	0.6662	0.8
15	0.062	0.014	0.0215	0.0289	0.0362	0.0435
20	0.0015	0.0036	0.0055	0.0074	0.0093	0.0112
30	0.0015	0.0036	0.0055	0.0074	0.0093	0.0112
40	0.0015	0.0036	0.0055	0.0074	0.0093	0.0112
50	0.0015	0.0036	0.0055	0.0074	0.0093	0.0112
60	0.0015	0.0036	0.0055	0.0074	0.0093	0.0112
70	0.0015	0.0036	0.0055	0.0074	0.0093	0.0112
80	0.0015	0.0036	0.0055	0.0074	0.0093	0.0112
90	0.0015	0.0036	0.0055	0.0074	0.0093	0.0112

Table 6: Relative transversal momentum resolution predicted by the above developed model for the $\bar{P}ANDA$ TPC constraints.

In contrast to the model the simulation includes diffusion of the drifting clusters, i. e. σ_x is not a constant, but varies with z. Therefore tracks with smaller polar angles having a longer drift distance to the readout plane, have a better relative transversal momentum resolution in the model than the simulation. This behavior can be observed:

$\theta[^\circ]$	20	30	40	50	60	70	80	90
$\frac{\Delta p_t}{p_t}$ Model/Sim.	0.44	0.72	0.78	0.85	1.17	1.33	1.87	2.07

Here $\theta = 0^\circ$ is the downstream direction and the readout is located on the upstream side of the TPC (at $\theta = 180^\circ$).
Model and simulation fit together, but the neglected effect of diffusion introduces a systematic error of 50% to the model. Since the diffusion is linear in the drift length and the detectors under investigation for the Crystal Barrel experiment have only a third of the dimensions of the $\bar{P}ANDA$ TPC (l/2 1.1 m $\rightarrow$ 0.3 m), the systematic error due to diffusion disregard is only $\approx$16.5%.

The model also has to be tested for a constant angle but with variable transversal momentum p_t. In the following table again the ratio between model prediction and simulation results is listed versus p_t:

p_t[GeV/c]	0.2	0.4	0.6	0.8	1	2	3	4	5	6	7
$\frac{\Delta p_t}{p_t}$ M/S	0.1	0.3	0.61	0.99	1.17	1.71	5.88	6.27	6.45	6.27	6.59

Obviously there is a discrepancy between model prediction and simulation result. For low p_t the resolution in the simulation suffers from multiple scattering in the included micro vertex detector[31], what leads to very small ratio $\frac{model}{simulation}$. On the other side at high p_t, where the deflection is very small, the additional track points from the MVD and the much improved lever arm let the simulation get 6 times better than the model prediction, which does not include additional tracking detectors.

[31] Panda Micro Vertex Detector (MVD) is a multilayer barrel shaped silicon pixel and strip detector.

When decreasing the inner radius in the model, the resolution for high transversal momenta gets compatible with the simulation, because more track points are generated.
However, the model seems to work and describes the general dependency of the resolution on geometrical and detector specific parameters quite well. When looking for short drift lengths the diffusion disregard can be compensated in a systematic error of below 20%. The dependency on p_t can not be compared easily, since the simulation includes another tracking detector, which generates on the one hand side multiple scattering and on the other hand side delivers additional precise track points.
The model is a good tool to estimate the transversal momentum resolution of tracking detectors, although it uses just simple calculations performed in a spreadsheet, but not a bulky simulation.
The aim of this model is not to replace simulations, but to study the dependency of the resolution on different design parameters more quickly and flexible.

2.5.5 Model results for Crystal Barrel constraints

Common parameters for both detectors are:

r_i	5 cm
r_o	15 cm
l/2	30 cm
B	2 T

Now the model prediction for the transversal momentum resolution for the TPC and the SPC are presented and compared to each other. Possible improvements on the detectors and their consequences are discussed as well.

Results for TPC model

d	2.5 mm
σ_x	150 μm

The model prediction presented in table 7 show a $\frac{\Delta p_t}{p_t}$ between 2 and 12% for polar angles bigger than 25°. The resolution for particles appearing in smaller angles worsen quickly. For $\theta < 20°$ serious momentum determination is not possible.

Results for SPC model

Wires	90
σ_x	300 μm

$\theta \setminus p_t$	0.2 GeV/c	0.4 GeV/c	0.6 GeV/c	0.8 GeV/c	1 GeV/c	1.2 GeV/c
15°	0.347	0.700	1.051	1.403	1.754	2.105
20°	0.07	0.142	0.214	0.286	0.357	0.429
25°	0.025	0.052	0.078	0.104	0.130	0.156
30°	0.0194	0.040	0.06	0.08	0.1	0.12
40°	0.0194	0.040	0.06	0.08	0.1	0.12
50°	0.0194	0.040	0.06	0.08	0.1	0.12
60°	0.0194	0.040	0.06	0.08	0.1	0.12
70°	0.0194	0.040	0.06	0.08	0.1	0.12
80°	0.0194	0.040	0.06	0.08	0.1	0.12
90°	0.0194	0.040	0.06	0.08	0.1	0.12

Table 7: Model prediction for relative transversal momentum resolution $\frac{\Delta p_t}{p_t}$ of a TPC meeting the Crystal Barrel constraints.

$\theta \setminus p_t$	0.2 GeV/c	0.4 GeV/c	0.6 GeV/c	0.8 GeV/c	1 GeV/c	1.2 GeV/c
15°	1.11	2.39	3.69	4.99	6.28	7.58
20°	0.28	0.61	0.95	1.29	1.64	1.98
25°	0.11	0.26	0.41	0.55	0.7	0.85
30°	0.09	0.21	0.33	0.44	0.56	0.68
40°	0.09	0.21	0.33	0.44	0.56	0.68
50°	0.09	0.21	0.33	0.44	0.56	0.68
60°	0.09	0.21	0.33	0.44	0.56	0.68
70°	0.09	0.21	0.33	0.44	0.56	0.68
80°	0.09	0.21	0.33	0.44	0.56	0.68
90°	0.09	0.21	0.33	0.44	0.56	0.68

Table 8: Model prediction for relative transversal momentum resolution $\frac{\Delta p_t}{p_t}$ of a SPC meeting the Crystal Barrel constraints.

With these parameters the SPC delivers a roughly five times worse p_t resolution than the TPC, but due to its flexible mechanics there are a lot of tuning parameters.
In contrast to the TPC the cross section along the z-axis does not need to be constant, but the inner bore can be decreased downstream the target. Going from $r_i = 5\,\text{cm}$ to 1 cm the resolution improves by a factor of 2 for big angles and a factor of 5 for small angles ($\theta \approx 15°$).
Increasing the number of signal wires from 90 to 120 produces an improvement of roughly 20%. More wires do not really advance the resolution further.
A segmentation of the central field cathode like the OBELIX experiments used it, would improve the point resolution in xy-plane a little bit (from $300\,\mu m$ to $\approx 250\,\mu m$) and σ_z by some factors. The latter one does not have any influence on p_t but the σ_{xy} improvement increases the transversal momentum resolution by 20%.

Conclusion

The TPC has a much better intrinsical p_t resolution especially for small angles. The SPC on the other hand, due to a much more simple design, has many parameters for improvements, but even with tuning the resolution of the TPC can not be achieved.
To improve the p_t resolution for strongly forward going particles and to increase the detector acceptance, an additional tracking detector is under investigation. It should consist out of three double sided silicon strip detectors in disk shape located inside the inner bore of the TPC perpendicular to the beam axis in downstream direction.

2.6 TPC for the Crystal Barrel experiment

A time projection chamber is well suited as tracking detector for the Crystal Barrel experiment. It has a good position and momentum resolution, as well as a very low material budget.
The complexity of such a detector exceeds by much the required man power and knowlegde a single person can provide. Therefore we joined the GemTPC collaboration in 2007. This collaboration between GSI Detectorlab, Technische Universität München (E12 + E18), Stefan-Meyer-Institut Vienna, and the HISKP is heading for a TPC as central tracker for the $\bar{P}ANDA$ experiment at the FAIR facility.
At the moment there are two options for the central tracker of $\bar{P}ANDA$, one is a straw tube tracker and the second one is a TPC. Both detector options have to show their feasibility and performance via prototypes before the final decision is met.
The prototype of the $\bar{P}ANDA$ TPC is designed such a way, that it serves all the needs of the prototype testing and fits also the constraints of the Crystal Barrel experiment. So all the effort is not only for prototype, but also for a detector, which will be used for a real experiment. On the other hand, during data taking the knowledge of operating, debugging, and analysing is built up and ready before the final TPC for $\bar{P}ANDA$ is available. However, there is no better way to test a detector than in a real experiment, so there is a real synergy.

At this point the question may arise why one needs to have a prototype TPC, since much bigger ones were already build and successfully operated. Well, the $\bar{P}ANDA$ TPC has to address two unique challenges. First of all there will be no trigger signal telling the TPC to start readout, i. e. the detector has to readout all channels continously, look for clusters, and send the observed tracks to the **D**ata **Acq**uistion system (DAQ). Related to this the second challenge is to get rid of the gating mechanism the ordinary TPCs implemented. The gating is needed to suppress the ion back flow into the drift volume during the amplification process of the electron clusters. Otherwise the ions form a space charge in the drift volume, which deforms the drift field and therefore

worsen the resolution of the detector. Thus a GEM amplification stage is implemented, since it has an intrinsic ion suppression and gating is not needed. The first challenge basically strikes the front end electronics. Up to now almost all experiments provide trigger signals, therefore the market for free running, non triggered front end chips is very limited. Also the data handling and online reduction provides a lot of interesting work to be tackled.

To test the various parts of a TPC in good-natured conditions, a small test TPC was build by the Munich group around B. Ketzer. This detector is not only operated with cosmics, but also has to prove its rate capabilities and performance with beam. That is the reason why a tracking test bench, as described in the next section, was setup at the electron accelerator facility ELSA in Bonn.
The analysis of the acquired data of the beam telescope and a first analysis of the TPC data is presented in chapter 4.

Gutta cavat lapidem non vi sed saepe cadendo.
Ovid

3 Testbench

The goal of the tracking test bench is to test the test TPC and further detectors in an electron beam with a precise external track definition. For that purpose 4 tracking detectors are installed, each with a resolution better than the one of the detector under investigation.
Especially the resolution of the test TPC is studied in dependency of the drift field, the amplification voltages, gas mixtures, and further parameters.

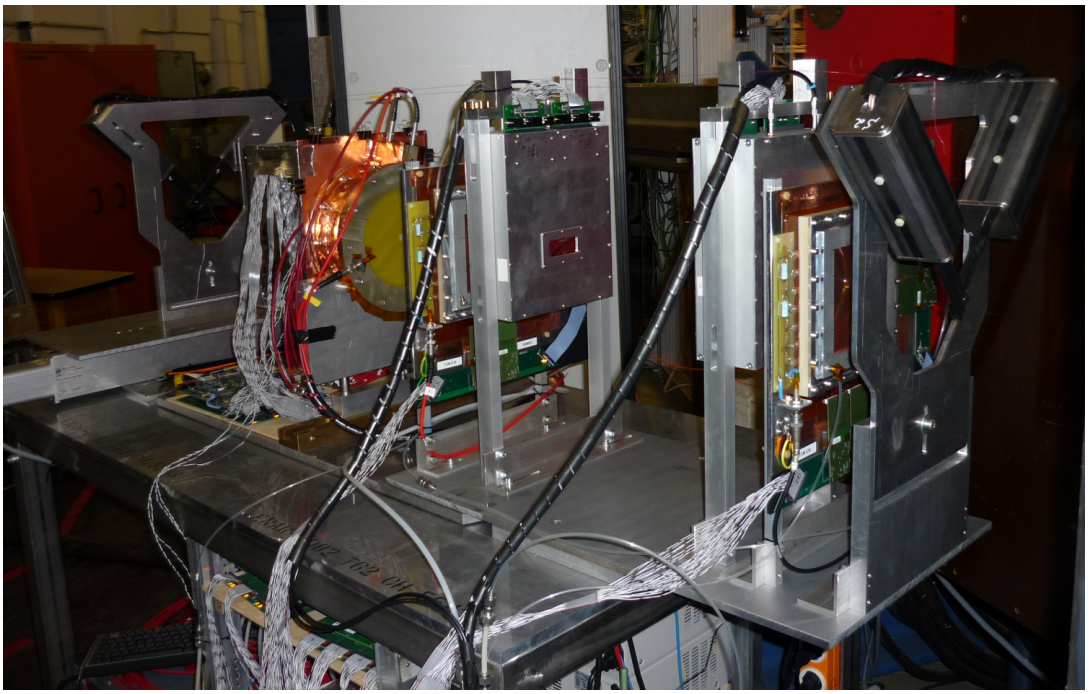

Figure 14: Photo of the tracking test bench. Electrons entering from the right hand side hitting scintillator pair 1, GEM1, Sil1, Sil2, GEM2, test TPC, scintillator pair 2.

Figure 14 shows the tracking test bench installed in the Crystal Barrel experimental area. Electrons are coming out of the energy tagging system from the right hand side and cross the tracking detectors.
The holding structure manufactured out of stainless steel and aluminum is fixed to the ground, but can be removed by a crane. Beside the support structure for the sub detectors, it consists of a 19 inch rack, where the crates and servers are installed, and a gas rack housing 4 gas bottles.

The following right-handed coordinate system is appointed for the test bench:

- $\vec{z}$ orientated along beam axis (from up to downstream).
- $\vec{y}$ points upwards.
- $\vec{x}$ has to go from the right to the left hand side looking downstream.

The first and the last detectors in the row are the trigger scintillators (described in 3.1), which select electrons around the central axis and generate a trigger signal whenever all four scintillators are hit. The scintillator pair at the downstream end (left hand side of figure 14) can be moved along the x-axis remotely to find the optimal trigger position, i. e. main direction of the electrons.
The tracking detectors, forming a so-called beam telescope, are all located infront of the test TPC (compare section 3.4), because the multiple scattering of electrons in the material of the readout flange is significant.
The detectors with the highest precision, the best position resolution, are the silicon strip detectors (see 3.2). They are placed in the middle of the beam telescope to have no additional material in between, which causes scattering. The distance between both is maximized, to have the maximal lever arm for reconstructing the particles' tracks.
Surrounding the semiconductor detectors, 2 planar GEM tracker (details in 3.3) are installed. They provide additional track points, which are necessary for tracking.

3.1 Trigger scintillators

The trigger scintillator detectors of the testbench have two tasks. One is the selection of electrons on certain tracks along the z-axis as well as the generation of timing signals for the particles.
For this purposes organic scintillators with photomultiplier readout are perfectly suited, because they have a good timing resolution below 1 ns and a very low material budget ($< 1\%\ X_0$), which is important to minimize multiple scattering of the electrons.

The single detectors consit out of the following parts:

- scintillating material[32]: It is cutted into bars of 20 mm width 150 mm length and 3 mm thickness and wrapped with aluminized mylar foil for achieving a high reflectivity and black tape, to get it light tight.
- Photomultiplier[33](PMT) which converts the scintillation light into electrical signals. The used PMTs were qualified with a LED pulser and the peak to valley ratio at the single photo electron peak. Scintillator

[32] EJ-260 is a green ($\lambda_{max} = 490$ nm) emitting, 9200 γs / MeV energy deposition.
[33] Photonis XP2972, a fast (2 ns rise time), 10-stage, 29 mm diameter tube with a typical gain of 3×10^6 and a maximum sensitivity at 420 nm.

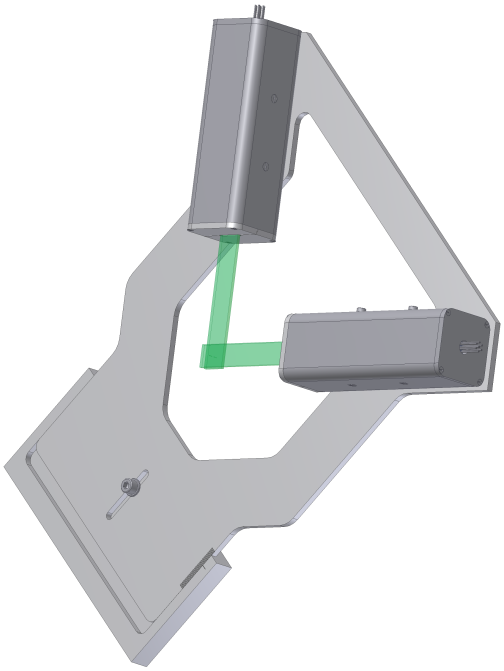

Figure 15: CAD drawing of a pair of scintillators arranged in a V shape to get a rectangular overlapping region. The iron boxes contain the photo multiplier tubes and the holding devices for the scintillators (green bars).

and photomultiplier are connected via optical grease to have an optimal contact. The Fixation is done by a plastic holding device. There is a steel container around the PMT, whose main task is to do a shielding of magnetic and electrical fields. In addition it keeps the PMT, the base, and the scintillator holding device together, so that there is always a good connection between these parts. Beside this the container is light tight, so no light from outside can enter and create some signal on the PMT.

Two detectors are arranged in a V shape (see figure 15) to have a overlapping region, where a coincidence of both detectors identifies a penetrating particle. At the same time the PMTs with their massive shielding are kept out of the beam plane.
The holding structure can be adjusted in height (y-axis) by $\pm$ 20 mm and $\pm$ 35 mm in x direction. In addition the second scintillator pair can be moved remotely in the x direction by 700 mm. This feature was very important during the commissioning, because the exact trajectories of electrons coming out of the tagging system are not known and the necessary scan could be performed without entering the area during beam time, to find the optimal detector positions. Figure 16 shows a horizontal scan, where the σ of the fitted gaussian corresponds to the scintillator width of 20 mm.
The four trigger scintillators form a four fold coincidence to generate a trigger signal, where scintillator 2 is delayed by 8 ns to make sure this detector is always the latest one and therefore causes the timing. The time resolution of

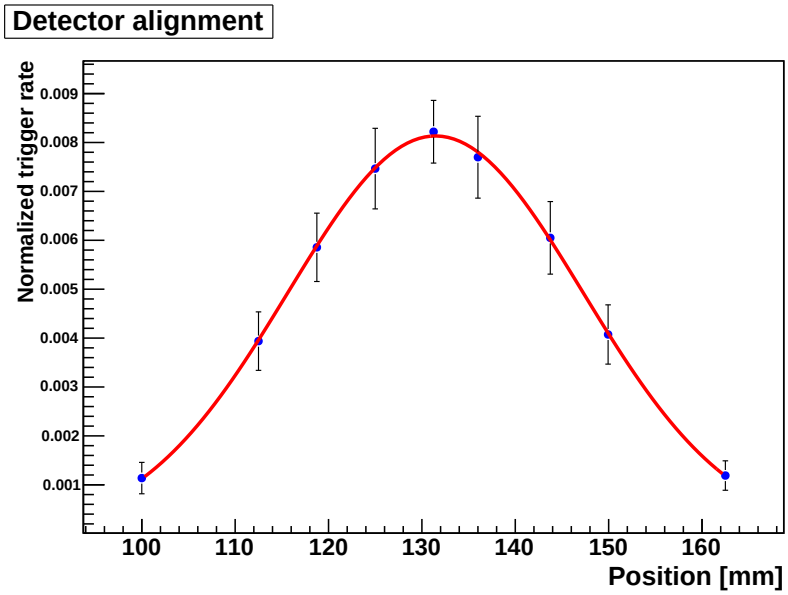

Figure 16: Coincidence rate of all four scintillators in dependency of the x position of the downstream pair normalized to countrate of scintillator 2 (fixed location). Data points can be described by a gaussian function, as plotted in red. Errors from count rate statistics of individual measurements.

the individual detectors is measured by triggering on three detectors and observing the prompt peak of the fourth detector. The achieved time resolution is $\sigma_t = 0.7\,\text{ns}$, which is actually a folding of the timing of the trigger and the investigated detector resolution. Whatever, the goal for the time resolution of 1 ns is succeeded anyway.

3.2 Silicon strip detectors

Semiconductor detectors consist out of a diode, which is reversed biased[34]. Charged particles ionize the material during penetration of the depletion zone and create free charge carriers that way, which form a measureable current through the diode.
To create a position sensitive detector a piece of semiconductor, typically silicon, is structured into individual diodes using common lithography techniques. The structure can be of the order of some millimeters (pads), or in strips with some dozens of micrometers in width and some tens of millimeter length. The finest segmentation is called pixel with typical dimensions of some tens of micrometers in both directions. All these concepts use a common substate for many individual diodes arranged in a periodic grid. Due to the high density, the readout circuits also need to be shrank down. Typical analog front end ASICs contain 64 or 128 channels, which are bonded directly to the sensor chip. These chips amplify and shape the analog signal before it is discretized in time and either directly digitized in amplitude or transmitted to an external

[34]Diode with voltage applied in the non conduction orientation, therefore the depletion (charge carrier free) zone expands.

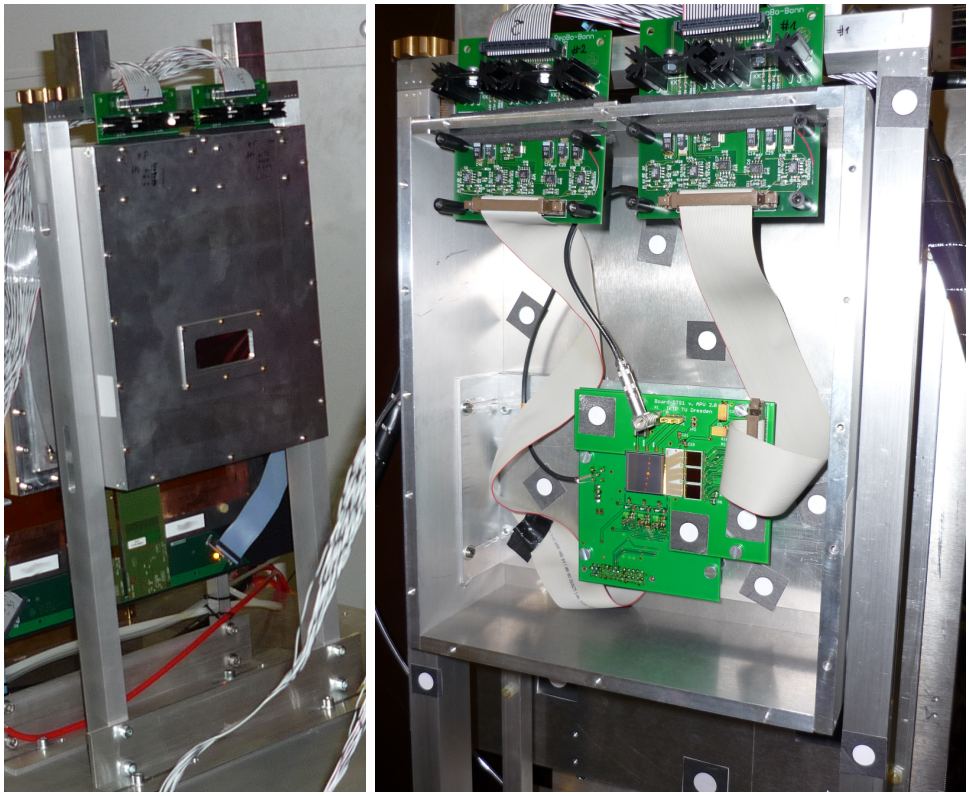

(a) Support and housing structure.

(b) Sensors and repeater cards inside housing with markers for photometry.

Figure 17: Pictures of silicon strip detectors. 17(a) showing the aluminum housing and support structure. Figure 17(b) reveals the inside with sensors (grey square in the middle of the PCBs) with front end chip (3 brown chips on the right hand side of the sensor) and repeater cards (PCBs on top for signal refreshing and low voltage supply).

ADC to do this job.
These and further informations about semiconducting detectors can be found in [45].
The actual sensors installed on the test bench are 300 μm thick silicon detectors, having an active area of 20 x 20 mm^2, a pitch of 50 μm and 384 strips. The sensors are actually double sided, i. e. both sides are segmented in different orientations, but in this setup only one side is bonded to the front end electronics. Hence two sensors close together (3 mm gap) with a stereo angle[35] of 90° are used to obtain a 2 dimensional point for the hit of a charged particle. The detectors are mounted inside an aluminum box to prevent mechanical damage and to provide a shielding for electromagnetic perturbations . This box is mounted on a support structure, so that the detectors can be adjusted in height (y coordinate) ± 25 mm and in their x position ± 35 mm (see fig. 17).

[35] Angle between both detector directions.

3.2.1 Front end electronics

The readout of the sensor is done by APV25 [46] ASICs, which were developed at CERN for the readout of the silicon detectors of the CMS[36] experiment. Each of the 128 channels of that chip has a programable shaper and amplification stage followed by an analog ring buffer, which stores analog samples with a frequency of 20 MHz[37].
When an external trigger is applied, the sampling stops after a configurable latency and a serialized analog data stream (see figure 18) is send to an ADC, which is performing the digitization. Typically three successive samples of all channels are transmitted to the ADC.

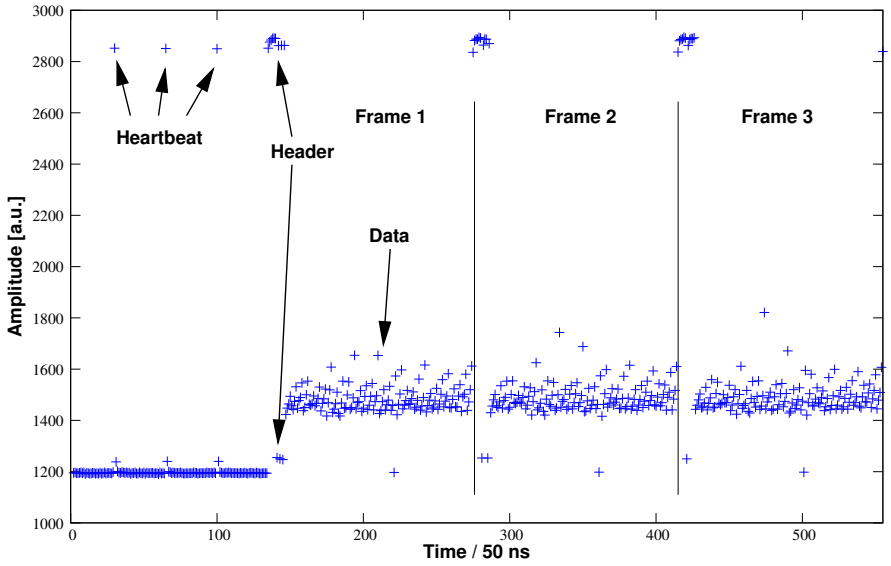

Figure 18: Serial analog data stream produced by an APV chip. One can see the periodic heart beat signals at the beginning, followed by 3 frames which start with headers. The heart beat signals is always present when no data transmission takes place.

In figure 19 the implemented readout chain for the APV25 front end chips is sketched. The strips of the sensor are bonded to the chip, where the signal conditioning and time discretization is done. Whenever a trigger is generated by the trigger module[38], i. e. all four trigger scintillators provide coincidence signals, the **T**rigger **C**ontrol **S**ystem (TCS) broadcasts the event signal with event number and some more details to all attached equipments. The via HGeSiCA[39] attached ADC transmits thereupon the event signal to the APV chip and receives in return the serialized analog data streams from each connected APV. After the digitization the ADC does a pedestal subtraction and

[36] The Common Muon Spectrometer at LHC, see cms.web.cern.ch .
[37] Designed for 40 MHz (LHC bunch clock), but also operate at higher frequencies > 50 MHz.
[38] FPGA based VME module containing the trigger logic and scalers. (See appendix B)
[39] **H**otlink **GE**M and **Si**licon **C**ontrol and **A**cquisition

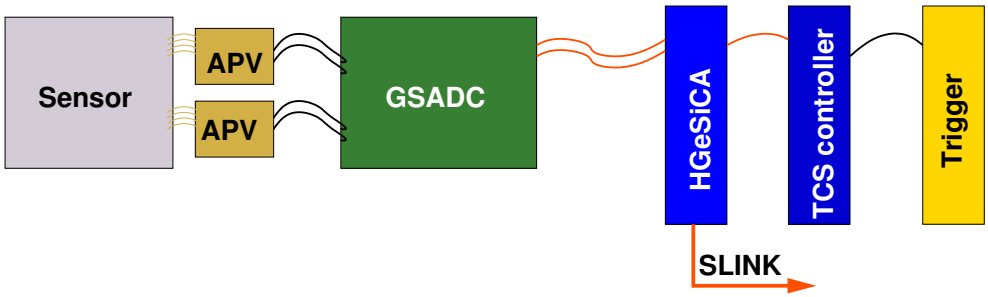

Figure 19: Schematic of the APV25 readout chain with the necessary equipment.

zero suppression[40], to reduce the amount of transmitted data, which is then sent to the data concentrator HGeSiCA. This data is wrapped into a data package with a header and can then be read out by the data acquistion system (DAQ).

3.2.2 Commissioning of silicon strip detectors

The first step of commissioning a detector is to look at the noise and the baseline. Therefore the depletion voltage of 35 V is applied to the sensors. Then data is acquired using a random trigger. The measured ADC values (amplitudes) are filled in individual histograms per chip, where a gaussian function is fitted to the data (see figure 20). From these fits one gets the pedestal (mean of the fit) and the pedestal width (standard deviation σ). The pedestals are used to perform the pedestal subtraction in the ADC online, while the σ is a quality parameter of the detector and its readout, since it represents the noise. In figure 21 the noise spectrum and the pedestals are plotted versus the channel number of one APV chip.

Energy calibration

An energy calibration of each channel is performed to check the readout linearity on the one hand side, but also to obtain an absolute energy calibration. Thus the noise can be determined in terms of **E**quivalent **N**oise **C**harge (ENC)[41].
The APV25 front end chip provides an integrated calibration circuit, which can inject a configurable amount of charge[42] on every input channel.
In figure 22 is plotted the digitized amplitude versus the injected charge. The linear fit delivers the calibration factor between ADC channels and a primary charge at the input of the chip. This figure reveals a nice linearity of the readout up to ICAL = 90, where a saturation begins to take place. However, a minimal ionizing particle (MIP), like high energetic electrons in case of the test bench, deposit in average a charge corresponding to ICAL = 23, so a

[40] If amplitude - pedestal $< 3 \times$ noise, the channel is discarded.
[41] 1 ENC corresponse to the amplitude generated by a single electron in the detector.
[42] Value of ICAL register in steps of 650 electrons.

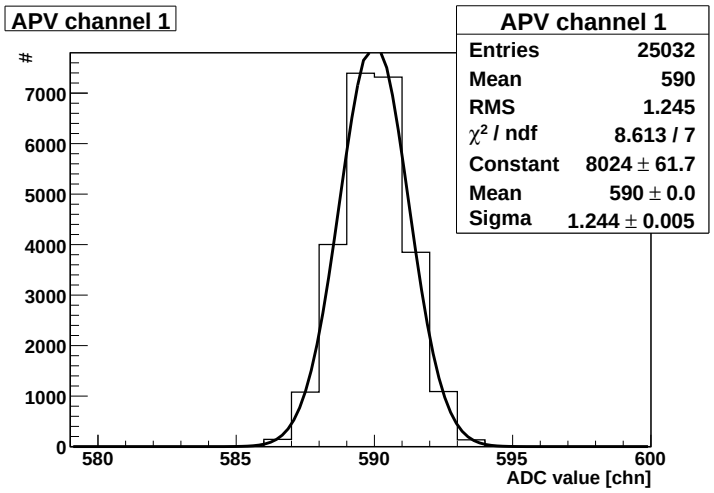

Figure 20: Pedestal peak of a silicon strip with a fitted gaussian.

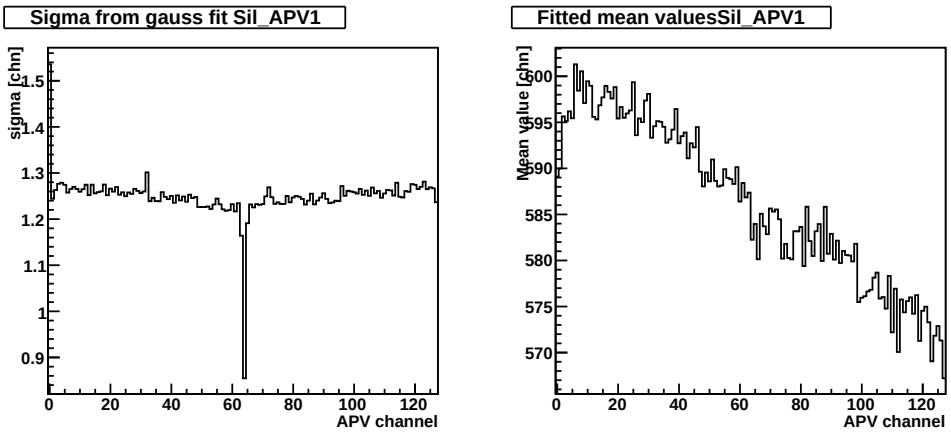

Figure 21: Noise / pedestal sigma vs. APV channel number (left hand side). An unbonded channels shows a lower noise level due to the smaller input capacity. Pedestal mean value vs. APV channel number (right hand side).

simultaneous energy deposition of 4 MIPs on one channel is still fine in terms of linearity.
The plot in figure 23 shows the calibration factors per channel over one APV. There seems to be a general structure, but every APV has an individual one differing from the others.
Two things are contributing to the observed gain fluctuations. First of all each channel has a different gain and leakage due to design and production differences, which are actually the quantities to be calibrated. But there are also the couplings between charge injector and the channel inputs, which also may vary and therefore effect the observed gain. Since both effects can not be studied independently, the pure gain variations of a single channel can not be determined. Thus the variation is below 10%, a gain calibration for the later analysis is expected not to be necessary and therefore not performed.
With this calibration (1 ADC channel = $(320 \pm 30)\ e^-$) one can now determine

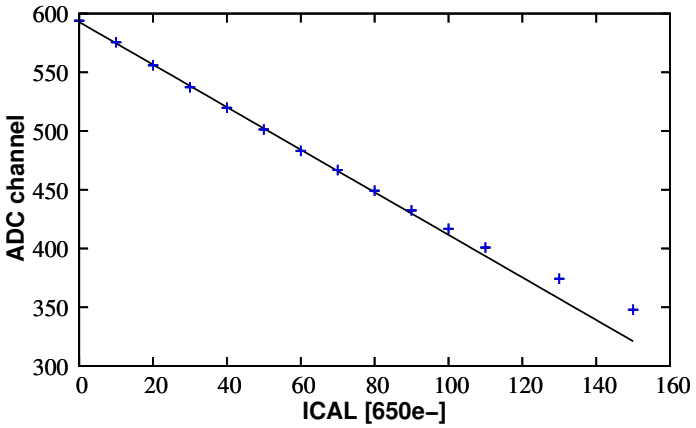

Figure 22: ADC value in dependency of injected charged per individual APV channel. The line is a fit on the data.

the average noise level of all silicon strip detectors to be

$$\langle \sigma_{sil} \rangle = (410 \pm 40)e^{-}.$$

So the APV calibration pulser turned out a good linearity between injected charges and the ADC values, the gain fluctuations between channels are negligible for the test bench purpose, and an absolute energy calibration was performed for all APV channels.

Latency adjustment

The latency of the trigger signal has to be adjusted before data taking, so that the ADC digitizes at the correct time and not before or after the analog pulse takes place. This means the samples' positions relatively to the analog pulse have to be fixed. There are three ways of placing the samples on the analog signal:

- All samples on the leading edge of the analog signal pulse.
- At least one on the leading and one on the trailing edge of the pulse.
- All samples on the trailling edge of the pulse.

Option one enables a simple t_0 extraction (determination of starting time), as discussed in 4.3. The second method provides a good determination of the maximum amplitude of the analog pulse. The third option is not going to be used.
A graphical way to obtain the position of the samples on the pulse is shown in figure 24, the so-called latency or banana plots. Here the ratios x1/x3[43] vs. x2/x3 are plotted for simulated data. The locations of the data points reveal the sampling position. The simulated data is not containing any noise

[43] x1, x2, x3 are the simulated amplitudes of the samples with increasing time. a1, a2, a3 are the corresponding measured amplitudes.

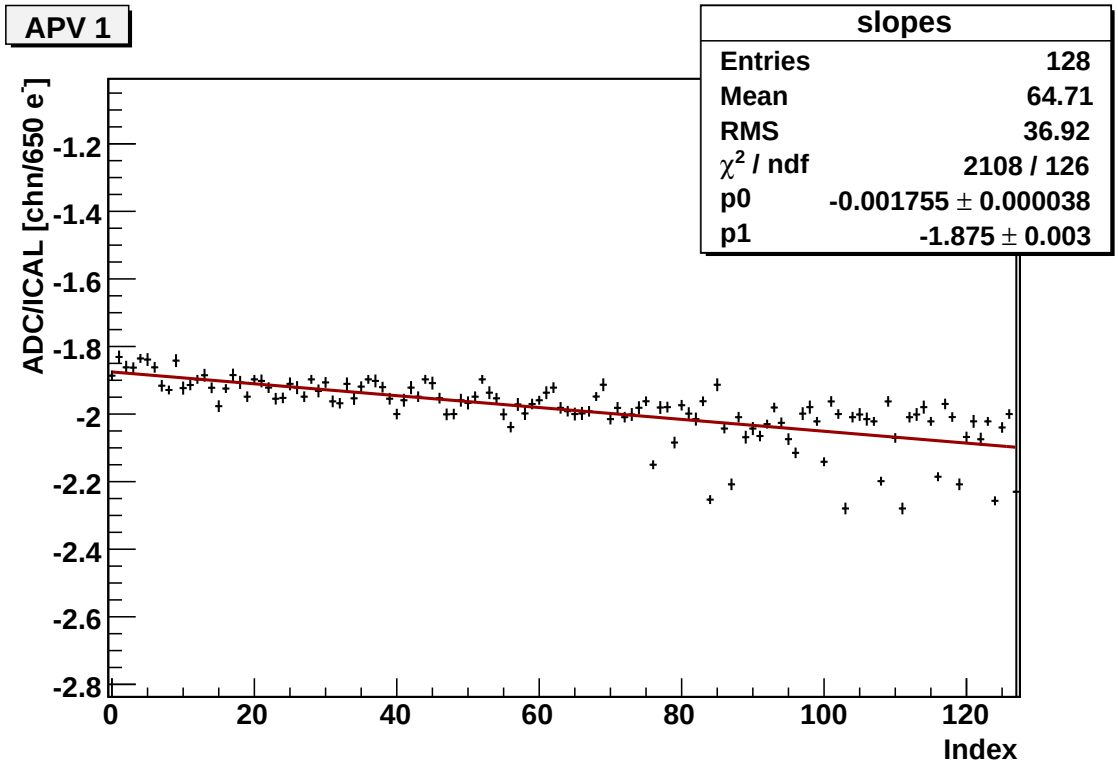

Figure 23: Determined calibration factors of one APV chip. The line represents a linear fit on all data points.

or signal fluctuations, therefore the lines are very sharp, but illustrate the structure nicely.
If one gets only a dot around the origin (Latency 1), the first two samples are infront of the pulse, i. e. too early sampling.
In case of the plot "Latency 4", where both rations are above 1, all the samples are located on the trailling edge, what is not desired, because the trailing edge of the analog signal is much less steep, which results in a greater timing noise. When both ratios are between 0.3 and 1, all samples are located on the leading edge.
One example of real data is shown in figure 25. Comparison of this plot with the simulations in figure 24 reveals that all 3 frames are on the rising edge of the pulse, which enables a good time extraction. This is very useful to correlate the hits in x and y projection for obtaining a 2 dimensional hit point, as shown in section 4.3.

After calibration and time adjustment are done, one starts to look at real hits. The first thing to obtain is a 2 dimensional hit pattern for both silicon detectors. Figure 26 shows such a hit pattern with all possible combinations of x and y strip hits. Silicon 1 is drawn with reversed x axis, so both detectors show the same picture. One edge of the trigger scintillators can be seen for high x numbers.

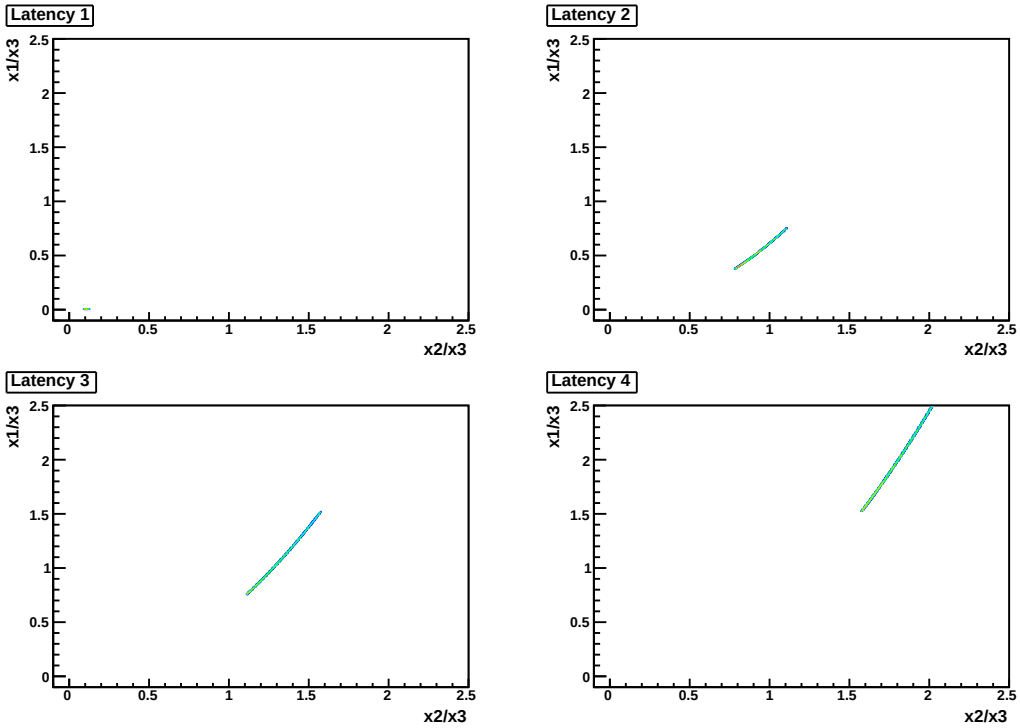

Figure 24: Simulated amplitude ratios for different latencies. Latency 1 = trigger too early, Latency 2 & 3 = sample on leading and trailing edge, Latency 4 = all samples on the trailing edge.

The settings and configuration details for the silicon detectors are listed in appendix C.

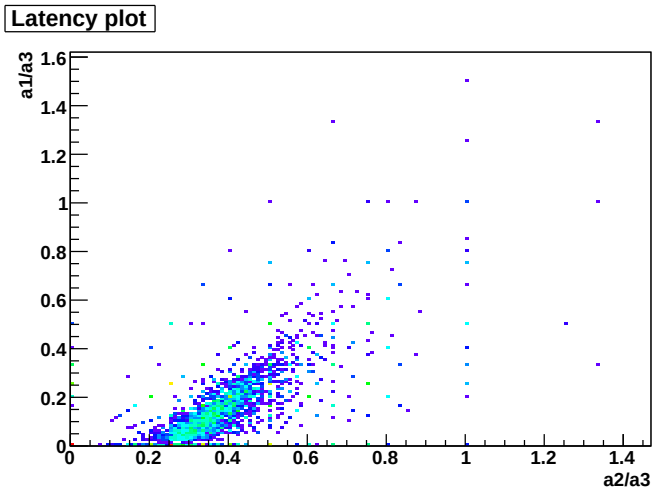

Figure 25: Latency plot of silicon strip detector (APV1). Plotted are the amplitudes of frame 1 to frame 2 normalized to frame3.

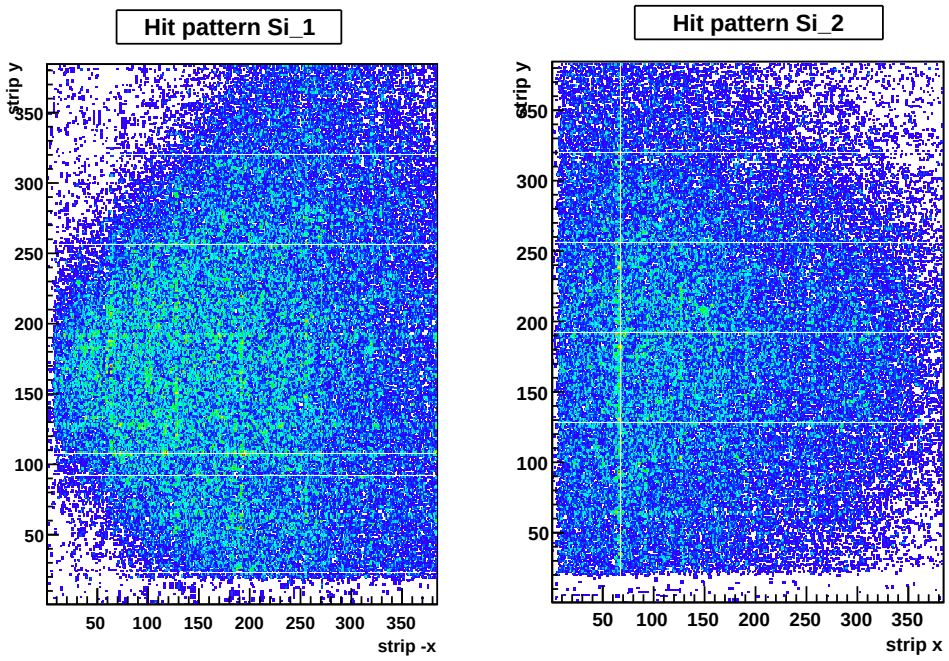

Figure 26: Raw hitpattern of the silicon strip detectors. All possible combination of x and y hits without any cuts are drawn.

3.3 GEM detectors

Planar GEM [47] detectors are the second type of installed tracking detectors (see figure 27).
The traversing charged particles generate ionization clusters in a several mm thick drift gas volume. These clusters are drifting then to a stack of 3 GEM foils, where the gas amplification process is taking place. GEM foils are copperized Kapton foils ($\approx 50\,\mu m$ thick) with holes in a regular grid (spacing $\approx 125\,\mu m$, diameter $\approx 50\,\mu m$). Applying a moderate voltage between both side of a GEM foil generated a strong electric field in the holes, where the gas amplification takes place. The created ions have only a short way to go before being neutralized on the top surface of the foil, so there is a intrinsic ion flow suppression and low space charge accumulation, which makes this technique optimal suited for high rate and occupancy detectors.
After that the amplified clusters induce signals in the readout strips. The readout plane is a PCB with two layer of strips arrange in 90° stereo angle with a strip pitch of $400\,\mu m$. $ArCO_2$ (70:30) is used as drift gas and a drift voltage of 4 kV is applied. The voltages for the GEM stack are provided by a voltage divider from the drift voltage, so only one HV connection is needed.

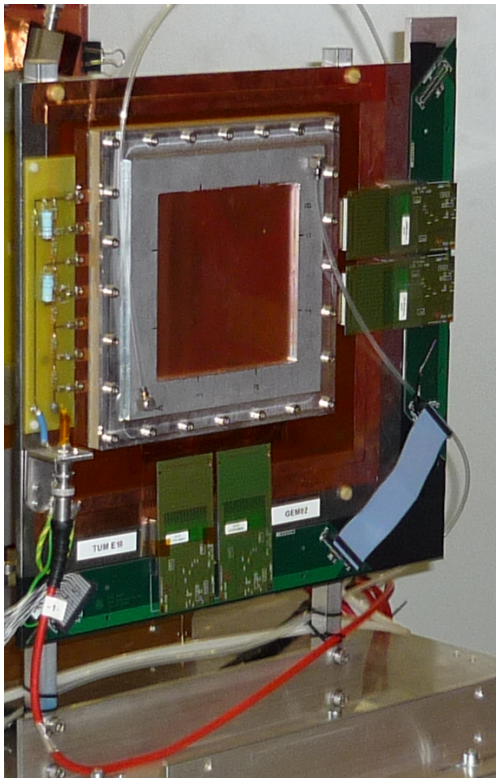

Figure 27: Photo of the second GEM detector. The active area is covered by the copper foil in the middle. The APVs are mounted on the bottom side of four piggy-bag PCBs placed on the bottom and right hand side of the detector.

The APV25 front end chip, as described in 3.2.1, is also used for the readout of the strips of the GEM detectors. The readout scheme and hardware is

the same as for the silicon strip detectors. Only some configurations of the electronics are different. The recent settings are listed in appendix C.
After flushing the detectors with drift gas and applying the drift voltage, the pedestals are recorded. Figure 28 shows the measured pedestals of APV 0. The noise is a factor of 4 higher than for the silicon strip detectors due to the larger capacity of the macroscopic strips compared to the small silicon strips.

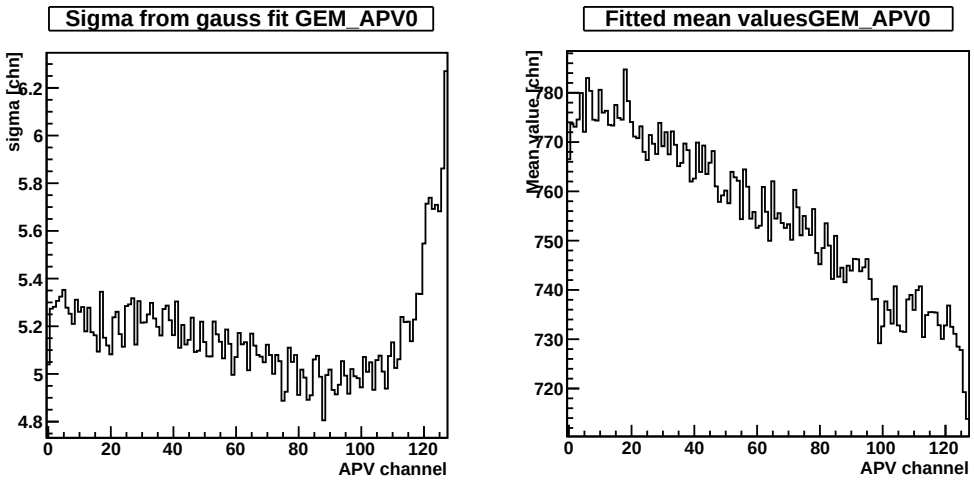

Figure 28: Standard deviation of pedestal fit (noise) vs. APV channel number (left hand side). Pedestal mean value vs. APV channel number (right hand side).

After the calibration of the APV channels one can determine the average noise of the GEMs to

$$\langle \sigma_{GEM} \rangle = (1870 \pm 150) e^{-}.$$

The next step is the adjustment of the latency similar to the silicon detctors. A latency of 17 (GEM1) and 18 (GEM2) turned out to be optimal for the setup. The raw hit pattern for both GEM detectors are shown in figure 29.

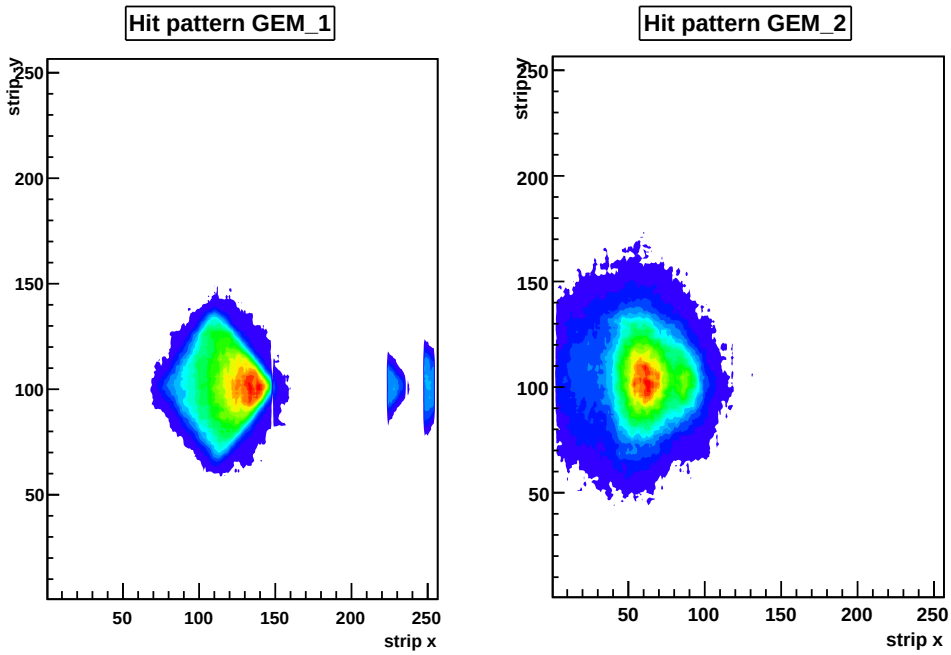

Figure 29: Raw hit pattern of the GEM detectors. The triggered beam spot can be observed clearly. The y axis are plotted in reverse order. On the right hand side of GEM1 appear ghost hits originating from noise channels in the x projection.

3.4 Test TPC

Aim of the tracking test bench is to provide a support structure for a tracking detector and an electron beam, which is externally defined by the beam telescope (silicon strip and GEM detectors). In the first term a small test TPC is installed on the test bench, to study individual sub systems like the amplification stage or the readout electronics. In parallel the monitoring and the analysis software is developed and directly applied to the taken data.

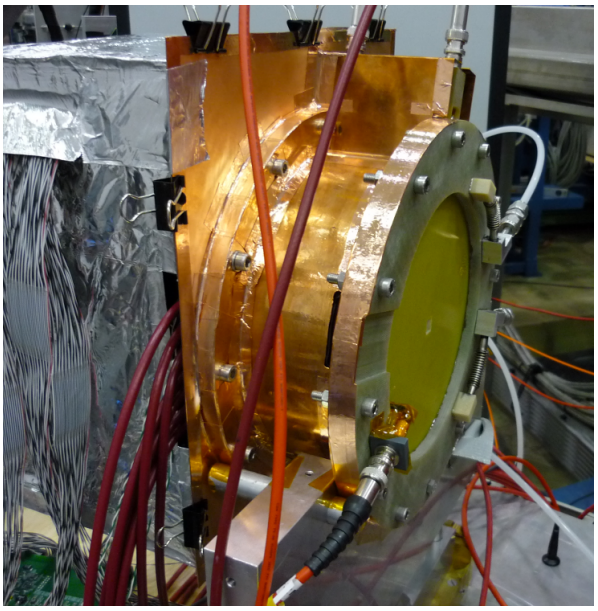

Figure 30: Test TPC with front end electronics covered by aluminum box (left hand side). Electrons emerge from right hand side.

The installed test TPC (figure 30) was constructed and built by the Technische Universität München E18 group around B. Ketzer. They provide the detector as well as the readout electronics. The system has the following specifications:

- Active area: 100 x 100 mm^2
- 1000 hexagonal readout pads (r_i = 1.5 mm and 1.25 mm)
- Drift length: 70 mm
- Drift voltage: 250 V/cm
- Triple GEM stack for amplification
- Drift gas: ArCO_2 (70:30)

For the readout the AFTER[49] chip[44] is connected to the pads acting as a sampling analog ring buffer and when a trigger signal appears the serialized analog data is transmitted to the same ADC chain as for the APV readout

[44] Analog sampling front end chip developed for the T2K TPC.

(see figure 19), but with a different firmware handling the data and another data output format (see figure 31).

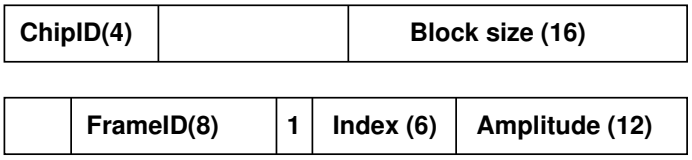

Figure 31: Data Format of the AFTER front end chip, which is packed into a SLINK and ADC frame like the APV frames (see figure 35).

This front end chip offers 76 channels with adjustable shaping parameters. The sampling frequency is externally provided up to 40 MHz, which fixes the maximal latency together with the buffer depth of 512 samples per channel. Figure 32 shows the noise[45] of one AFTER chip. Some channels show a much lower noise level than the rest. These are unbonded channels, therefore the input capacity is lower and the noise reduced. However, the mean noise of 2 ADC channels is better than expected from laboratory tests [50], especially for the long L-shaped extention cards, which are used to get the chips out of the beam plane to the cost of a higher input capacity, which results in additional noise [45].

After acquiring the pedestals, the whole TPC can be readout in the sparse mode, i. e. pedestal subtraction and zero suppression. Reading the complete test TPC in that mode enables to generate a hit pattern of the pad plane, which is shown in figure 33. Beyond an almost isotropic background from uncorrelated tracks an area of higher occupancy can be obtained. Compaired to the detectors of the beam telescope the triggered beam spot is less sharp, due to the much greater distance to the front scintillator pair. Since there is a lot of scattering in the massive readout flange of the test TPC, the second scintillator pair does not constrain the primary electron trajectory that much, to clear up the hit pattern.

Due to some errors in the provided mapping file, some holes in the hit pattern occur and the axis are inverted.

[45] σ of a gaussian fit of the pedestal peak.

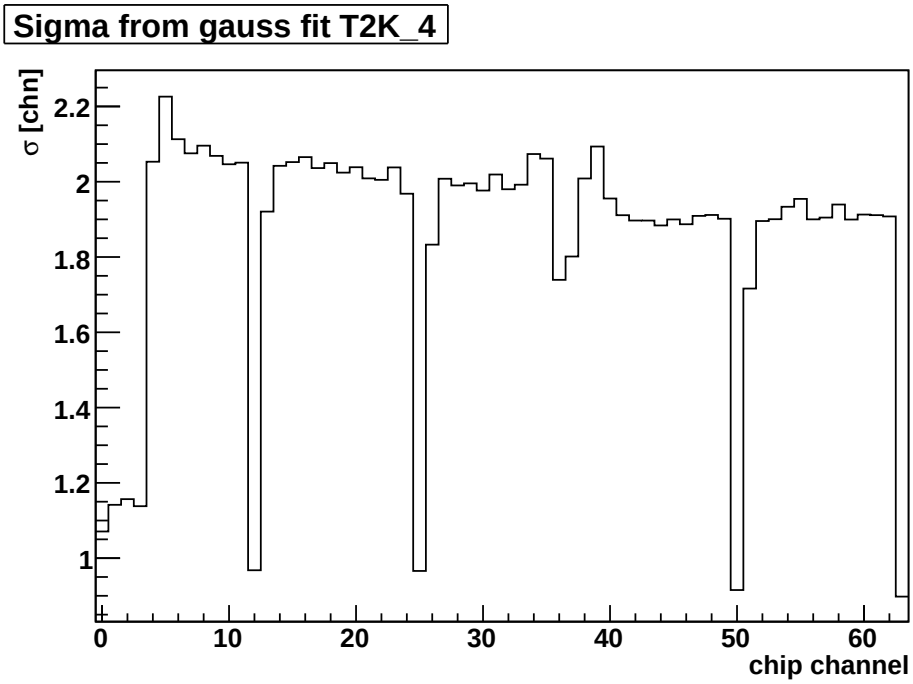

Figure 32: Width of a gaussian fit of the pedestal peak, which represents the noise level of an AFTER chip. Unconnected channels do have a lower noise level as connected ones.

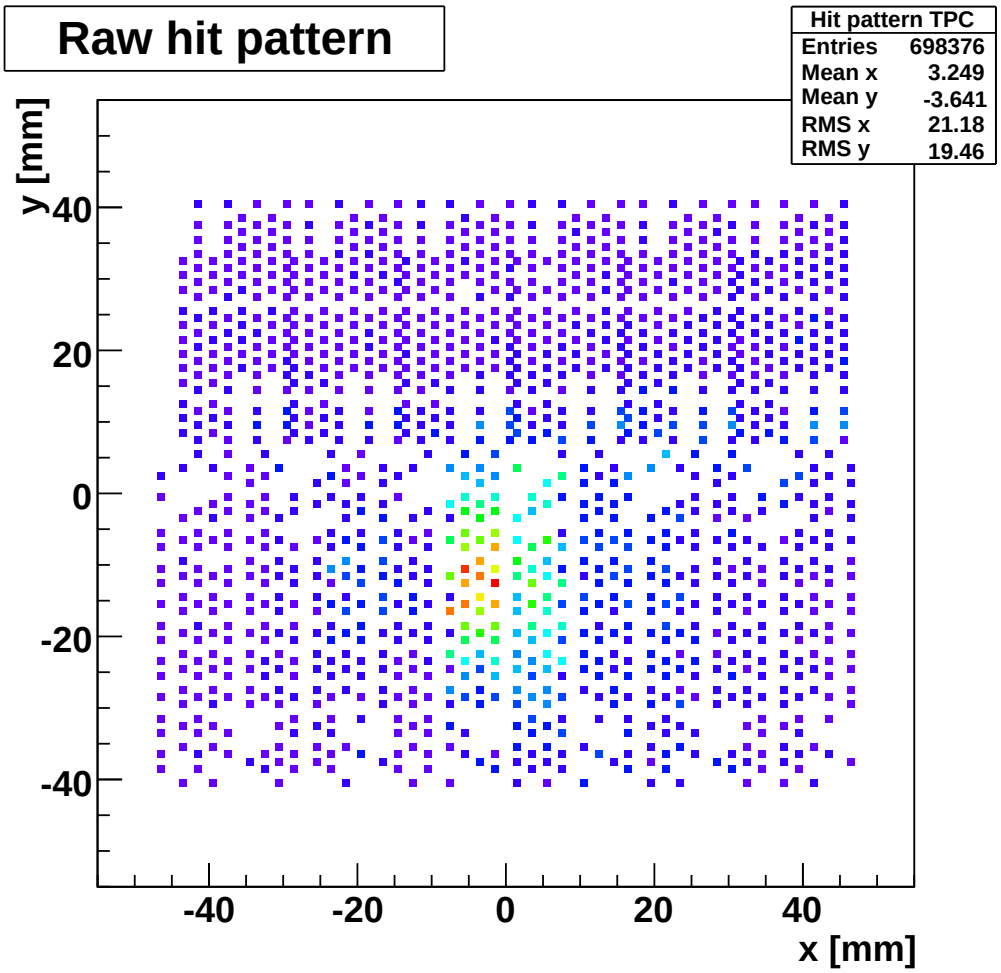

Figure 33: Raw hit pattern of 300k events on the TPC pad plane (run 1191 and frame 16). The pad plane has two different pitches in the upper and lower half. The axis have to be inverted to match with the common coordinate system. Some pads are missing in the plot due to mapping errors.

3.5 Data acquisition system

The **D**ata **Acq**uisition system (DAQ) collects the data from the sub detectors and stores it into a file. The answers to the following three questions will explain what the DAQ is actually doing.

- What and how is going to be read out?
- When is the readout done?
- How is the data stored?

The answer to the first question is given in the order of detectors listed in this chapter.
The signals of the four trigger scintillators are split into 2 branches, where the first one is given to a leading edge discriminator (LED) to generate a digital signal. This signal is used to derive the trigger signal and after some cable delay it represents the stop pulse for the TDC[46]. The second branch of the analog signal is delayed via cables and then given to a QDC to measure the pulse height. The time and amplitude information of the trigger scintillators is not important for the tracking itself, but are very helpful debug information. In figure 34 the readout is sketched with cable lengths and module types. The TDC and the QDC are both LeCroy CAMAC modules, which are read out via a VME CAMAC controller (CBD8210).

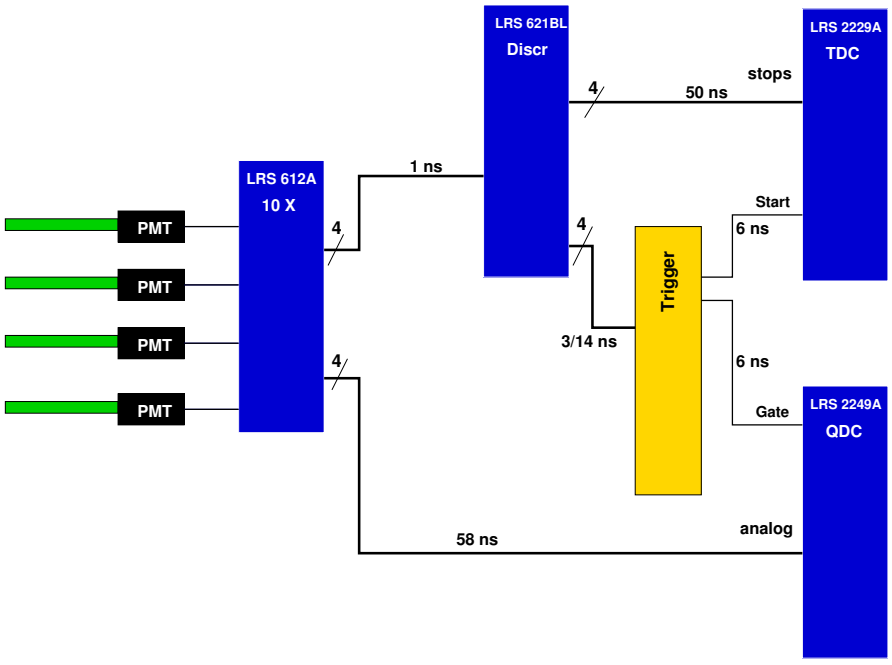

Figure 34: Schematic of scintillator readout with detectors, modules, and cables with their multiplicity and length in ns.

The readout of the silicon strip detectors and the GEM detectors is actually the same, since both detectors use APV25 chips. In figure 19 the readout of

[46]Time to digital converter measured the time between a start and a stop signal.

the sensors was already sketched. Whenever the TCS controller receives an event signal from the trigger module and the DAQ is ready, an event signal with a header is distributed to the HGeSiCA modules via optical fibers using the TTCex Laser module with 20 dBm attenuators. Hereupon the data concentrator (HGeSiCA) transmits a trigger signal to the optical attached ADCs, which finally generate the trigger signal for the APV chips. As explained above, the ADC digitizes the serial analog data stream and sends the requested data to the data concentrator, which generates container for the data including a header word. Since up to eight ADCs can be connected to one HGeSiCA, the ADC packets are again wrapped into a SLINK frame (see figure 35) [48].
The test TPC uses the same readout system as the APVs, but with a different firmware of the ADC creating also another output data format.

There are two different ways to get the data out of the HGeSiCA module. The simple one is to read sequentially a 4 byte VME register of the module, but the depth of the implemented FIFO[47] is a limiting factor, i. e. for high event rates and many attached channels the queue can overflow and corrupt the data.
The second option for readout is the SLINK[48] interface. This is a mono directional optical connection between the data concentrator and a PCI card. The data is pushed to the memory of the PCI card (spill buffer card) without any flowcontrol. The installed memory is sufficiently large and the interrupt based DMA transfer from this memory to the readout application is that fast, so that no buffer overflow occur. The linux kernel driver for these spill buffer cards was developed by L. Schmitt for the COMPASS experiment, but it needed some modification for our operating system (Debian 4.0).

There are now two different DAQ systems to acquire the data. First of all I have developed a stand alone DAQ, to have control and access to all informations. All the testing and debugging of the silicon strip and GEM detectors was performed with this VME or SLINK based DAQ.
In addition my colleagues from Techinsche Universität München (E18), which are deeply involved in the COMPASS experiment and have designed many of the readout modules, run DATE, the COMPASS DAQ, because it should run out of the box and their analysis is working directly on that data format.
In my DAQs every module in usage is represented by a C++ class containing all functionality (encapsulation). The main program just creates instances of these classes to do all configurations and the data readout. In case of this VME DAQ, a single CPU locking DAQ scheme is used, which is explained in the following listing:

1. Prepare electronics
2. Open life time gate
3. When trigger occurs and life time gate open: close life time gate

[47] First in first out memory element.
[48] For details see: http://hsi.web.cern.ch/HSI/s-link/

SLINK header

err	event type (5)	source id (10)	event site exc. header (16)
stat	spill number (11)	event number (20)	
format (8)	#error words (8)	tcs error (8)	status (8)

ADC header

format old ADC (8)	ADC ID (8)	ADC event size (16)
1 format new ADC (7)	time tag (24)	

APV header

chip id (4)				local event no. (12)		APV block size (16)
1	gs	as	00	APV header frame 3 (9)	APV header frame 2 (9)	APV header frame 1 (9)

Sparsified data format

channel no. (7)	ADC value frame 3 (9)	ADC value frame 2 (8)	ADC value frame 1 (8)

Latch–all data format

1	sf	ADC value frame 3 (10)	ADC value frame 2 (10)	ADC value frame 1 (10)

Last word APV frame

1	cr	baseline frame 3 (10)	baseline frame 2 (10)	baseline frame 1 (10)

Figure 35: Data structure of APV data. Numbers in brackets represent the number of bits. The APV block consits out of an APV header and the data block (up to 128 words). 16 APV blocks are encapsulated in an ADC packet. A SLINK frame contains up to 8 ADC packets.

4. Collect the data and write event packet to file

5. Reset the electronics and goto 2 while not aborted

The readout of the HGeSiCA is also accomplished via the VME interface. Nevertheless a SLINK DAQ was developed as well, where the readout of HGeSiCA is done via the SLINK interface. This data and further information are merged according to unique event and spill numbers provided by the TCS.
The data is stored in a binary format in the following structure:

Name	Size
Packet size in Bytes	32 bit
Scintillator ADC[4]	4 x 16 bit
Scintillator TDC[4]	4 x 16 bit
Scaler [16]	16 x 32 bit
HGeSiCA 1 data	variable
HGeSiCA 2 data	variable
HGeSiCA 3 data	variable

After getting DATE operational, this DAQ is used, since it is more userfriendly once it is configured correctly. It also takes care of the event building of the different data sources and provides the data structure needed for the COMPASS monitoring software used by the Munich colleagues.
To switch in the analysis between the data formats of DATE and my DAQs hardly any effort is needed due to the flexible analysis framework.

3.6 Slow control and gas system

Two individual gas systems were set up. One for the GEM detectors and a second one for the TPC. Both are very similar, namely having two source gas bottles, where one is containing the drift gas for measurements and the other nitrogen (N_2) for flushing the detectors while not in use. There is a switch to select between these gases.
Cleaned stainless steel pipes are used to guide the gases through a remote controlled flowmeter to the detectors. The gas outlets are implemented with some meters of plastic tube, to minimize the back flow of oxygen or water in the detector. A bubbler could also be used to separate the active volume from the outer world, but especially for the TPC the pressure variations due to not continuously bubbling would change the drift velocity and therefore decrease the resolution.
The standart flow of N_2 and the drift gases is is 4.5 l/h.

The whole test bench with all it's peripherals is monitored and controlled by the slow control. List of attached equipment:

- High voltages (Scintillators, GEMs, TPC)
- Low voltages (front end electronics)
- Flowmeters (TPC and GEM circuit)
- Gas quality for TPC (oxygen and water)
- Temperatures

The graphical user interface is implemented via a web site[49], which enables the monitoring and user specific manipulation of all parameters. The core of this slow control is a PostgreSQL data base, where front end demon can connect to in order to request or transmit data.
The major work on the gas system and the slow control is done by D. Kaiser as a part of his doctoral thesis.

[49] http://tbserver.cb.uni-bonn.de/slowcontrol

Perfer et obdura.
Ovid

4 Test bench data

The decoding and analysis of the data acquired with the test bench is done using the Crystal Barrel *explora*[50] framework. This software is based on *root*[51] and follows an object oriented C++ programing style. The core system is extended by plugins, which can be exchanged flexible, since inheritance and interfaces are strictly used.
XML[52] files are used to define the hierarchical plugin calls and to set parameters. So there are two levels of programing. On the C++ level the implementation of algorithms and data handling is performed, while the XML level creates instances of plugins, defines the data organization, and fixes the program flow.

As the explora framework was developed for the Crystal Barrel experiment having only calorimeters and scintillators, there were no methods or data structures foreseen for tracking detectors. Therefore some basic plugins needed to be extended and the whole chain from decoding to analysis had to be developed.
In the following part the processing chain with some results is presented. Thereby the focus was put on getting the full chain running, rather than having the ultimative and final software. For sure the algorithms must not be too bad to obtain trustable results.
Due to the plugin concept every single step can be re-implemented in a different way without touching anything of the rest. Thus the effect of single changes in the chain can be studied on all results. The speed of the plugins can also be tested that way by using the plugin profile features and the bottle necks can be taken care of.
Colleagues from Munich are doing a parallel analysis using the COMPASS analysis software. Errors or great uncertainties in one analysis can be revealed by comparison of results of both different packages.

In the following sections (4.1 - 4.5) only the detectors of the beam telescope are beeing discussed. The analysis of the test TPC is presented in section 4.6. The goal of the analysis of the beam telescope is the reconstruction of particles' tracks and the determination of the resolution of the single detectors. Therefore the following steps need to be done: After decoding the binary data and mapping it to detector structures, a clustering algorithm is implemented to find the center of gravity of the detector hits per projection (1D hits). Afterwards the hits of both projections of a detector are matched to obtain 2D detector hits. For fitting a track to all hits, it is necessary to have space points from each detector, which are achieved by the determination of the 3D detector offsets. The detectors' resolutions are then given by the deviation of

[50] **Ex**tended **pl**ugable **o**bjectoriented **r**oot **a**nalysis
[51] See root.cern.ch
[52] Extensible Markup Language

the fitted track and measured hit point in the detector, the so-called residual distribution.

4.1 Raw data decoding

The first step of data processing is the translation of the DAQ data into data objects, which can be used for the further analysis. Herefore it is necessary to recall the data structure as shown in 3.5. The decoding happens reversely to the data packing in the readout, i. e. take outermost frame, interpret the header, extract the payload and so forth until one reaches the real data.

The outermost frame of the silicon strip detectors, the GEM detectors, and the TPC data are SLINK frames. To decode them an instance of the *CBTSlinkDecoder* plugin is called with a pointer on the raw data from explora basic methods. The decoding method of this class then triggers an object of the type *CBTGsadcDecoder* with the pointer on the payload of its structure. Finally the *CBTApvDecoder* does the decoding of the data and the creation of *CBTDataObj* instances.
The listed classes are C++ classes, which are compiled to shared object libraries. The data processing and the handling of the different objects and instances are done in an XML configuration file. The following part from a XML file represents the decoding as explained above:

```
<CBTSlinkDataStructureCollection debug="1" prefix="slink." >
  <CBTDataContainer ref="tpc_data"/>
    <CBTSlinkDecoder debug="0">
      <CBTGsadcDecoder debug="0" >
        <CBTApvDecoder debug="0" prefix="sil1." adcid="1"
 notconnected="true">
        </CBTApvDecoder>
        <CBTApvDecoder debug="0" prefix="sil1." adcid="1"
threshold="20">
        </CBTApvDecoder>
        ...
        <CBTApvDecoder debug="0" prefix="sil1." adcid="1"
threshold="20">
        </CBTApvDecoder>
      </CBTGsadcDecoder>
      <CBTGsadcDecoder debug="0" >
        <CBTApvDecoder debug="0" prefix="gem1." adcid="2"
threshold="100">
        </CBTApvDecoder>
        <CBTApvDecoder debug="0" prefix="gem1." adcid="2"
threshold="100">
        </CBTApvDecoder>
        ...
        <CBTApvDecoder debug="0" prefix="gem1." adcid="2"
threshold="100">
        </CBTApvDecoder>
```

```
      </CBTGsadcDecoder>
    </CBTSlinkDecoder>
</CBTSlinkDataStructureCollection>
```

Let's have a closer look on the *CBTApvDecoder* class, because this one is doing the actual data decoding and the creation of the data objects.
At first the decoder has to detect whether latch-all[53] or sparsified[54] data is present by looking at the ADC header, because the data structure in both cases is not the same (see figure 35).
After this *CBTDataObj*s with the listed properties are generated:

Property	Explanation
Index	APV channel number
GroupID	global APV ID
FrameID	frame number (0..2)
Value	ADC value
Name	global name incl. frame, chipID, channel, prefix

The sequence of the serialized analog stream from the APV is not in the same ordering as the input channels (strips). The reordering of the output index to input channel number n is done by the APV decoder using the formula

$$n = 32 * (Index \bmod 4) + 8 * (Index/4) - 31 * (Index/16).$$

The concept of explora is to map the single informations (CBTDataObj) into structures, which represent the real detectors with its subdetectors and so on. In case of the silicon strip and the GEM detectors all channels of sensors are arranged in one object (*CBTExtendedDataObject*), which contains beside the amplitudes of the single channels also further information like the pitch and orientation.

4.2 Clustering

The signal of a traversing particle does not stay within a single channel, but spreads over a few ones. This provides a better resolution than the strip pitch d by looking for clusters[55] and determining their *center of gravity*. The *CBTClusterFactory* class of explora is providing this cluster algorithm and also determines the center of gravity and the cluster energy in one dimension.
The results of the clustering algorithm for two detectors (GEM1_x and Sil1_x) are shown in figure 36. The silicon strip detector delivers most likely no or only one cluster per event. In 1% of the events two clusters appear and 3 clusters occur only on the sub per mill level.
The GEM detector on the other hand shows a significant higher cluster multiplicity, which can be explained by the much greater active area - so multiple hits are more likely - and the higher noise also showing up in the noise peak in the cluster energy histogram.

[53] Raw ADC data.
[54] Pedestal subtracted ADC value with zero suppression.
[55] Connected area of activated channels. Single channel gaps are still included.

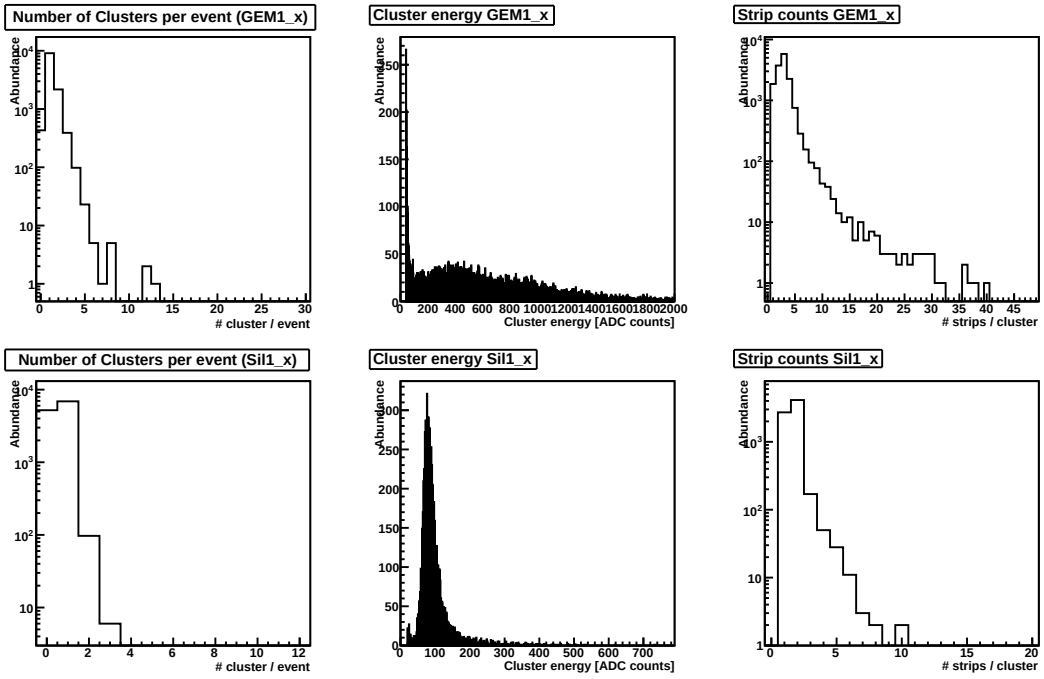

Figure 36: Output of the clustering algorith for GEM1_x and Sil1_x. The distributions of number of clusters per event, cluster energy, and number of strips contributing to the cluster are shown.

The cluster energy distribution of the silicon strip detector provides a clear signal peak around 100 ADC channels and the beginning of the noise peak can be seen on the low end of the spectrum.
The strip multiplicity per cluster is higher for the GEMs than for the silicon detectors, because the charge cloud is broadened through the amplification in the GEM detectors.

4.3 Generation of 2D hits

The next step is to generate 2D hits out of 1D clusters in x and y projection. The simplest approach is to take all combinations of x and y hits within an event. As soon as there is more than one cluster per projection, artificial hits are produced, which show up as background in the hitpattern.
When the two projections of a detector share the same active volume, like the GEM detectors do, one can use the cluster amplitudes to correlate the x and y clusters, because the induced signals are of the same strength in both projections. The plot in figure 37 shows the correlation of the cluster amplitudes of both projections. Hits with too big differences in the x and y amplitudes are discarded. This technique reduces the number of randomly correlate hits, but also real hits may be discarded. Figure 38 shows the reduction of generated 2D hits (η = generated hits / all combinations) in dependency of the allowed matching interval[56].

[56] If |x cluster energy - y cluster energy| < delta cut, then a 2D hit is generated.

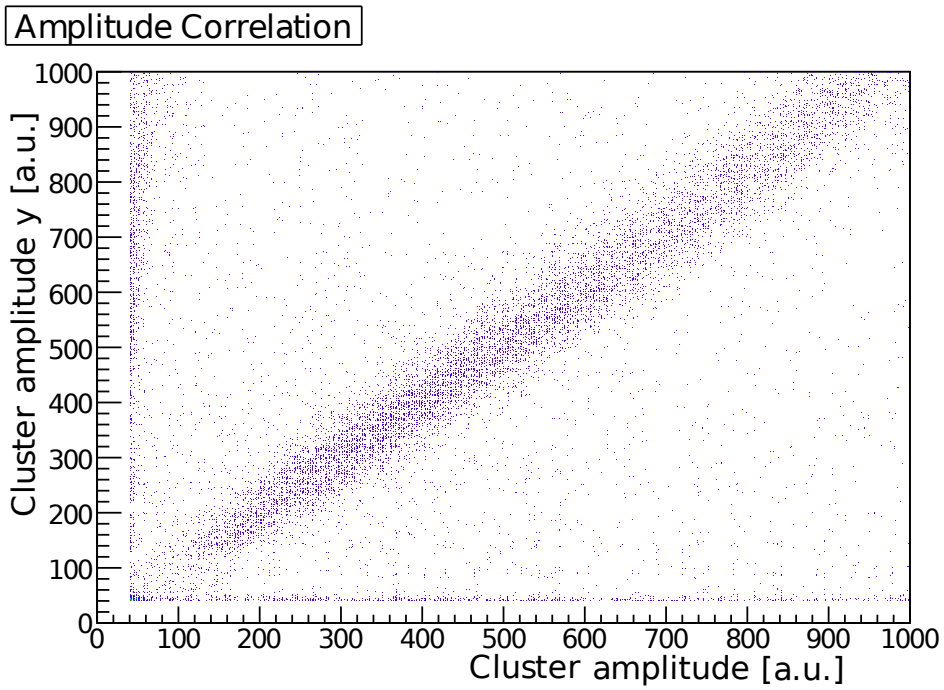

Figure 37: Amplitude correlation for both projections of GEM1 detector.

A third way to obtain the 2D hits from the 1D clusters is to use the time information. Real hits have simultaneous clusters in x and y. This method is also applicable for the silicon strip detectors with two individual sensors for the x and y coordinate, because the signal generation is still in coincidence. Since the three samples of the analog signales are located on the leading edges of the pulses, the timing can be extracted in an approximation by fitting a straight line to the three data points. The line is characterized by the slope parameter m, which is defined by $m = \frac{\Delta y}{\Delta x}$. Two samples would be sufficient for a perfect line fit, but since the pulse does not have a linear rise and the presence of signal fluctuations, three samples are helpful. The averaged slope parameter is calculated with the three samples a_1, a_2, and a_3 by

$$\langle m \rangle = \frac{1}{3}\left((a_2 - a_1) + (a_3 - a_2) + \frac{1}{2}(a_3 - a_1)\right).$$

The crossing of the fitted line with the time axis, called t_0, corresponds to an amplitude compensated starting time. Taking a_2 and the calculated m, one can determine c from equation $y = mx + c$. Now the crossing point is given by $x_0 = -\frac{c}{m} \equiv t_0$. It turns out, however, that c (y axis offset) is already a good cut parameter (see figure 39 for time correlations). This also increases the decoding speed, since t_0 resp. c are calculated in the decoder class for every strip. Therefore the difference in of c_1 and c_2 is instrumented as cut criteria. Hits are matched if for the central strips of both clusters $|c_1 - c_2| < \Delta_t$ is true. The reduction of generated hits versus the cut parameter is plotted similar to the amplitude matching for the time matching in figure 40. Another way to

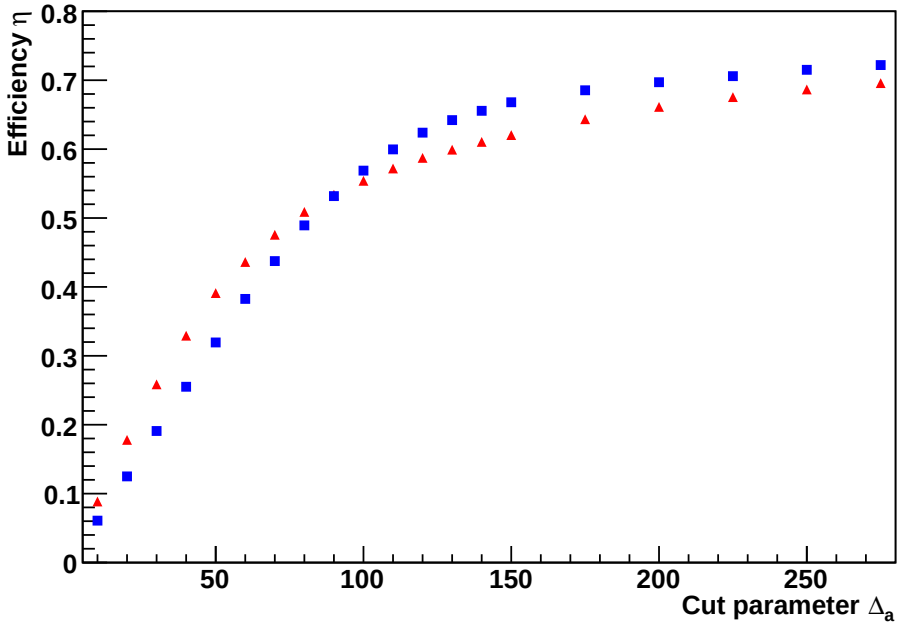

Figure 38: Reduction of reconstructed hits in dependency of the cut parameter Δ_a - the maximal accepted difference between x and y total cluster energy. η = # reconstructed hits / # combinatorial hits. (Red triangles = GEM1, blue squares = GEM2).

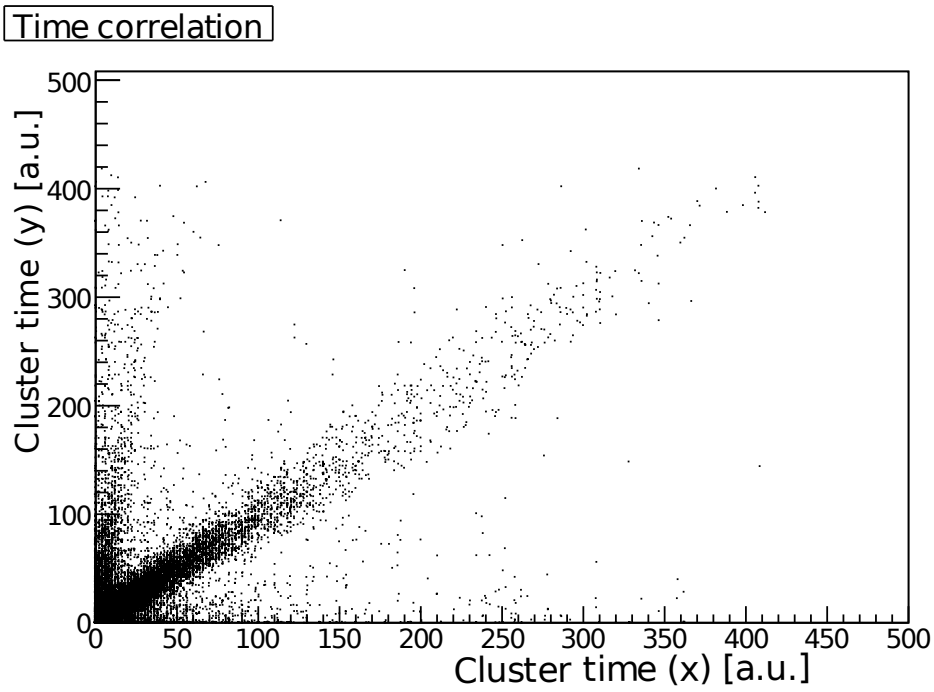

Figure 39: Correlation of the extracted timing parameter for x and y projection of GEM1 detector.

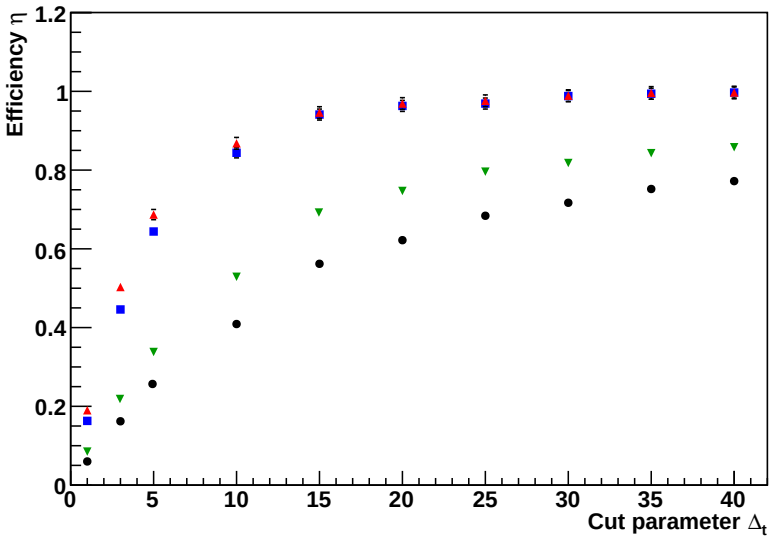

Figure 40: Reduction of reconstructed hits depending on the time cut parameter Δ_t - the maximal accepted difference between the determined c of x and y clusters. η = # reconstructed hits / # combinatorial hits. (Blue squares = Sil1, red triangles = Sil2, green triangles = GEM1, black circles = GEM2).

observe the effect of constraining the matching of the two projections is the mean number of reconstructed hits per event $\langle n \rangle$. In a low rate run, some Hz trigger rate, the detector should see in most cases only a single particle track, so $\langle n \rangle$ should be almost 1. Table 9 shows this mean number of hits for various cuts.

Condition	Sil1	Sil2	GEM1	GEM2
combinatorial	1.057 ± .006	1.037 ± .004	1.68 ± .018	1.6 ± .02
$\Delta_t \leq 40$	1.056 ± .006	1.037 ± .004	1.46 ± .014	1.31 ± .01
$\Delta_t \leq 15$	1.056 ± .006	1.033 ± .004	1.304 ± .01	1.192 ± .009
$\Delta_t \leq 5$	1.042 ± .006	1.024 ± .003	1.187 ± .009	1.108 ± .007
$\Delta_t \leq 1$	1.016 ± .005	1.009 ± .003	1.11 ± 0.01	1.06 ± .01
$\Delta_a \leq 250$			1.199 ± .007	1.18 ± .007
$\Delta_a \leq 130$			1.14 ± .06	1.13 ± .06
$\Delta_a \leq 50$			1.085 ± .005	1.080 ± .005
$\Delta_a \leq 10$			1.050 ± .008	1.027 ± .005

Table 9: Mean number of hits per event $\langle n \rangle$ for different limits in the cluster matching.

4.4 Determination of detector locations

Having now two dimensional hits of each detector in its local coordinate system, the next step is to transform them into a common 3D coordinate system, to reconstruct tracks of the penetrating particles.
The offsets between the detectors have to be measured and one point (+ beam axis) is going to be fixed, to define a 3D coordinate system neglecting rotations of detectors. There are different methods to determine the detector locations (offsets) like:

1. Measurement with a ruler

2. Photometry: Put markers an all planes, take pictures with fixed focus, determine 3D informations from marker deformations on the pictures, determine coordinates of planes.

3. Cluster delta method: Determine for individual tracks the difference between the same projection of different detectors. The offsets show up as peaks in the histograms.

4. Millipede algorithm: Minimizing a χ^2 function for angles, offsets, and pitches of all detectors using tracks and starting values.

Method one is not precise enough to deal with offsets in the μm range and some measurements are not applicable. Photometry was used to get starting values for the z positions of the detectors. The precision is supposed to be in the order of $100\,\mu m$ [51].
The 4th method delivers the most precise results, but takes beside a big technical effort to integrate this Fortran coded algorithm into our C++ analysis frame work, also very good starting values for all parameters to converge in finite time.
Therefore method 3 is used at this point to obtain the x and y offsets of all detectors to each other. Taking the z position from photometry enables the transformation from 2D detector hits into 3D space points, which are used to determine tracks.
The *CBTRoughAlignment* plugin generates the so called delta histograms. Hereby the same projection (x or y) of two different detectors (Sil1, Sil2, GEM1, GEM2) are selected and the value of (position_1 - position_2) is histogramed.
The plots in figure 41 show examples of delta histograms. The distributions can be described with Gaussians, where the fitted mean value represents the offset between both detectors. Table 10 contains all offsets between two detectors from gaussian fits applied onto the delta histograms.

The distributions in the delta plots show a broadening for detector pairs with larger distances, i. e. combining Sil1/GEM1 with Sil2/GEM2.
To check the determined offsets on consistency, take two successive detector pairs and compare it with the directly obtained offset, e. g. (Sil1 - GEM1) + (GEM1 - GEM2) versus Sil1 - GEM2. Using the numbers from table 10 one gets -38.39 mm + 22.09 mm = -16.30 mm, which fits within the errorbars to

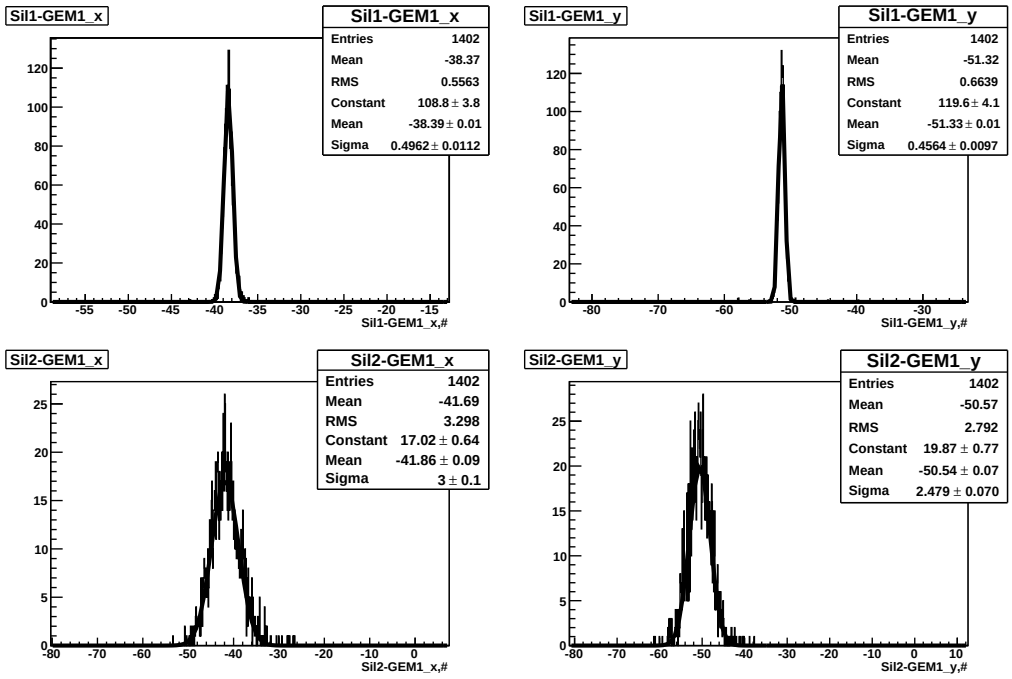

Figure 41: Delta plots for GEM1 versus both silicon detectors in x and y projection. Detector position differences in mm.

Detectors	x projection	y projection
Sil1 - GEM1	-38.39 ± 0.01 mm	-51.33 ± 0.01 mm
Sil1 - Sil2	3.44 ± 0.01 mm	-0.71 ± 0.06 mm
Sil1 - GEM2	-16.26 ± 0.09 mm	-50.78 ± 0.08 mm
Sil2 - GEM1	-41.86 ± 0.09 mm	-50.54 ± 0.07 mm
Sil2 - GEM2	-19.76 ± 0.01 mm	-50.11 ± 0.01 mm
GEM1 - GEM2	22.09 ± 0.01 mm	0.500 ± 0.09 mm

Table 10: Offsets between 2 detectors from fits on delta histograms.

the directly obtained -16.26 mm.
The precision of this measurement is determined by the errors of the fits, so the resolution is $\lesssim 100\,\mu m$.
It is necessary to fix one detector position and use the offsets of the other detectors to the first one, to obtain the x and y coordinates of a global coordinate system. The most upstream detector (GEM1) is fixed and the other detectors do have offsets listed in table 11. In the recent analysis the tilt angles of the detectors are neglected and the z coordinate is averaged over the detector plane, this determines the systematic error. The silicon strip detectors consist out of 2 sensors with 3 mm gap, but only the upstream one is measured. Since the hits are treated as originating from one detector, the z coordinate can be approximated by the middle of the sensors gap with a gap/2 error.

	x coordinate	y coordinate	⟨z⟩ coordinate
GEM1	0.0 mm	0.0 mm	0.0 mm
GEM2	22.09 ± 0.01 mm	0.50 ± 0.09 mm	618.5 ± 0.5 mm
Sil1	38.39 ± 0.01 mm	51.33 ± 0.01 mm	85.4 ± 1.5 mm
Sil2	41.86 ± 0.09 mm	50.54 ± 0.07 mm	528.1 ± 1.5 mm

Table 11: Coordinates of the individual detectors in the global coordination system. GEM1 is fixed at the origin.

4.5 Track fitting and detector resolution

The offsets of all tracking detectors in the global three dimensional coordinate system let transform the local 2D hits in each detector into 3D space points. In absence of magnetic fields and neglecting the effect of multiple scattering the trajectories of particles are straight lines.
Mathematically a line is defined by two points, but the measured hit points have a finite resolution and error, so having four points and using a χ^2 minimization method reduces the impact of these errors.

Assume each of the 4 tracking detectors delivers a hit point $\vec{\xi}_i = (x_i, y_i, z_i)$ with i $\epsilon\{1, 2, 3, 4\}$. Since the z coordinates are fixed, a straight line can be described by

$$\vec{f}(z) = (m_x z + c_x) \cdot \hat{e}_x + (m_y z + c_y) \cdot \hat{e}_y + z \cdot \hat{e}_z.$$

The four parameters m_x, m_y, c_x, c_y are variated to minimize

$$\chi^2 = N \sum_i |(\vec{f}(z_i) - \vec{\xi}_i)/\epsilon_i|^2,$$

where ϵ_i are the errors of the detectors and $N = \sum_i \epsilon_i^2$ the normalization factor. In first order approximation the detector pitch can be used as error, because the resolution is proportional to the pitch.
Starting values for the parameters can be extracted from the outer most detectors (GEM1 and GEM2):

$$m_x = \frac{x_4 - x_1}{z_4}, \quad c_x = x_1, \quad m_y = \frac{y_4 - y_1}{z_4}, \quad c_y = y_1.$$

The equations simplify, because $z_1 \equiv 0$.
If there are more than just a single hit per detector, all combinations have to be taken into account. An upper limit for χ^2 value (χ^2_{cut}) would be needed to be introduced, to reject wrong combinations of hits or tracks of scattered particles.
Having now the parameters of the fitted line, the residuals can be calculated by

$$\delta_i^x = (m_x z + c_x) - x_i, \quad \delta_i^y = (m_y z + c_y) - y_i.$$

There are three types of residuals. For resolution determination unbiased residuals s are needed. Unbiased means that they are independent of the measurement. If the detector under investigation is included in the track

fitting, the obtained residuals are called biased inclusive (δ^{incl}), because the track fit depends on the detector. Dismissing the detector in the track fit, one gets biased exclusive residuals (δ^{excl}), because the track resolution will be worse. In case of a finite track resolution it reveals $\delta^{incl} < s < \delta^{excl}$.
Only the biased residuals are obtainable from real data, but [55] shows that the geometric mean of both biased residuals corresponds to the unbiased one:

$$s = \sqrt{\delta^{excl}\delta^{incl}}$$

The application of this method to calculate the unbiased residuals from data[57] delivers the results listed in table 12 and examples for biased residual distributions are shown in figure 42.
The unbiased residuals correspond to the resolution of the detector only if the track resolution $s_T \ll$ detector resolution s.

δ_x	GEM1 [μm]	Sil1 [μm]	Sil2 [μm]	GEM2 [μm]
inclusive	182 ± 4	3.94 ± 0.07	4.19 ± 0.08	192 ± 4
exclusive	183 ± 4	151 ± 3	160 ± 3	190 ± 4
unbiased	182 ± 2.8	24.3 ± 0.3	25.9 ± 0.4	191 ± 2.8
δ_y	GEM1 [μm]	Sil1 [μm]	Sil2 [μm]	GEM2 [μm]
inclusive	172 ± 3.5	3.88 ± 0.08	3.89 ± 0.07	170 ± 3.7
exclusive	178 ± 4	150 ± 3	146 ± 3	176 ± 4
unbiased	175 ± 2.7	24.1 ± 0.35	23.8 ± 0.3	173 ± 2.7

Table 12: Measured residual distribution widths in case of using all 4 detectors for tracking (inclusive) and discarding the detector under investigation for the track fitting (exclusive). Row three shows the calculated unbiased residuals s.

In case of N identical detectors with resolution s forming a beam telescope, the track resolution can be determined by $s_T = s/\sqrt{N}$ [56]. Since the resolutions of our detectors are not identical, the geometric mean is used to determine the track resolution.

$$s_T = \frac{\sqrt[4]{s_1 s_2 s_3 s_4}}{\sqrt{4}}$$

Plugging in the number from above one gets:

$$s_T = (34.3 \pm 0.25)\mu m$$

Since s_T is not much smaller than the unbiased residuals, the latter ones are not identical to the detector resolutions. The real detector resolution is better. The resolution of segmented detectors, where only a single strip is hit, is given by pitch/$\sqrt{12}$. In case of the installed GEM detectors a resolution of 115 μm and 14 μm for the silicon strip detectors are estimated that way. In case of multiple strip hits, which is very likely as shown before, the resolution will improve more.
Comparing these with the determined unbiased residuals it turns out that the

[57] File: run-1290.001.raw.

estimation is 40% better than the observed resolution, which is expected since s_T not $\ll s$. There are two main reasons for that: First of all the electron energy of 500 MeV is relatively low, meaning multiple scattering really matters, as shown in appendix D. The scattering angle $\theta_{1/e}$ excluding angles with a probability less than 1/e is determined for the whole beam telescope to be 0.76°.
And second the number of detectors is only 4 and two dominate the fit due to their smaller pitch/error. Therefore the track fit is effected by dismissing one detector for the fit.
Increasing the electrons' energy would reduce multiple scattering and therefore improve the resolution, because $\theta_{1/e} \propto 1/p$, but at the current location it is not possible to do. Adding more detectors to the beam telescope might bring some improvements, but the material budget and therewith the effect of multiple scattering increases as well.
For high precision tests typically 4 or 6 layers of identical detectors are used at muon beams with energies of many dozens or hundreds of GeV [56].
However, the beam telescope is working with a sufficient resolution compared to the expected resolution of the TPC.

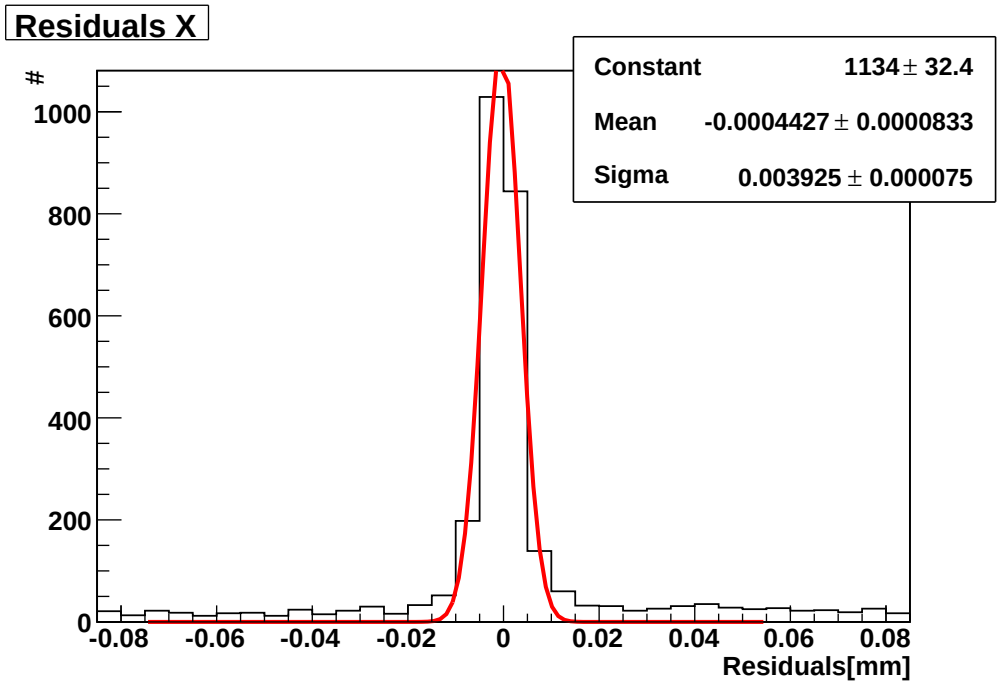

(a) Silicon 1 detector.

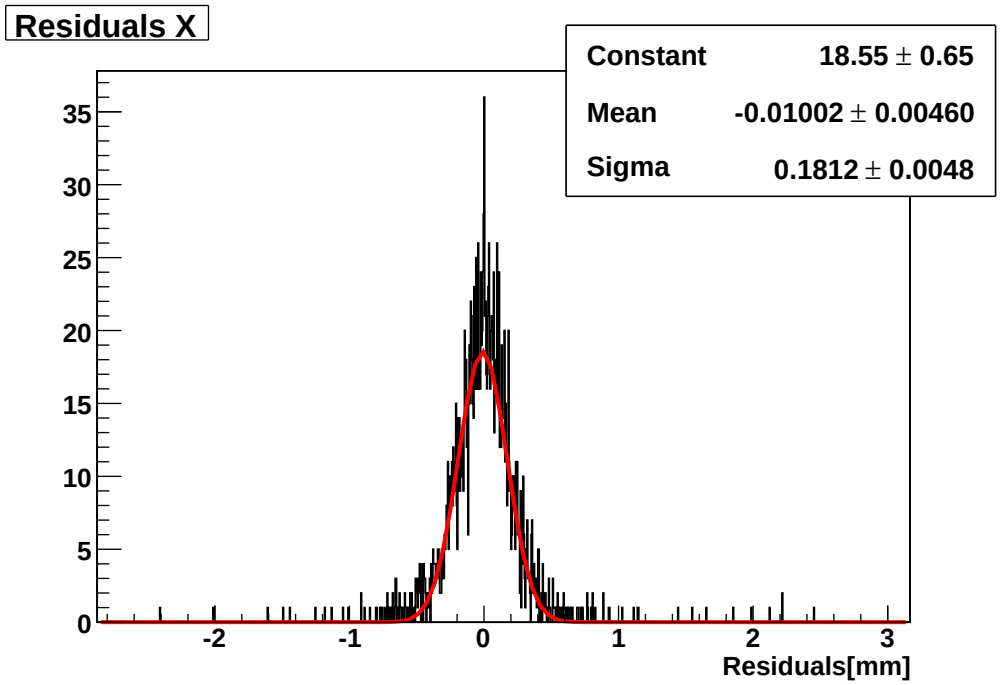

(b) GEM 2 detector.

Figure 42: Biased inclusive residual distributions for x coordinate (δ_x^{incl}) of two detectors.

4.6 Test TPC analysis

This section describes the analysis of the test TPC data from beam tests with the beam telescope. The structure of data processing is similar to the beam telescope. After the raw data decoding and mapping is done, a cluster algorithm is applied on an individual time frame, which corresponds to a slice of the drift volume. Out of the present clusters the one correlated to the tracked particle needs to be found. Then residual distributions and with that the resolutions are determined.

4.6.1 Event display

Before having a closer look at the data analysis, an event display shall show how the raw data is looking like. Figure 43 shows the track of a cosmic muon traversing the drift volume parallel to the readout plane. The mapping could not be too wrong, because the track points are all along a line. However, during the reconstruction it turned out that the x and y axis directions are inverted with respect to the beam telescope and some mapping errors are included in the provided mapping file.

In all cases not an individual track for incoming electrons is observed, but

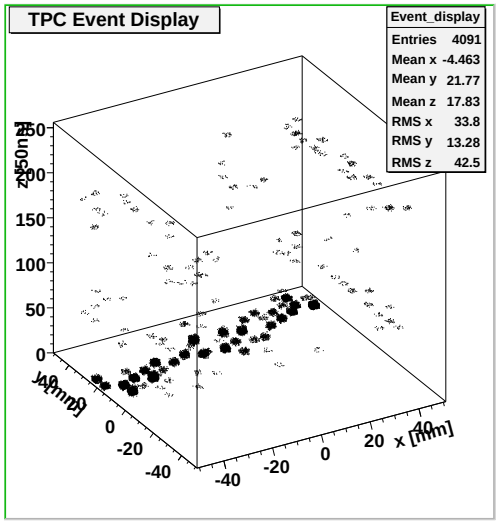

Figure 43: Event display for a track of a cosmic muon in the TPC.

always two parallel ones as shown in figure 44. This is an indication for cross talk between channels of the front end chip. Some investigations of colleagues from Munich confirm this suspicion.

4.6.2 Clustering

For performing clustering in two dimensions as it is done for the TPC pad plane the neighborhood relations need to be know. Therefore a list of neighbors for each pad is calculated by looking for pads within a certain radius around the central pad.

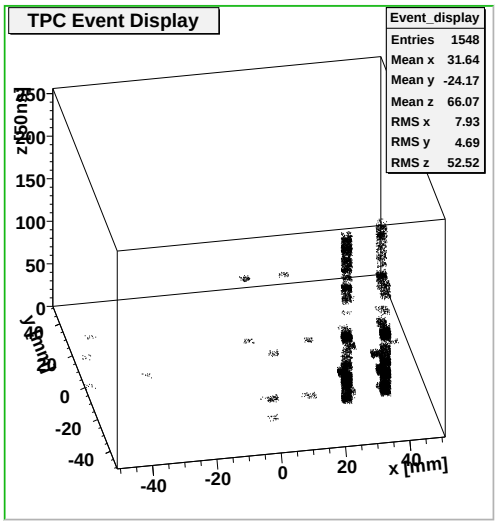

Figure 44: A double track along the z axis from the electron beam can be observed. The amplitude are almost identical with a frame, which is an indication for cross talk.

In case of the one dimensional strip detectors single strip gaps are still accepted in a cluster. In a similar way for two dimensions the search radius for neighbors can be extended, such that the next neighbor pads are also included in the neighbor list. For that reason a radius of 4.8 mm is chosen for the neighborhood determination, while having a hexagonal pad with radius of 1.5 mm and 0.1 mm gaps.
The clustering process starts with the pad of maximal amplitude, looks for hit neighbors, adds these to the cluster, and goes iteratively through all hits. Each pad can only be member of one cluster, therefore a flag is set when a pad is added to a cluster.
Some results of this clustering are shown in the following:

Figure 45 shows the energy distribution of all clusters in a run. Since no cuts are applied the distribution has an exponential behavior dominated by low energy noise. The cluster multiplicity (see figure 46(a)) reveals that there are not only real hits, which would just generate a single cluster, but also many noise hits or clusters from different tracks not correlated to the triggering particle. There are no clusters with a single pad, which is another indication for cross talk. The hitpattern of reconstructed clusters, shown in figure 47, does not show a clear beam spot like the detectors of the beam telescope do, but is almost homogeneously covered with an enhancement in the middle. This is another indication for a lot of background in the TPC, which needs to be taken care of in the reconstruction.

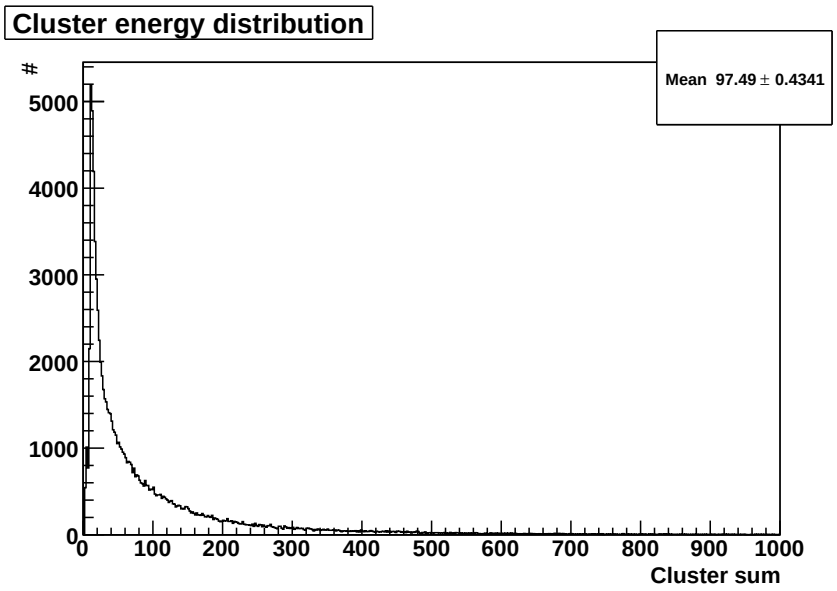

Figure 45: TPC cluster energy distribution.

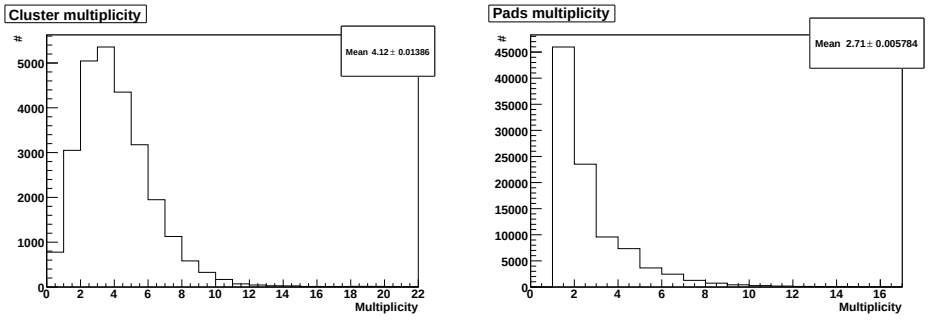

(a) Clusters per event. (b) Pads per cluster.

Figure 46: Multiplicity distributions for TPC clusters.

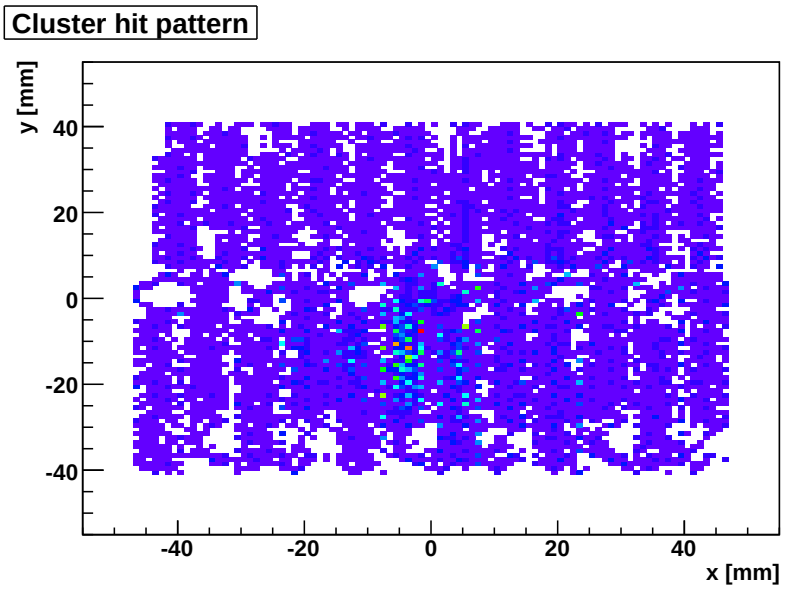

Figure 47: Hit pattern of clusters on the TPC readout plane.

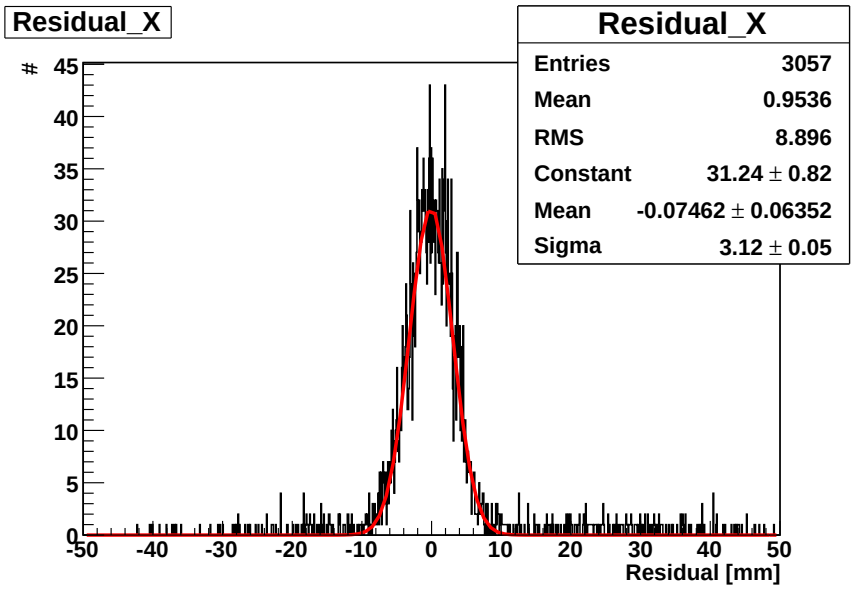

Figure 48: TPC biased exclusive residual distribution in x direction δ_x^{excl}.

4.6.3 Resolution

To obtain the residual distribution and therewith the resolution, it is important to get rid of the not correlated clusters in the TPC. The cluster energy is not a good handle on uncorrelated clusters, therefore another method is implemented. Particles' tracks are fitted by the beam telescope, then the fits are extrapolated to the TPC and the residuals of all clusters are determined. Only the clusters with the smallest residuals per event are considered to be correlated hits and therefore plotted in the residual distribution.
This method delivers the biased exclusive residual distributions for the x and y projection of the TPC. Figure 48 and 49 show the residual distribution for time frame 75, which corresponds to a drift length of 21 mm. Here one gets $\delta_x^{excl} = 3.12 \pm 0.05\,\text{mm}$ and $\delta_y^{excl} = 2.53 \pm 0.045\,\text{mm}$.
To determine the resolution of the TPC, the unbiased residuals are needed. To obtain these, the inclusive biased residual distribution have to be generated and then, like for the detectors of the beam telescope, the geometric means of both biased residuals are the unbiased ones.
The selected TPC clusters, which are supposed to be correlated hits, are fed into another track fitting procedure with the beam telescope, to determine δ^{incl}.
It turns out that the inclusive and exclusive biased residuals are the same, so corresponding to [55] the biased residuals are identical to the unbiased ones s, which then represent the detector resolution, because $s_T \ll s$. Therefore the exclusive residuals and the resolutions are set equal in the following.
Even with the low pad multiplicity per cluster, as shown in figure 46(b), a resolution of $\sigma \approx d/\sqrt{12}$ should be achievable[58]. But in the case of the test TPC a resolution of approximately the pitch could be obtained only, which is

[58] For pitch d = 3 mm $\rightarrow \sigma \lesssim 870\,\mu m$.

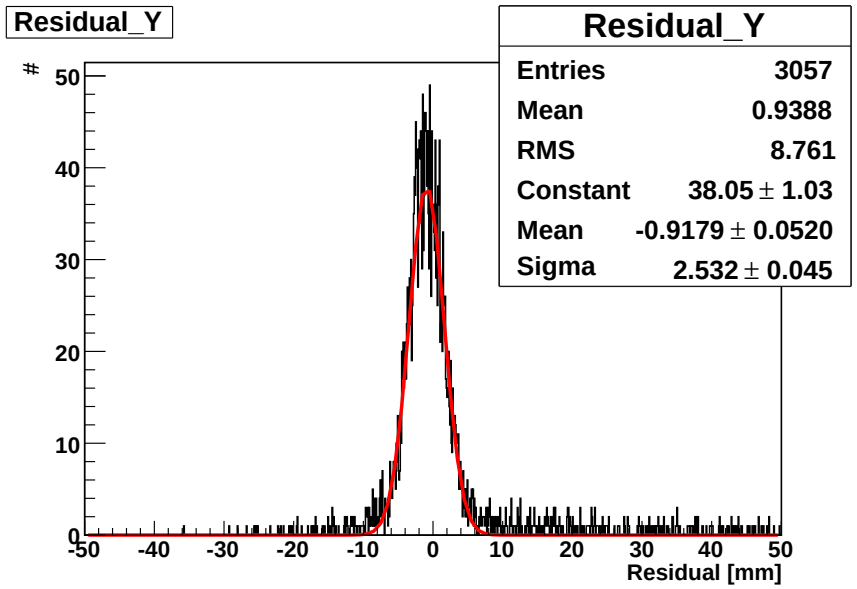

Figure 49: TPC biased exclusive residual distribution in y projection δ_y^{excl}.

dominated by the cross talk, the multiple scattering in the drift cathode[59] (as discussed in appendix D), and the mapping errors.
Also the noise and gain of the front end electronic is not optimal nor equal on all channels. Another point is the non perfect alignment, like for the beam telescope only offsets but no rotations are taken into account, which will result in a worse reconstruction than it actually is.

Figure 50 shows the TPC resolution in dependency of the drift length (z coordinate). As expected the resolution worsen with longer drift lengths corresponding to the formula

$$s_x(z) = \sqrt{const + \frac{C_D^2}{N_t^{eff}} z},$$

from [55] with $s_x(z)$ the x resolution, C_D the transversal diffusion constant, and N_t^{eff} the effective number of primary electrons in the cluster.
A fit on the data in figure 50 delivers $\frac{C_D^2}{N_t^{eff}} = 0.063 \pm 0.008\,\text{mm}$. The transversal diffusion constant for $ArCO_2$ (70:30) at a drift voltage of 250 V/cm was calculated to be $C_D = 0.01641\,\sqrt{cm}$ [52]. Thus

$$N_t^{eff} = 23.4 \pm 3$$

can be determined. Therewith N_t^{eff} is 25% bigger than in [55], which indicates a low charge loss during the drift by recombination or attachment, as well as a good ionizability of the active medium.
For short drift lengths, i. e. primary ionization close to the GEM stack, the

[59] Drift cathode consists out of 2 mm FR4, 35 μm Cu, 4 μm Ni, 1 μm Au.

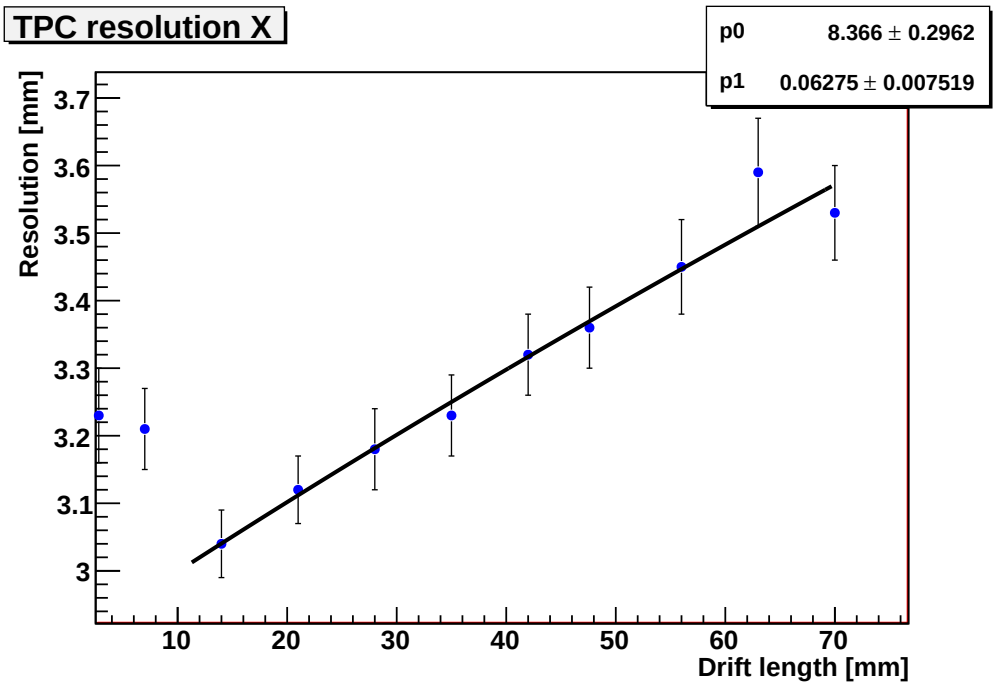

Figure 50: Resolution in x projection in dependency of the z coordinate of the primary ionization. Including a fit of the $s_x(z)$ function on the data points.

resolution is not dominated by diffusion, but by the lower pad multiplicity. This effect is also present in the resolution studies shown in [55].

4.6.4 Conclusion

These results show that the 2D reconstruction of the TPC is working and the effects of different detector parameters like drift voltage, gas mixture, and charge amplification can be studied. However, for the analysis two more features need to be included, in particular the cross talk cancellation and the re-mapping of the pads. Regarding those effects the resolution of the test TPC is expected to become much better.
Limiting factor is then the multiple scattering, which can be overcome by increasing the electron momentum. This might be possible by moving the beam telescope to another location, e. g. at the end of the photon beam line in the Crystal Barrel area, where electrons with up to 3.5 GeV/c momentum are available, that means multiple scattering is decreased by a factor of 7. Unfortunately an electron beam at that location is not allowed in the current operating license of ELSA.
For the final detector the origin of the cross talk has to be located and removed if possible, otherwise the aspired performance will never be achieved. The documentation in the designing and assembling phase has to be reliable, so that the mapping of the pad locations and the data is clear.
Characterization and optimization of the front end electronics is ongoing, but the results are already promising.

Vivere militare est.
Seneca

5 Final TPC implementation

This section deals with methods for calibrating a TPC especially with a focus on the constraints for the Crystal Barrel TPC, and describing the specifications and status of the final TPC.

5.1 Crystal Barrel TPC

In parallel to the testing and studying of the test TPC, the final one for the Crystal Barrel experiment was constructed by the GSI detector lab and the manufacturing process is ongoing.
The TPC has the shape of a hollow cylinder with a flange (media flange) at the upstream side of the TPC. The vessel is made out of a sandwich structure of Rohazell and Kapton. On the inner side there are staggered strip lines on the Kapton foil supplied by SMD resistor chains to generate the electrical drift field along the z axis, which makes the electrons drifting to the readout plane. The central part is the modular media flange, which houses the amplification, the readout, and the supplies. It also makes the connection between the drift volume (vessel) and the readout.
The readout of the TPC will be the same as for the test TPC, so the debugging and optimization work for the electronics, the readout, and the decoding can be or is already done now. This was the major goal of the tracking test bench and the studies of the test TPC. For sure the development and application of the analysis software is the second important reason.

How the final TPC will be located inside the calorimeter is shown in figure 51. In addition the solenoid with return yoke (blue), which cover the complete Crystal Barrel detector, and the polarized target with its horizontal cryostat is displayed.

Figure 52 shows a closer view of the cross section. The readout and the media flange are located on the upstream end (right hand side) of the TPC. The mounting of the TPC is done only at the media flange with a half cone fixed to the calorimeter support structure, so that no additional material in forward direction is needed.
All connections to the TPC are on the media flange and the cables are routed along the cryostat out of the return yoke.
The dimensions are very tight; there is only 5 mm radial distance between the field cage and the opening of the calorimeter. The inner edge is close to the target cryostat and in between there might be a scintillating fiber detector to generate a start signal for the TPC.

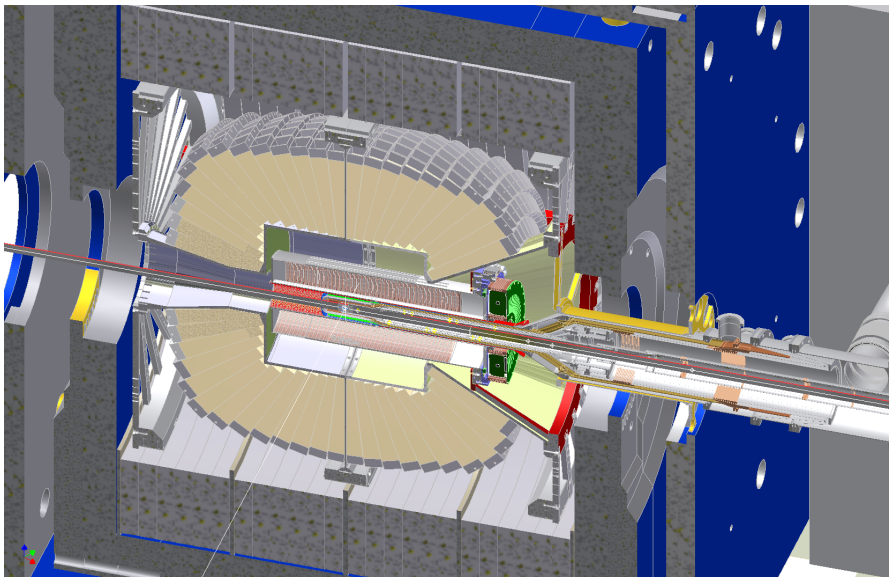

Figure 51: Crystal Barrel calorimeter inside its solenoid with TPC and polarized target.[53]

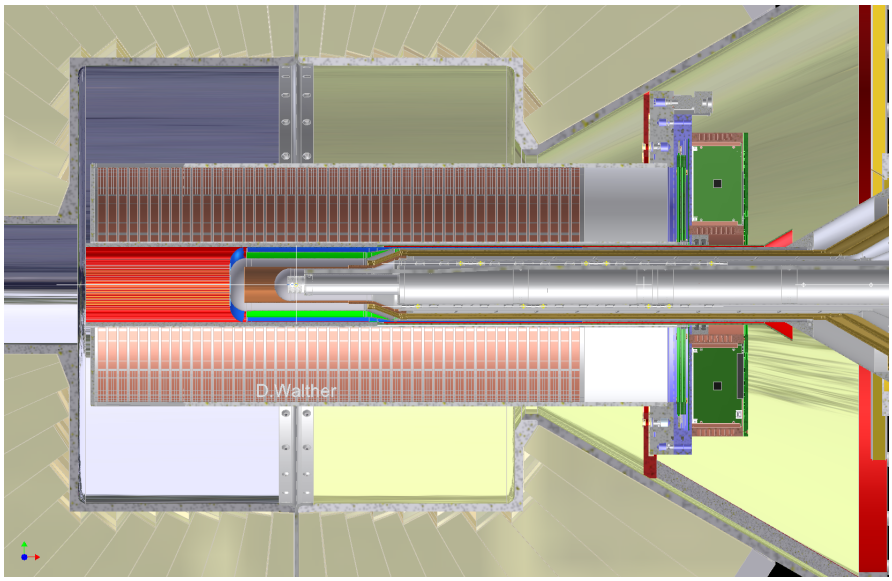

Figure 52: Cross section of the Crystal Barrel detector with TPC and polarized target. [53]

The following specification for the TPC are fixed:

$\varnothing_{out}$	300 mm
$\varnothing_{in}$	105 mm
Drift length	800 mm
Drift voltage	400 V/cm = 32 kV
Amplification	Triple GEM stack
Pad plane	$\approx$ 10000 hexagons (r = 1.5 mm)
Readout circuit	42 x 4 AFTER chips

After manufacturing of the TPC at GSI first test will be carried out there. Then the detector is supposed to be tested in the FOPI experiment with heavy ion beams and electrons on the tracking test bench at ELSA. The installation of the TPC inside the Crystal Barrel experiment is not going to happen before 2011 as discussed in 1.2.3. However, there is a lot to do before the installation of the TPC in the experiment, the detector and the software can be studied and optimized in the mean time with cosmic muons and the beam telescope.

5.2 Calibration of a TPC

This subsection discusses calibration methods for a TPC with respect to the constraints of the Crystal Barrel experiment.
At first one has to consider which parameter have to be calibrated and monitored to reconstruct particles trajectories and to do particle identification.

- **Drift velocity** v_d
  needs to be know to determine the z positions of the primary clusters.

- **Field distortions**
  generate displacements of primary clusters and therefore worsen resolution.

- **Gain of each channel**
  has to be equalized to have optimal resolution for the center of gravity fit for clusters.

These three items are the most important ones. Methods to measure and calibrate them are presented in the following.

5.2.1 Drift velocity v_d and field distortions

The drift velocity depends on many parameters like gas mixture / impurities, temperature, pressure, electric field strength and many more. It is not possible to control all of them at sub percent level, therefore techniques to measure v_d directly are necessary. Since there may be inhomogeneities in the drift gas, the drift velocity does not need to be constant in the whole drift volume. Therefore measuring this quantity only at one point, e. g. in an external chamber in the gas outlet, can only be a rough estimate.
A second method is to use cosmic muons the measure the drift velocity inside

the active volume of the TPC. Herefore external tracking and timing is necessary to determine the actual drift length and time, to calculate v_d. In case of the TPC for the Crystal Barrel detector with $\sigma_z \approx 1\,\text{mm}$ it would be sufficient to know the muon track within the same size, so an array of scintillating fibers (1 mm diameter) would do this job. In addition this method delivers straight tracks and field distortions can be corrected by comparing the reconstructed track with the externally define one.
A third option is to generate a grid of UV laser tracks inside the drift volume, which ionize the gas (actually the gas impurities and the field cage material) via photon effect. Since the laser is pulsed, the starting drift time for the primary ionizations is known and the drift length is fixed by the laser beam position. The relative drift velocity resolution σ_{v_d}/v_d of the ALICE TPC was measured with such a laser system to be $2 \cdot 10^{-4}$ [57].
The HARP TPC [58] instruments another technique. Here ultra violet laser light is coupled to quartz fibers. Their second ends penetrate the drift cathode, entering the drift volume, in a symmetric grid. The fiber tips are coated with some atomic layers of aluminum, so a laser pulse can generate some free electrons via photo effect on the tip. This grid of pulsed electron sources can be used to measure the drift velocity at several points and to determine field distortions, which would lead to displacements in the reconstructed origins of the electrons.

Taking now the constraints of Crystal Barrel TPC into account, the laser track method has be discarded, because there is no space to feed in the laser beams into the TPC. This TPC has only active volume inside the field cage. Putting in some optics would reduce the active area too much.
The HARP design is a nice idea, but quartz fibers can stand only a large bending radius and therefore need a lot of space in forward direction, which is not present. In addition the material budget is non negligible increased by the quartz fibers. One can think about alternatives to produce electrons, which would mean a Go for this technique:

- UV LED with metal coating: Not feasible due to light intensity and power dissipation.
- Controlled field emission: Is working only in vacuum properly. In parallel it would generate field distortions.
- Triggered α source: An emitted α particles ionizes some drift gas and is then detected in a PIN diode (For more details see E). Not clear if technical realizable.

As long as there is no reliable triggered electron source available, cosmic muons are going to be used, to measure the drift velocity and field inhomogeneities.

5.2.2 Pad gain

In general the amplification of the GEM stack can not be considered as homogeneous and the pad response functions (PRF), i. e. the factor between charge on the pad and the digitized value, of all pads will differ.

When calculating the center of gravity of a charge cloud unequal pad gains move the reconstructed away from the real one. A measurement of the pad gain and the calibration is inevitable.
Having an equalized gain also clears up the dE/dx vs. p_t correlation, which is used to perform particle identification, and the separation power between the different species is increased.
Two common methods for energy calibration of TPCs are presented in the following:

Cosmic muons

Minimal ionizing particles like cosmic muons deposit energy in the drift gas while traversing the TPC. One can think of hexagonal rods with the readout pads as surface filling the whole drift volume. Each of these virtual rods can be treated as individual sample of dE/dx, so a Landau distribution is expected to appear. The mean energy deposition per rod is calculated to be 650 eV. Assuming an ionization energy of 20 eV, one gets approximately 32 electron ion pairs, so the Landau fluctuations[60] can be estimated by $\Delta N/N = \sqrt{N}/N = 17.7\%$. To trigger on cosmic muons traversing the TPC one needs scintillators with a finite size, what yields to track length variation which also contributes to the energy resolution. However, the error for a 5 cm wide scintillator is less than 1%. The length of the scintillator (along x axis) introduces already for the test TPC (100 mm active length) and track length error of 8%. By far the biggest error is coming from the pad shape. The hexagon can be decomposed into a rectangle and two triangles. For vertical tracks the projected track length on the pad is constant for the rectangle, but does down to 0 at the corners of the triangles. This means 30% of the tracks have a different dE/dx as expected. So either one takes these into account and smears out the spectrum, or one discards these hits, using the neighbor pads as veto, and reduces the statistics by one third.
So this method is just a rough approach to get an estimation for the energy calibration factors. However, having data of cosmic muons from the drift velocity measurements, one should use it.

Kr method

For this method a ^{83}Rb source is installed in the gas inlet of the TPC. The rubidium isotopes decay via electron capture into the isomer ^{83*}Kr with a half life of 83 days [59]. This krypton is transported with the drift gas into the active detector volume, where it decays isotropically with a half life of 1.86 h via γ-cascades to ground state. The emitted photons have energies between 8 and 42 keV, which fit to the dynamic range of the digitizer.
The TPC has to be readout continuously to detect the clusters from emitted photons. Since there is not only a single photon energy, but many with well known energies, one can adjust the pad gain and in parallel check the linearity of the whole readout circuit. Actually an absolute energy calibration is possi-

[60] Fluctuations of generated e^- ion pairs (or photons) due to statistical nature of the process.

ble.
The electron clouds after the amplification spread over many pads, therefore one needs to sum over the full cluster to obtain the energy correctly. It needs an iterative calibration process to determine the gain of individual pads and having starting values from different methods - like cosmic muons - will lead to a quicker convergence.
This method is used for many years now successfully for instance in the ALICE TPC[57].

5.2.3 Conclusion calibration

The major tool for calibrating the TPC will be cosmic muons, because these enable a first energy and gain calibration in parallel to drift velocity and field inhomogeneity measurements. The Kr method will improve the energy calibration quite well. All the other techniques are not applicable in the Crystal Barrel TPC, but the important parameters can be calibrated anyhow.
As soon as the detector is assembled, filled with drift gas, and high voltage is applied the calibration can start.

Was du erstens nicht selber
und zweitens sofort erledigst,
das wird auch nichts.
H. Kalinowsky

6 Summary

The aim of this thesis was to investigate a tracking upgrade of the Crystal Barrel experiment and to start with the implementation of an adequate detector system.
In the first two chapters the current physics program and setup of the Crystal Barrel experiment was presented and the consequences to introduce tracking of charged particles was discussed. This upgrade will not only improve the number of detectable decay channels for single and double meson photoproduction experiments, but will also allow to measure further quantities like the transversal momentum of charged particles, the sign of charge, precise tracks, and vertices, which all help to identify further reactions like hyperon production. Including a transversally polarized target it will be possible to have the first complete experiment ever performed.
After I have done simulations of reactions with charged final states, boundaries and constraints for a tracking detector were fixed. Then three detector concepts - silicon strip tracker, SPC, and TPC - were discussed and checked corresponding to the fixed design parameters and further experiment's constraints. Especially I studied the transversal momentum resolutions by developing a parameterized model. The model predictions for a detector system, which was already simulated, were cross checked. The model predictions turned out to be good estimations within a systematic error of 20%.
Finally the decision to build a TPC as central tracker for the Crystal Barrel experiment was made, because this concepts fits best to the constraints for the central tracking detector.
To be able to investigate tracking detectors like a TPC, study individual components, and to develop the necessary software tools, I have planned, installed, and commissioned a tracking test bench on an electron beam at ELSA. The setup consists of a beam telescope, which is built out of 2 silicon strip detectors and 2 planar GEM detectors, and a test TPC, which carries all major components of the final one.
I have performed an analysis of data taken with an electron beam and the track resolution of the beam telescope was determined to be better than $35\,\mu m$. Afterwards I measured the resolution of the test TPC. It turned out that the TPC did not fully comply with the design goals, but the hard- and software are working, I have revealed the issues and presented solutions. However, the desired systematic studies can be performed and individual parameters can be optimized with beam data in the next runs.
Chapter 5 shows the planned integration of the TPC into the Crystal Barrel experiment with the fixed design parameters for the detector. In addition calibration concepts for a TCP in general are discussed and their feasibility for the Crystal Barrel TPC were investigated.

To conclude: A central tracker improves the Crystal Barrel experimental setup, albeit to the cost of big efforts and non negligible financial resources, but the realization is feasible and on-going.

7 Acknowledgements

First of all I would like to thank Prof. Dr. Reinhard Beck for trusting me and giving me the opportunity to work in the exiting field of tracking detectors in hadron physics. Due to the granted freedom I could learn a lot also beyond my direct research tasks.
My mentor of the Bonn Cologne Graduate School of Physics and Astronomy, Prof. Dr. Hans Ströher, who is also the second referee for this thesis, I want to thank for his advices and comments on my work and future career.
I also appreciate Prof. Dr. Ulf-G. Meißner and Prof. Dr. Peter Martini for being referees of my dissertation.
A great thank goes to the CBELSA/TAPS collaboration, which provides me a lot of challenges to tackle and a great learning curve since my very first days as working student.
I want to thank all my colleagues from the working groups Beck, Brinkmann, and Thoma for the good support, their patient with me, and hints for improvement. A special thank for sure to my room mates - Manuela Gottschall and David Kaiser - who endured me in the last years, always had an open ear for my problems and complains. I appreciate Roman Schmitz's work on the software and simulation, which actually enables me to perform the analysis of the beam data. A thank also to the technicians and work shops of the HISKP, which had done very good jobs at the mechanics of the test bench.
The GemTPC collaboration under the leadership of Bernhard Ketzer and Bernd Voss offers me great opportunities to learn a lot in setting up, commissioning, and operating tracking detectors with all the necessary infrastructure, which I really appreciate.
The wise and calming words of the experienced people really helped me to endure my challenges.
I have to thank the Bonn Cologne Graduate School of Physics and Astronomy for the support in the last two years.

Thanks to my friends and family for accompanying me through the time of graduating with many motivating words, preventing me from loosing my head and courage, and opening my eyes to different point of views. Especially I want to thank my parents for making me interested in science and technical things from an early stage on, enabling me to do my studies, and providing everything I needed.

Appendices

A Phase space simulations

The phase space simulations are performed via root macros.

```
Double_t masses[2] = { 0.938, .135} ; // mass of proton and pi0 [GeV/c^2]
Double_t E_min = 0.2;
Double_t E_max = 3.5;
Double_t E_gamma = E_min;
Double_t proportional_const = 25000.;

TGenPhaseSpace gevent;

while (E_gamma <= E_max) {
for (int a = 0; a < (proportional_const/E_gamma); a++) {
TLorentzVector beam(0.0, 0.0, E_gamma, E_gamma);
TLorentzVector W = beam + target;
gevent.SetDecay(W, 2, masses);
Double_t weight = gevent.Generate();

TLorentzVector *pProton = gevent.GetDecay(0);
TLorentzVector *ppi0    = gevent.GetDecay(1);

// Fill histograms with theta(), Pt(), ..

}
E_gamma += 0.01;
}

// Plot histograms
```

At first an array of the masses of decay products are defined. Since a 1/E photon energy distribution is used as beam, the minimal and maximal energy has to be fixed as well. Then an object of the type *TGenPhaseSpace* is generated. In the following *while* loop the photon energy is going from E_min to E_max. The encapsulated *for* loop realizes the energy dependent countrates. As a first step of the event processing the photon beam is initialized and the center of mass energy (W) is calculated. The next two methods of object gevent generate the decay of the center of mass energy into the desired particles. Pointer on the generated particles are created and can be used to extract information like θ angle, transversal momentum etc. which are then filled into histograms. Decays can be cascaded, i. e. one takes a particles of the primary reaction and let it decay again with the same methods.

A.1 $\gamma p \rightarrow p\omega$

Simulation parameters:

E_min	0.85 GeV
m_ω	782.6 MeV/c^2
$m_{\pi^\pm}$	139.6 MeV/c^2

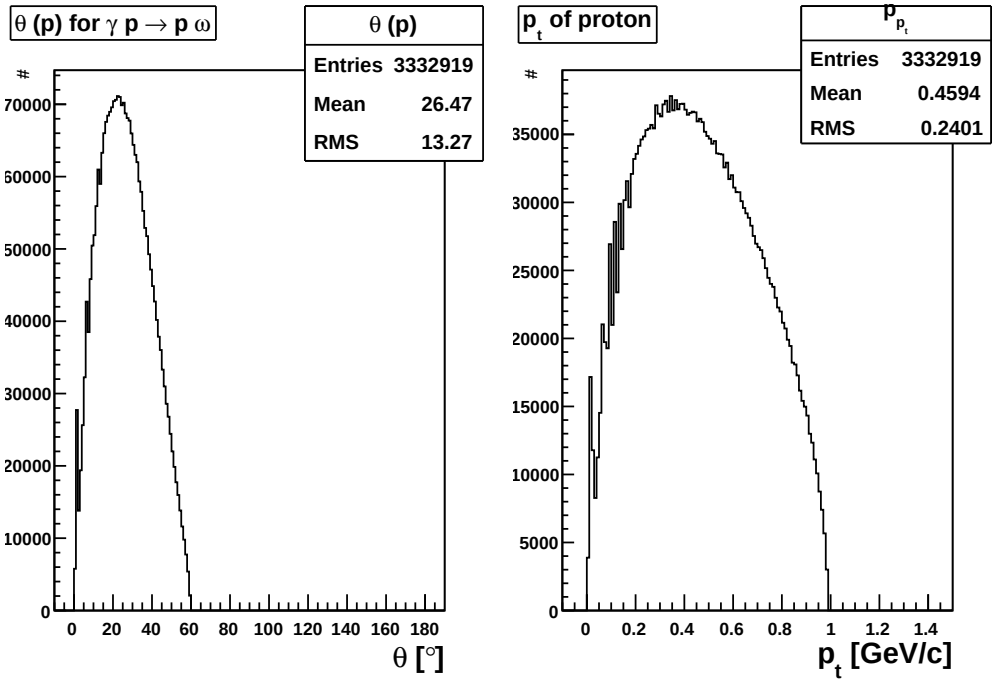

Figure 53: Polar angle and momentum distribution of the proton.

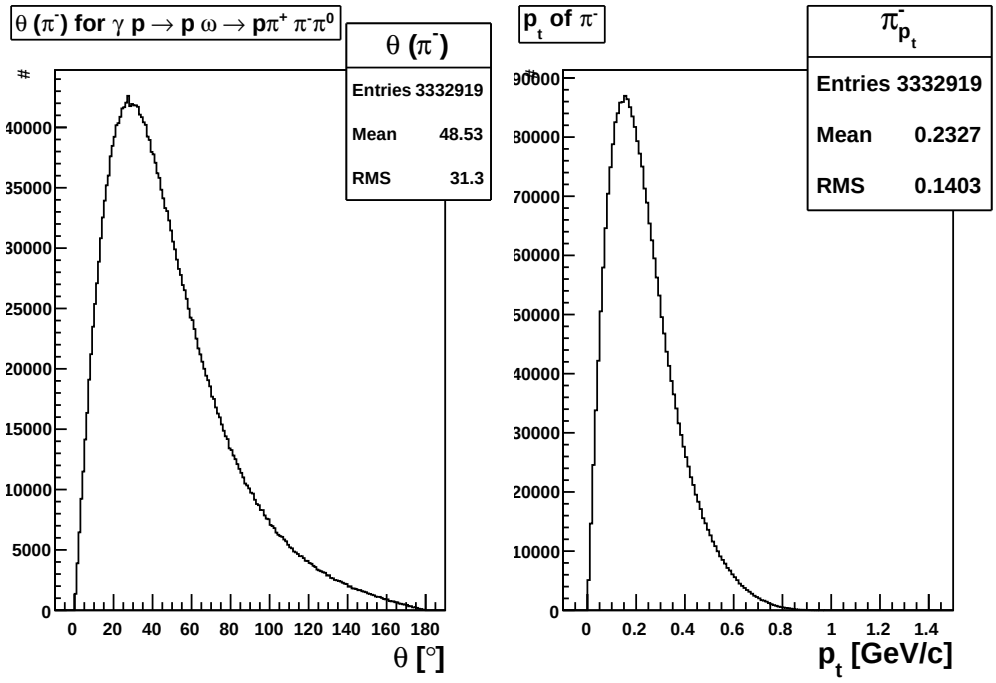

Figure 54: Polar angle and momentum distribution of the π^-.

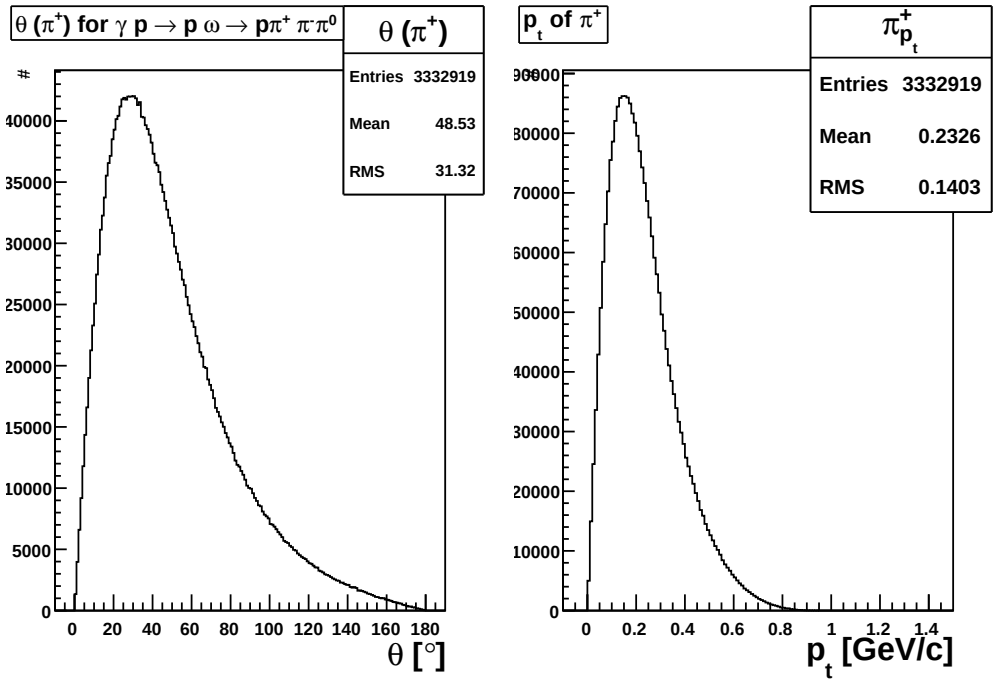

Figure 55: Polar angle and momentum distribution of the π^+.

A.2 $\gamma p \rightarrow K^+\Lambda$

Simulation parameters:

E_min	1.75 GeV
m_{K^+}	493.7 MeV/c^2
m_Λ	1115.7 MeV/c^2

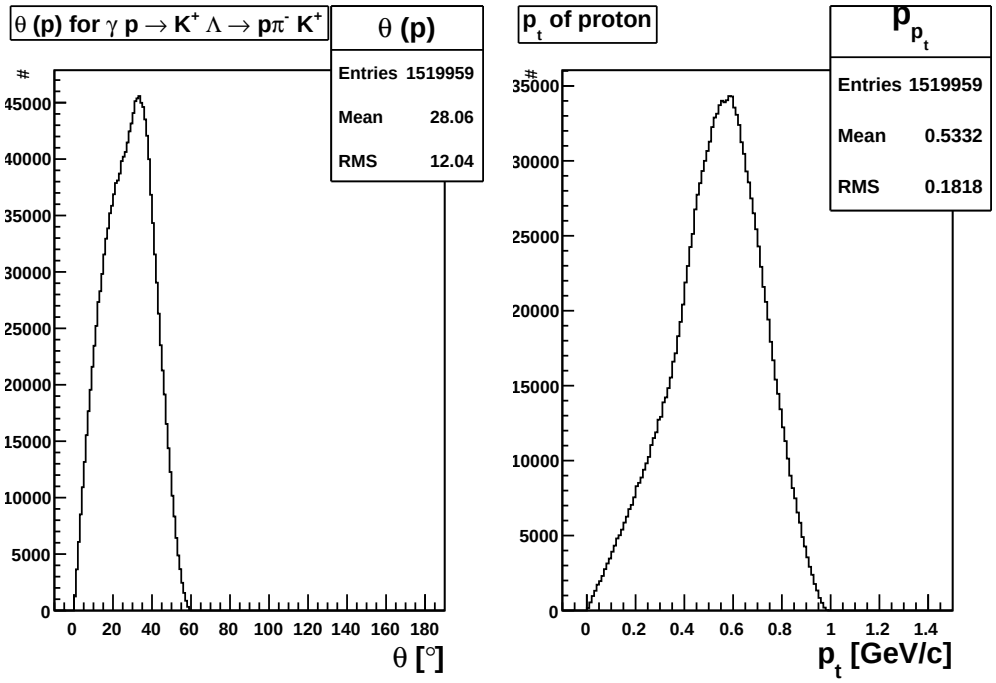

Figure 56: Polar angle and momentum distribution of the proton.

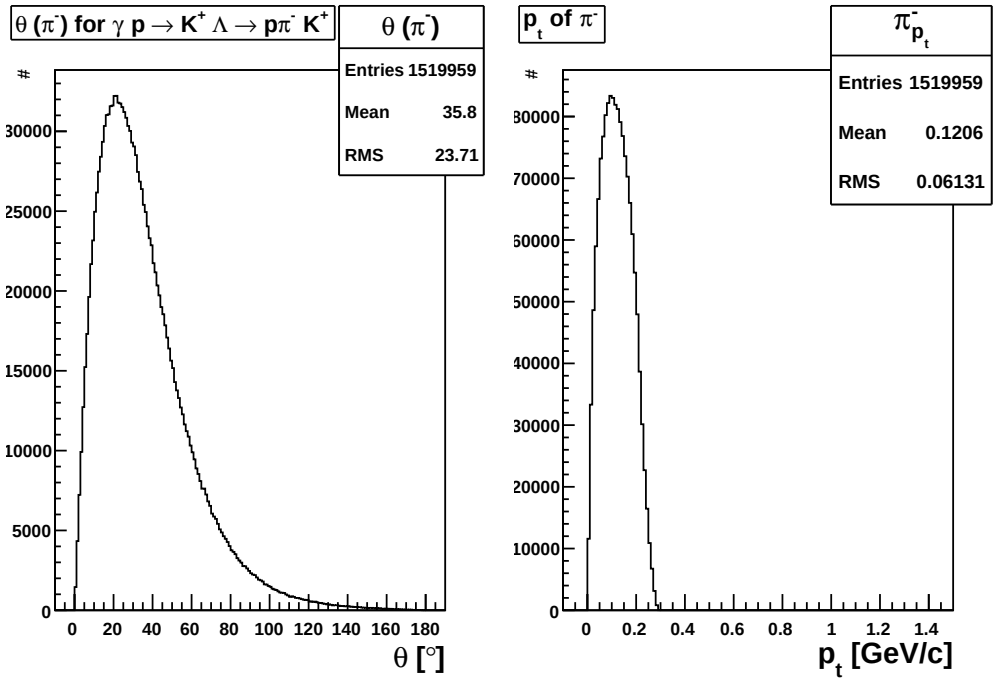

Figure 57: Polar angle and momentum distribution of the π^-.

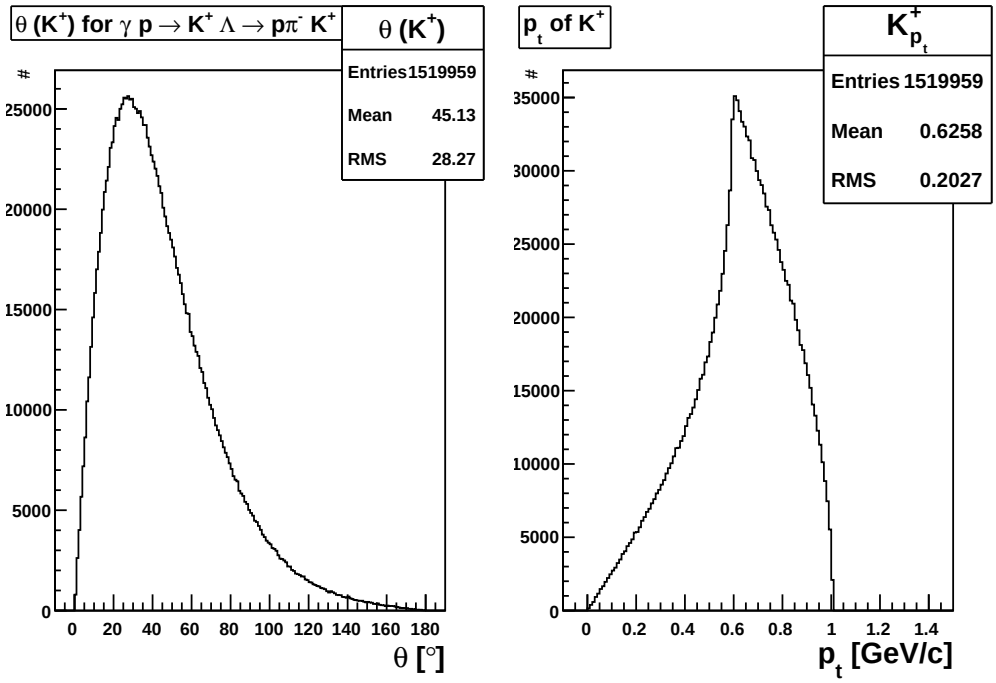

Figure 58: Polar angle and momentum distribution of the K^+.

B VME_FPGA board

During the year 2006 the need of a generic VME module arose. So I have designed a FPGA board with VME interface for 6U crates (see figure 59). The properties and recent applications are specified in the following.

B.1 Board specifications

- 6U VME board compliant to VMEbus Specification Manual Rev. C.1
- It provides an A32 D32 Interface with 16 bit adjustable base address realized in a Xilinx XC2C384 CPLD
- A Xilinx Spartan 3 FPGA is the core component
- 3 mezzanine card connectors (Samtec QFSS-052-06.25-L-D-PC4) with +5 V, -5 V, +3.3 V supply

B.2 Applications

- Trigger module
- Synchronization system for the Crystal Barrel experiment DAQ
- Video scaler with optical transmission to display experiment count rates
- APV digitizer board
- Multi threshold discriminator with rise time compensation algorithm
- Time to Digital Converter (TDC) using GP2 chips
- Logic and counter module (also software TDC with 1.25 ns time resolution)

For these applications various mezzanine cards were developed:

- NIM input / output / bidirectional
- ECL input / output
- LVDS input / output
- Optical receiver / transmitter (ST connector)
- TDC mezzanine with GP2 chips
- Programmable multi threshold mezzanine
- Sampling ADC and LVDS I/Os
- Synchronization mezzanine cards with ECL, NIM and PECL over RJ45

These mainboards have proved their stability and reliability for more than one year by now in the Crystal Barrel experiment. They were mainly used to perform the synchronization between the sub detectors to assure the correctness of the data. There was no failure in the system during the entire time of data taking.
The trigger for the test bench is also generated by such a VME board. The trigger condition including veto signals is configured via a VME register during run time. Counter for all inputs, event number, life and deadtime are included as well.
This equipment is now also commercially available at ELB - Elektroniklaboratorien Bonn UG (haftungsbeschränkt)[61].

Figure 59: VME FPGA mainboard (VFB) with NIM and ECL mezzanine plugged on.

[61] www.elbonn.de

C Test bench parameters

C.1 Silicon settings

Bias voltage V_{bias}	+35 V
Typ. bias current $\langle I_{bias} \rangle$	0.2 - 0.34 μA
APV VPSP	35
APV MODE	45
APV ICAL	0
APV CDRV	127
APV CSEL	254
APV MUXGAIN	4
APV VFS	60
APV VFP	30
APV IMUXIN	34
APV IPSP	55
APV ISSF	34
APV ISHA	34
APV IPSF	34
APV IPCASC	52
APV IPRE	92
APV LATENCY	21

C.2 GEM settings

Voltage V_0	3950 V
Typ. current I_0	722 μA
APV VPSP	27
APV MODE	13
APV ICAL	25
APV CDRV	1
APV CSEL	1
APV MUXGAIN	4
APV VFS	60
APV VFP	30
APV IMUXIN	30
APV IPSP	48
APV ISSF	30
APV ISHA	30
APV IPSF	30
APV IPCASC	45
APV IPRE	85
APV LATENCY	17

D Multiple scattering

Charged particles traversing matter do multiple scattering due to coloumb interaction with the nuclei. The angle at which the probability distribution for scattered particles drops to 1/e ($\theta_{1/e}$) is given in [54] by

$$\theta_{1/e} = \frac{17.5MeV}{p\beta c}\sqrt{\frac{L}{X_0}(1+\epsilon)},$$

with X_0 being the radiation length, L the material thickness, p the momentum of the projectile, βc the particles velocity, and $\epsilon = 0.1 \cdot \log \frac{10 \cdot L}{X_0}$.
Considering electrons with an energy of 500 MeV and silicon sensors with $300\,\mu m$ thickness, $\theta_{1/e} = 0.1°$. In case of the GEM detectors a 2 mm readout PCB is considered as dominating scattering contributor. Assuming a radiation length for the PCB material of 21 cm one calculates $\theta_{1/e} = 0.18°$.
The beam telescope consists of 4 silicon sensor and 2 GEM detectors, which contribute to multiple scattering. The overall scattering angle including all detectors is then calculated to be $\theta^{tot}_{1/e} = \sum_i \theta^i_{1/e} = 0.76°$.
To estimate the contribution of multiple scattering in the beam telescope to the TPC resolution, only the last detector infront of the TPC is taken into account, because the scattering in the previous ones is measured by the next detector. The last detector is a GEM detector with $\theta_{1/e} = 0.18°$ and the distance between it and the TPC pad plane is ≈ 330 mm, so a displacements of 1 mm can be expected. Taking also the TPC drift end plate[62] into account, which the electrons have to pass before entering the sensitive volume, the displacement $\Delta_{1/e}$ increases to 2 mm.
This displacement is dominating the residuals of the TPC.

[62] Very similar material stack compared to GEM detetcor.

E α-ionizer

The challenge is to ionize pointlike the drift gas correlated to an electrical signal. One idea is to take an α source e. g. ^{241}Am, and collimate it onto a PIN diode, which generates an electrical signal when it is hit. In the gap between source and diode the α particles ionize the drift gas. The free electrons are pulled away by the drift field to the readout plane.
Figure 60 shows a sketch of such a device with source, diode, and the direction of the traveling α particles.

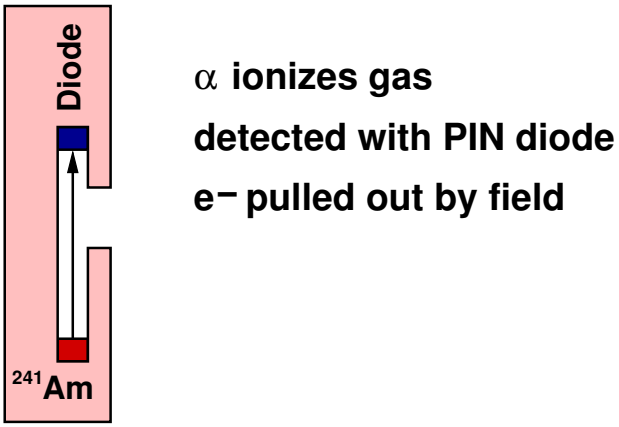

Figure 60: Sketch of an α-ionizer, where electrons are emitted to the right hand side.

Beside dealing with more than 30 kV potential the size of such a device would be crucial. The size of the source can be negligible small and the surface of the PIN diode can be in the order of 1 mm^2. The required path length L of the α particles to generate at least 100 e$^-$ ion pairs has to be estimated:

$$
\begin{aligned}
&100\ \mathrm{e}^- \text{ ion pairs with } \mathrm{E}_{ion} = 20\,\mathrm{eV} \\
&\hookrightarrow \text{Energy deposition} \geq 2\,\mathrm{keV} \\
&\text{For sufficient fast } \alpha\ \mathrm{dE/dx} \approx 470\,\mathrm{keV/cm} \\
&\hookrightarrow \mathrm{L} \gtrsim 4.7\,\mu m \text{ for } 100\ \mathrm{e}^- \text{ ion pairs}
\end{aligned}
$$

This determined required path length L is feasible for building a pointlike electron source. However, there is still the challenge with the high voltage and the efficiency of getting free electrons into the drift gas is not clear.
A drawback of this device is that the source can not be switched of or regulated somehow and one has radio active material inside the detector.

References

[1] Proceedings of the Royal Society, Series A 82: 495500, *On a Diffuse Reflection of the α-Particles* , H. Geiger and E. Marsden

[2] Philosophical Magazine, Vol 21 (1911), pp 669-688, *The Scattering of alpha and beta Particles by Matter and the Structure of the Atom*, E. Rutherford

[3] Science **124**, 103 (1956), *Detection of the Free Neutrino: a Confirmation*, C. Cowan, F. Reines (nobel prize 1995) *et al.*

[4] Phys. Rev. Lett. 23, pp. 930-934 (1969), *High-Energy Inelastic e-p Scattering at 6° and 10°*, E. D. Bloom *et al.*

[5] Physics Letters B667, 1 (2008), *PDG Particle Physics Booklet*, C. Amsler *et al.*

[6] European Physical Journal A 10(2001) 309, *Relativistic Quark Model of Baryons With Instantaneous Forces*, U. Loehring *et al.*

[7] Nuclear Physics A 657 (1999), pp 283-302, *Diquark correlations in the nucleon*, k. Shimizu *et al.*

[8] Physics Letters B 286 (1992), pp 29-35, *Baryons as bound states of diquarks and quarks in the Nambu-Jona-Lasinio model*, A. Bucker *et al.*

[9] Physics Letters B 679 (2009), pp 77-80, *Diquark correlations in baryon spectroscopy and holographic QCD*, H. Forkel and E. Klempt

[10] Nuclear Physics B 204 (1982), pp 204-212, *Quarks and diquarks in baryon string model*, C. J. Burden and L. J. Tessie

[11] Zeitschrift für Physik A 352 (1995), pp 327-343, *Photo- and electroproduction of eta mesons*, G. Knöchlein *et al.*

[12] Nuclear Physics A 285 (1995), pp 63-74, *Electromagnetic Strangeness Production at CEBAF*, R. A. Schumacher

[13] Physical Review C, Vol 55, Nr 4 (1997), *Completeness rules for spin observables in pseudoscaler meson photoproduction*, W. Chiang and F. Tabakin

[14] CERN_PPE/92-126, 1992, *The Crystal Barrel Spectrometer at LEAR*, CB@LEAR collaboration

[15] European Physical Journal A 28(2006), pp 139-148, *The Bonn Electron Strecher Accelerator ELSA: Past and Future*, W. Hillert

[16] Doctoral thesis Susanne Kammer (2009) Physikalisches Institut Bonn, *Strahlpolarimetrie am CBELSA/TAPS Experiment*

[17] Diploma thesis Christian Hammann (2009), HISKP, *Aufbau eines Flüssigwasserstofftarget zur Durchführung von Kalibrationsmessungen am Crystal-Barrel Experiment an ELSA*

[18] Nucl. Instr. and Meth. A436 (199) 430-442, *A new frozen spin target for 4π particle detection*, Ch. Bradtke *et al.*

[19] Doctoral thesis Holger Flemming (2001), Ruhr Universität Bochum, *Entwurf und Aufbau eines Zelluarlogik-Triggers für das Crystal Barrel Experiment an der Elektronenbeschleunigeranlage ELSA*

[20] Doctoral thesis Christian Funke (2008), HISKP, *Analyse der Triggerfähigkeiten zur Selektion hadronischer Ereignisse und Entwicklung eines Hochgeschwindigkeits-Triggers für den Vorwärtskonus des Crystal-Barrel-Detektors*

[21] Diploma thesis Marcus Grüner (2006), HISKP, *Modifikation und Test des Innendetektors für das Crystal Barrel Experiment*

[22] Doctoral thesis Christoph Wendel (2008), HISKP, *Design und Aufbau eines Szintillationsdetektors zur Identifizierung geladener Teilchen im Crystal-Barrel-Vorwärtsdetektor*

[23] Diploma thesis David Kaiser (2007), HISKP, *Aufbau und Test des Gas-Cerenkov-Detektors für den Crystal-Barrel-Aufbau an ELSA*

[24] Diploma thesis Alexander Winnebeck (2006), HISKP, *Entwicklung und Implementierung eines universellen, FPGA basierten Triggermoduls für das Crystal-Barrel-Experiment an ELSA*

[25] Doctoral thesis (in preparation), HISKP, *Weiterentwicklung und Implementierung der Datenakquisitionshard- und software für das Crystal-Barrel-Experiment an ELSA*

[26] Diploma thesis Manuela Gottschall (2007), HISKP, *Verbesserung der Triggereigenschaften des Crystal-Barrel-Detektors an ELSA mit einer Silizium-Photomultiplier-Auslese der Kristalle*

[27] Diploma thesis Marco Wehrfritz (2008), HISKP, *Entwicklung und Test eines Silizium-Photomultiplier-Triggers für das Crystal-Barrel-Kalorimeter*

[28] Diploma thesis Friedemann Zenke (2009), HISKP, *A new avalanche photodiode readout of the Crystal Barrel experiment*

[29] Physics Letters B 643 (2006), pp 41-45, *On the extraction of the quark mass ratio* $(m_d - m_u)/m_s$ *from* $\Gamma(\eta' \to \pi^0\pi^+\pi^-)/\Gamma(\eta' \to \eta\pi^+\pi^-)$, A. Borasoy, Ulf-G. Meißner, R. Nißler

[30] Diploma thesis Christian Honisch (in preparation), HISKP, *Untersuchungen zu einer neuen Avalanche-Photodioden-Auslese fr das Crystal-Barrel-Kalorimeter*

[31] private communication M. Grüner (2009)

[32] Nuclear Instruments and Methods in Physics Research A315 (1992), pp 48-54, *Spiral projection chambers: experience and prospects*, U. Gastaldi

[33] Diploma thesis Roman Schmitz (2008), HISKP, *Simulationen zum Nachweis geladener Teilchen für das Crystal-Barrel-Experiment an ELSA*

[34] Nuclear Instruments and Methods in Physics Research A594 (2008), pp 339-350, *The WASA detector facility at CELSIUS*, Chr. Bargholtz *et al.*

[35] Proceedings of ICHEP 2002, pp 62-64, *The Alice Experiment at CERN LHC*, P. Kuijer *et al.*

[36] Nuclear Instruments and Methods in Physics Research A602 (2009), pp 682-686, *Status and commissioning of the ATLAS experiment at LHC*, A. Di Ciacco *et al.*

[37] Nuclear Physics B (Proc. Suppl.) 170 (2007), pp 264-272, *Status and Commissioning of the CMS experiment*, O. Buchmüller *et al.*

[38] Nuclear Instruments and Methods in Physics Research A286 (1990), pp 76-98, *THE ASTERIX SPECTROMETER AT LEAR*, S. Ahmad *et al.*

[39] Nuclear Physics A558 (1993), pp 369-382, *Nuclear Physics with OBELIX*, A. Ableev *et al.*

[40] IEEE Transaction on Nuclear Science, VOL. 38, No.2, (April 1991), *The 4π cylindrical detector SPC/XDC for X-ray and charged particles detection in antiproton annihilations in the OBELIX experiment at LEAR*, G. Bendiscioli *et al.*

[41] Nuclear Instruments and Methods in Physics Research A598 (2009), pp 89-93, *TPC review*, A. Attié

[42] Nuclear Instruments and Methods in Physics Research A409 (1998, pp 9-13, *Development of a TPC detector for the ALICE experiment*, J. Baechler for the ALICE collaboration

[43] Nuclear Instruments and Methods **24** (1963), pp. 381-389, *Uncertainties in track momentum and direction, due to multiple scattering and measurement errors*, R. L. Glückstern

[44] Diploma thesis Sebastian Neubert (2005), Technische Universität München E18, *A GEM-based TPC for $\bar{P}ANDA$*

[45] Helmuth Spieler, *Semiconductor Detector Systems*, Oxford Science Publications, ISBN 978-0-19-852784-8

[46] *APV25-S1 User Guide v. 2.2*, L. Jones, RAL Microelectrinics Design-Group

[47] Nuclear Instruments and Methods in Physics Research A422 (1999), pp 257-262, *Recent developments and applications of fast position-sensitive gas detectors*, F. Sauli

[48] COMPASS Note 2002-8 , *The COMPASS Online Data Format Version 4*, H. Fischer *et al.*

[49] T2K TPC ASIC AFTER, *data sheet version 1.1.b*, P. Baron, Laboratoir de recherche sur les loir fondamentales l'Universe

[50] Private communication Maxence Vandenbrouck (2009), Technische Universität München (E18)

[51] Private communication Alexander Schmah (2009), Technische Universität München (E12)

[52] Private communication Roman Schmitz (2009), HISKP

[53] AutoCAD drawings done by Dieter Walther (2009), HISKP

[54] Nuclear Instruments and Methods 129 (1975), pp 497-499, *Some practical remarks on multiple scattering*, V. L. Highland

[55] Nuclear Instruments and Methods in Physics Research A 538 (2005), pp 372-383, *Resolution studies of cosmic-ray tracks in a TPC with GEM readout*, R. K. Carnegie *et at.*

[56] Nuclear Instruments and Methods in Physics Research A 480 (2002), pp 501-507, *A high resolution silicon beam telescope*, C. Amsler *et al.*

[57] arXiv:0809.5133v2 [nucl-ex] 6 Oct 2008, *The Time Projection Chamber for the ALICE Experiment*, C. Lippmann and the ALICE Collaboration

[58] Nuclear Instruments and Methods in Physics Research A 518 (2004), pp 132-134, *The HARP TPC Laser Calibration System*, G. Vidal-Sitjes

[59] Physical Review vol. 136 number 1B (1964), *Decay Scheme of* Rb^{83}, I. Dostrovsky *et al.*